

V^0 production ratios at LHCb and the alignment of its RICH detectors

Christopher George Blanks

High Energy Physics
Blackett Laboratory

A thesis submitted to Imperial College London
for the degree of Doctor of Philosophy

December 2011

Declaration

The work presented in this thesis was carried out between October 2007 and August 2011, and represents the results of my own studies with the support and assistance of members of the Imperial College HEP group and the broader LHCb collaboration. The following specific contributions were made by me:

Chapter 1 Fig. 1.1.

Chapter 3 Figs. 3.4 and 3.5.

Chapter 4 Figs. 4.8, 4.11 and 4.12.

Chapter 5 Fig. 5.1(a). The development of the geometric RICH alignment procedure described in Section 5.4, including Figs. 5.2 – 5.5. The application of that alignment procedure to calibrate the RICH with collision data described in Section 5.5, including Figs. 5.6 and 5.7. The further investigations into the limitations of that initial calibration described in Section 5.7, including Figs. 5.11 – 5.13. Implementation of the alignment monitoring system based on the procedure mentioned above as well as the design, development and maintenance of the LAMS control software, described in Section 5.9 and Appendix A, including Figs. A.1 and A.2. Development of the procedure to estimate the Cherenkov photon yield from the three RICH radiators described in Section 5.10, including Fig. 5.16.

Chapter 6 Fig. 6.1(b). The analysis procedure described in Section 6.6, including Figs. 6.3, 6.4 and 6.6 – 6.9: specifically, implementation and optimisation of the selection cuts (track and vertex quality, Fisher discriminant and V^0 background veto), application of the simulated impact parameter smearing procedure and development of both the signal extraction fit and the procedure to correct the p_T and y distributions of MC candidates. Determination of the measurement range and binning as well as the combined selection and detector efficiencies. Estimation of all systematic uncertainties. Estimates related to track and primary vertex reconstruction were based on studies by T. Blake and those related to material interactions relied on the work of F. Dettori and S. Miglioranzi. The combination of LHCb field up and down results was performed with a weight function derived to minimise the variance of the combined results, as suggested by O. Schneider. Calculation of final results and uncertainties, including Figs. 6.11 – 6.14.

Where other sources of information have been included, they have been explicitly referenced.

This thesis has not been submitted for any other qualification. The results of the RICH alignment presented in Chapter 5 have been previously reported by me at the RICH 2010 conference [1]. Preliminary results on the V^0 production analysis presented in Chapter 6 were presented by me at the ICHEP 2010 conference [2]. I was also the lead author on a paper reporting these results on behalf of the LHCb collaboration [3].

Christopher G. Blanks, 13 December 2011

Abstract

The strangeness production ratios $\bar{\Lambda}/\Lambda$ and $\bar{\Lambda}/K_S^0$ are measured by the LHCb detector from 0.3 nb^{-1} of proton-proton collisions delivered by the Large Hadron Collider (LHC) at CERN with centre-of-mass energy $\sqrt{s} = 0.9 \text{ TeV}$ and 1.8 nb^{-1} at $\sqrt{s} = 7 \text{ TeV}$. Both ratios are presented as a function of transverse momentum, p_T , and rapidity, y , in the ranges $0.15 < p_T < 2.50 \text{ GeV}/c$ and $2.0 < y < 4.5$. The ratios measured at the two energies are in good agreement in an overlapping region of rapidity loss, $\Delta y = y_{\text{beam}} - y$, and are consistent with previous measurements.

A review of the Standard Model is presented with emphasis on the difficulties in its application for predictions of physics at the LHC. Phenomenological models are introduced as the current state of the art for such predictions. Accurate models are required as an essential benchmark for future discoveries of physics beyond the Standard Model. LHCb's results represent a powerful test for these models in the soft QCD regime for processes including hadronisation. The ratio $\bar{\Lambda}/\Lambda$, measuring the transport of baryon number from the collision into the detector, is smaller in data than predicted, particularly at high rapidity. The ratio $\bar{\Lambda}/K_S^0$, measuring the baryon-to-meson suppression in strange quark hadronisation, is significantly larger than expected.

The LHCb experiment is introduced, with particular focus on its Ring Imaging Cherenkov (RICH) detectors. The development and successful implementation of a method to align those RICH detectors is presented, using proton-proton collision data from the early running period of the Large Hadron Collider, which began in November 2009. The performance of the RICH detectors is investigated with preliminary analysis of the Cherenkov photon yield. The RICH mirror positions are monitored using an automated software control system, which has been running successfully since October 2008.

Acknowledgments

I want to express my gratitude to the Science and Technology Facilities Council, Imperial College London and to the European Organization for Nuclear Research for funding and hosting me during this PhD programme. Special thanks to the UK Liaison Office at CERN for providing such excellent accommodation in Geneva.

None of the work presented in this thesis would have been possible without the many hundreds of physicists and engineers who have developed and who maintain the Large Hadron Collider and the LHCb detector or without the more than 80 countries around the world who choose to fund research at CERN.

I have enjoyed the wonderfully collaborative environment of the RICH group, and owe particular thanks to Antonis Papanestis and David Websdale, who helped me out so much with the alignment studies presented in Chapter 5.

The V^0 production analysis presented in Chapter 6 was carried out in collaboration with Thomas Blake, Walter Bonivento, Francesco Dettori and Raluca Mureşan, with numerous useful discussions within the LHCb Minimum Bias and Flavour Physics working groups, chaired respectively by Michael Schmelling and Olivier Schneider.

Thank you to everyone in the Imperial HEP group, particularly to my supervisor Ulrik Egede and to Andrei Golutvin for suggesting I take a look at Λ decays.

Special thanks go to Tom for making second breakfast a habit and to Fatima, my PhD sister.

Colin, Linda, Jennifer & Nobuko

Contents

List of Figures	15
List of Tables	17
1 Introduction	19
1.1 High Energy Physics	19
1.2 An outline of this thesis	21
2 The Standard Model	23
2.1 Introduction	23
2.2 QED: The first gauge field theory	24
2.3 Electroweak interactions	26
2.4 Strong interactions	29
2.5 Higgs-Yukawa interactions	32
2.6 Free parameters	34
2.7 Unanswered questions in the Standard Model	34
3 Phenomenological QCD	37
3.1 Practical application of Standard Model theory	37
3.2 Generators	41
3.2.1 Introduction	41
3.2.2 Primary interactions at a proton-proton collider	42
3.2.3 Hadronisation and strange quark production	44
4 The LHCb experiment	47
4.1 CERN and the Large Hadron Collider	47
4.1.1 A short history of CERN	47
4.1.2 The Large Hadron Collider	48
4.2 The LHCb detector	49
4.2.1 Introduction	49
4.2.2 Detector layout	51
4.2.3 Vertex Locator	52

4.2.4	Tracking	53
4.2.5	RICH particle identification	54
4.2.6	Calorimetry	57
4.2.7	Muon detection	58
4.2.8	Trigger and data processing	59
4.2.9	MC simulation	60
4.2.10	Performance and outlook	61
5	RICH detectors	63
5.1	An introduction to Cherenkov radiation	63
5.2	LHCb's RICH system	65
5.3	Geometric alignment	66
5.4	Development of an alignment procedure	67
5.4.1	Observables	67
5.4.2	Simulations	68
5.4.3	Measurements	70
5.4.4	Test exercise	71
5.5	Application to collision data	72
5.5.1	Method	74
5.5.2	Results and discussion	75
5.6	PID performance after alignment	75
5.7	Further investigations and outlook	76
5.8	Latest performance	79
5.9	Alignment monitoring	80
5.10	Cherenkov photon yield	81
6	V^0 production ratios	83
6.1	An introduction to “ V ” decays	83
6.2	Strangeness production ratios	86
6.3	An overview of LHCb's tracking system	88
6.4	Data samples	88
6.5	Monte Carlo generation	89
6.6	Analysis procedure	89
6.6.1	Reconstruction and quality cuts	89
6.6.2	Selection	90
6.6.3	Signal extraction	93
6.6.4	Kinematic corrections for simulated candidates	94
6.6.5	Measurement range and binning	95
6.6.6	Efficiency correction	95
6.7	Systematic uncertainties	96

6.7.1	Experimental uncertainties	97
6.7.2	Model-dependent uncertainties	98
6.7.3	Procedural uncertainties	100
6.7.4	Cross-checks	100
6.7.5	Summary	101
6.8	Results	101
6.8.1	Combination of data sets	101
6.8.2	Observations	103
6.9	Recent development of the Perugia tunes	105
6.10	Conclusions	107
7	Summary	109
A	The LAMS control project	113
B	V^0 production ratio tables	117
B.1	Tabulated results	117
B.2	Tabulated results before non-prompt correction	119
C	List of Acronyms	121
	Bibliography	125

List of Figures

1.1	The Standard Model of High Energy Physics	20
3.1	Measured dependence of the QCD coupling α_s with interaction energy . .	40
3.2	Proton PDFs from combined experimental results at HERA	40
3.3	Evidence for three generations of light SM neutrino from Z^0 decays at LEP	42
3.4	Illustration of a high energy proton-proton collision	43
3.5	Illustration of hadronisation in the Lund model	45
4.1	The CERN accelerator complex	49
4.2	Parton interaction probabilities with luminosity	50
4.3	Predicted $b\bar{b}$ production angles at LHCb	50
4.4	LHCb detector layout	51
4.5	The silicon VELO stations with r, ϕ geometry	52
4.6	Layout of the tracking system with evolving magnetic field strength	53
4.7	Polar angle vs. momentum for MC generated pions from $B^0 \rightarrow \pi^+\pi^-$. . .	55
4.8	Cherenkov angle for π, K & p as a function of momentum	55
4.9	A cosmic event reconstructed in RICH1	56
4.10	Schematic of an HPD	57
4.11	Integrated CPU processing time used by LHCb physicists on the grid . . .	60
4.12	Delivered integrated luminosity from pp collisions at $\sqrt{s} = 7$ TeV	60
5.1	Cherenkov light cone and analogous Mach wave	64
5.2	RICH misalignment on the photon detector plane	68
5.3	Degradation in precision due to simulated RICH misalignments	69
5.4	Example fit for misalignment parameters	70
5.5	Illustrated misalignments of a RICH2 HPD panel and correlations with $\Delta\theta(\phi)$ amplitudes A and B	72
5.6	RICH1 data from first pp collisions	73
5.7	Illustrated misalignments of a RICH1 spherical mirror and the entire RICH2 apparatus	74
5.8	Improving π PID with alignment	75
5.9	Selection of $\phi(1020) \rightarrow K^+K^-$ with RICH PID	76

5.10	Time-integrated HPD pixel hits in RICH 1	77
5.11	Cumulative share of photons seen by HPDs in RICH 1	77
5.12	Individual HPD ϕ coverage and a comparison of their $\Delta\theta$ peaks in an overlapping region	78
5.13	The ϕ coverage of one HPD seeing light from two RICH 1 mirror pairs and comparison of their $\Delta\theta$ peaks in an overlapping region	78
5.14	Selection of $B^0 \rightarrow K^+\pi^-$ using PID to measure direct CP violation	79
5.15	Schematic of the Laser Alignment Monitoring System	80
5.16	Estimation of the Cherenkov photon yield: $\Delta\theta$ weight function and track-yield distribution	82
6.1	V^0 decays photographed at the Bevatron	84
6.2	Predictions for $\bar{\Lambda}/\Lambda$ at the LHC by selected PYTHIA 6 tunes	87
6.3	Track and vertex fit quality examples	90
6.4	The Fisher discriminant \mathcal{F}_{IP} for K_S^0 and $\bar{\Lambda}$	91
6.5	VELO impact parameter resolution	92
6.6	Λ impact parameter smeared in simulation to match data	92
6.7	V^0 background revealed in Armenteros-Podolanski variables	93
6.8	Invariant mass peaks from reconstructed $\bar{\Lambda} \rightarrow p\pi^-$ and $K_S^0 \rightarrow \pi^+\pi^-$	94
6.9	MC V^0 candidates weighted to match kinematic distributions in data	95
6.10	Production ratios in data/MC compared as a function of material traversed	99
6.11	$\bar{\Lambda}/\Lambda$ and $\bar{\Lambda}/K_S^0$ as a function of y in intervals of p_T	104
6.12	$\bar{\Lambda}/\Lambda$ and $\bar{\Lambda}/K_S^0$ as a function of y and p_T at $\sqrt{s} = 0.9 \text{ TeV}$	105
6.13	$\bar{\Lambda}/\Lambda$ and $\bar{\Lambda}/K_S^0$ as a function of y and p_T at $\sqrt{s} = 7 \text{ TeV}$	106
6.14	$\bar{\Lambda}/\Lambda$ and $\bar{\Lambda}/K_S^0$ as a function of Δy	106
A.1	An illustrative flow diagram of the LAMS control project	114
A.2	The LAMS control project GUI	115

List of Tables

1.1	The relative strengths and ranges of the four fundamental forces	21
5.1	Sources of uncertainty on θ_C	66
5.2	Alignment corrections found from early collision data	74
5.3	Comparison of μ and σ for $\Delta\theta$ distributions of individual HPDs	77
5.4	Cherenkov photon yields found in data and simulation	82
6.1	Optimised coefficients for \mathcal{F}_{IP}	91
6.2	Signal V^0 yields from data sets taken at $\sqrt{s} = 0.9$ and 7 TeV	94
6.3	Longest lived ancestors of MC generated Λ and $\bar{\Lambda}$	96
6.4	Comparisons of field up and down results by χ^2 probability	101
6.5	Summary of systematic uncertainties	102
B.1	$\bar{\Lambda}/\Lambda$ and $\bar{\Lambda}/K_S^0$ as a function of y and p_T at $\sqrt{s} = 0.9$ TeV	117
B.2	$\bar{\Lambda}/\Lambda$ and $\bar{\Lambda}/K_S^0$ as a function of y and p_T at $\sqrt{s} = 7$ TeV	118
B.3	$\bar{\Lambda}/\Lambda$ and $\bar{\Lambda}/K_S^0$ before non-prompt correction at $\sqrt{s} = 0.9$ TeV	119
B.4	$\bar{\Lambda}/\Lambda$ and $\bar{\Lambda}/K_S^0$ before non-prompt correction at $\sqrt{s} = 7$ TeV	120

Chapter 1

Introduction

It may be that the great influence of the Greeks on modern science and their short list of elements – earth, air, fire and water – has inspired a nostalgia for such a concise description of the universe. It may be that the impulse for a simple, unifying description is part of human nature, as similar ancient ideas are well known from Egypt to Japan. For me though, it is the repeated observations in the field of High Energy Physics of one guiding principle that inspires belief in fundamental particles and fundamental forces:

“... every particle decays into lighter particles, unless prevented from doing so by some conservation law.”

– *D. Griffiths, Introduction to Elementary Particles, 1987* [4]

1.1 High Energy Physics

The “High” in High Energy Physics has had an ever-changing definition reflecting the contemporary boundary of our understanding of the natural world at a fundamental level. For current High Energy Physicists, this boundary is the 7 TeV centre-of-mass energy of proton collisions at the LHC. Each new expansion of the energy frontier is a step into the unknown, where our understanding of the constituents of matter and the nature of the interactions between them will be tested and may be overturned.

The high energy frontier has come a long way – 12 orders of (fixed target equivalent) magnitude [5] – since John Cockcroft and Ernest Walton began their pioneering work in 1928 to surpass the energy limits of naturally occurring α radiation by creating a beam of accelerated protons [6,7]. At that time, only two of the particles now considered to be fundamental had been identified: the lightest of the charged leptons (the electron, discovered by J. J. Thomson in 1897 [8]) and the mediator of the electromagnetic force (the photon: a corpuscular description of light invoked by Albert Einstein to explain the photoelectric effect [9]). Just four years later, in 1932, a third particle: the positron (or antielectron) was

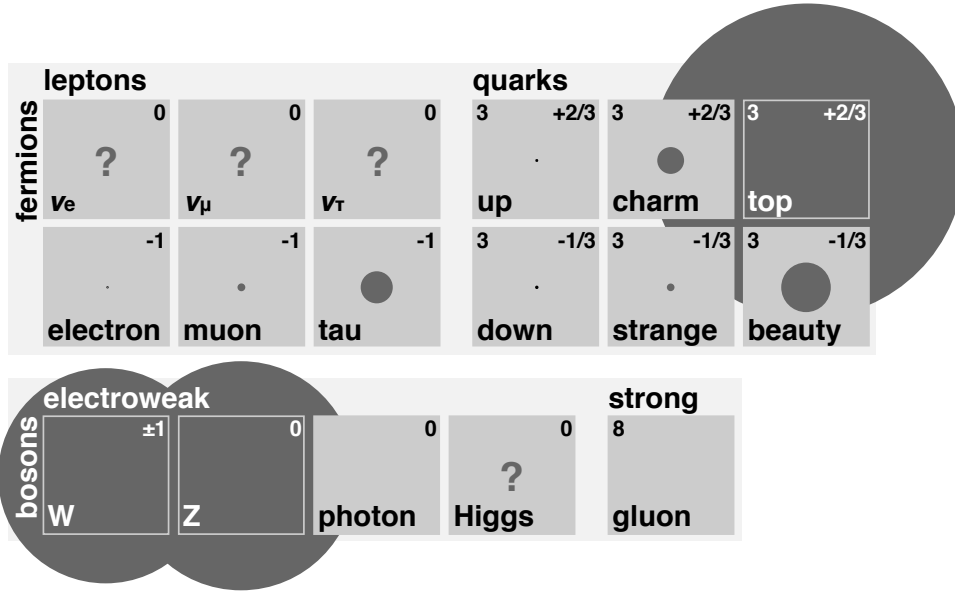


Figure 1.1: The Standard Model of High Energy Physics. The fundamental particles are shown with their electric charge (top right) and number of color states (top left), where applicable. The circular areas given for each particle are proportional to their respective masses, from the light $0.5 \text{ MeV}/c^2$ electron to the heavy $172 \text{ GeV}/c^2$ top quark. The photon and gluons are massless. The masses of the neutrinos and the Higgs boson are currently unknown. The Higgs has not yet been observed.

to be discovered by Carl Anderson [10], confirming the existence of antimatter implicit in Dirac’s equation [11]. A “zoo” of new particles (and antiparticles) followed over the subsequent decades with discoveries driven by developments in accelerator and detector technologies. The creation of new theoretical ideas to catalogue and sometimes anticipate (e.g. the Ω^- baryon and Z^0 boson discussed in Chapter 2) these particles, as well as to describe their interactions, has produced our current picture of the fundamental constituents of nature called the Standard Model, summarised in Fig. 1.1.

In this picture, each type of particle is identified by its mass, mean lifetime, spin and its coupling to the fundamental forces: electromagnetism and the weak and strong nuclear interactions. Each type of particle is an example of a Platonic ideal; with every specimen a perfect reproduction, indistinguishable from the next. An overview of Standard Model theory is given in Chapter 2.

The matter particles, generically called fermions, are divided into two families: the six flavours of lepton, of which three couple to the electromagnetic force and all couple to the weak force, and the six flavours of quark, which all couple to the electromagnetic, weak and strong forces. Each family is split into three generations of increasing mass but otherwise identical properties. Each of these generations consists of two particles differing only by mass, mean lifetime and electric charge. All of the quarks may come in three colours: red, green and blue, representing the charges of the strong force. For each matter particle there is an antiparticle with the same mass, mean lifetime and spin but opposite

Table 1.1: The relative strengths of the four fundamental forces. The range of each force is related to the mass of the mediating particle. [12]

Fundamental interaction	Strength	Range [m]	
Strong	1	10^{-15}	$\sim 1/m_{\text{pion}}$
Electromagnetic	10^{-2}	∞	$\sim 1/m_{\text{photon}}$
Weak	10^{-6}	10^{-18}	$\sim 1/m_{W^\pm, Z^0}$
Gravitation	10^{-42}	∞	$\sim 1/m_{\text{graviton}}$

couplings to the forces. All in all there are 12 leptons and 36 quarks.

The fundamental forces are mediated by particles called bosons: the eight gluons, g , of the strong interaction, the three carriers of the weak interaction: W^\pm & Z^0 and the photon, γ , which mediates the electromagnetic force. The range of each force is inversely proportional to the mass of the mediating particle.¹ The Higgs boson has been predicted by the unification of the electromagnetic and weak interactions but has not yet been observed. At the scale of these fundamental objects gravitation exerts a negligible influence and its hypothetical mediator, the graviton, is not included in the model. The relative strength and range of each force is summarised in Table 1.1.

While the advancements of 20th century physics, culminating in the Standard Model, can be considered a great success, it is clear that we do not yet have a complete, fundamental description of nature. There is no quantum field theory for gravitation and the matter-antimatter asymmetry observed in the universe cannot be accounted for. The search for such fundamental answers will always motivate enquiring minds to drive innovations in technology and theory that will continue to redefine the ‘‘High’’ in High Energy Physics in the new century.

1.2 An outline of this thesis

This thesis is presented in four main sections:

I – Chapters 2 and 3 introduce Standard Model theory, with particular emphasis on the strong force, and argue the need for phenomenological models to make useful predictions at the LHC. An explanation of common approaches to these models and the requirement for validation by new experimental results is also given.

II – Chapter 4 provides a walkthrough of the LHCb detector, its components and early performance. The physics goals of the experiment are given in the historical context of CERN.

¹Where strong interactions are approximated by pion exchange. [12]

III – Chapter 5 is focussed on Ring Imaging Cherenkov (RICH) detectors, from an introduction to Cherenkov radiation to the calibration of LHCb’s detectors with early collision data and their successful employment for particle identification.

IV – Chapter 6 presents an analysis of the strangeness production ratios $\bar{\Lambda}/\Lambda$ and $\bar{\Lambda}/K_S^0$ as a powerful probe for hadronisation processes in the new high energy conditions at the LHC. LHCb can make an important contribution thanks to its full instrumentation at small angles to the colliding proton beams, which is unique among the LHC experiments.

Finally, Chapter 7 presents a summary of this thesis and its conclusions.

Chapter 2

The Standard Model

“I was at first almost frightened when I saw so much mathematical force made to bear upon the subject, and then wondered to see that the subject stood it so well.”

– *Michael Faraday, letter to James Clerk Maxwell, 25 March 1857* [13]

2.1 Introduction

The Standard Model (SM) is a relativistic quantum field theory that describes the dynamics of the fundamental particles under the influence of the electromagnetic, weak and strong interactions. These forces are brought together in the language of gauge theories. The SM is gauge invariant, i.e. all measurable predictions are unchanged by a set of transformations, or symmetries. Invariance of the Standard Model to the Poincaré global symmetry group: translations, rotations and boosts in spacetime, leads naturally to the classical physics conservation laws for energy, momentum and angular momentum, by Noether’s theorem [14].

The Standard Model Lagrangian can be summarised as:

$$\mathcal{L}_{\text{SM}} = \mathcal{L}_{\text{EW}} + \mathcal{L}_{\text{Strong}} + \mathcal{L}_{\text{Higgs-Yukawa}} \quad (2.1)$$

where the Higgs-Yukawa term must be combined with the electroweak (EW) and strong interactions to produce non-zero particle masses without breaking the overall symmetry of the theory.

The conserved charges of the electromagnetic, weak and strong forces result from invariance of the Standard Model to the local symmetry group: $\text{SU}(3)_{\text{C}} \otimes \text{SU}(2)_{\text{W}} \otimes \text{U}(1)_{\text{Y}}$, where C represents the color charge of the strong force, W the isospin and Y the hypercharge of the unified electroweak interaction. The electric charge, Q , is also conserved and is derived from the hypercharge and the weak isospin, $Q = W^3 + Y$. The symmetry

group has 12 generators that give rise to all the force mediators: the eight gluons, g , of the strong force, the three weak vector bosons, W^+ , W^- & Z^0 , and the single photon, γ , of the electromagnetic interaction.

An additional four conserved quantities result from “accidental” global symmetries found in the Standard Model: baryon number, B , and the three lepton family numbers: L_e , L_μ & L_τ . With the discovery of neutrino oscillations by Super Kamiokande in 1998 [15] and the implication for non-zero neutrino masses, the conservation of individual lepton family numbers can no longer be held and is replaced by conservation of total lepton number, $L = L_e + L_\mu + L_\tau$.

2.2 QED: The first gauge field theory

The gauge field theory Quantum Electrodynamics (QED), which reached maturity in the 1940s [16], was the first successful combination of quantum mechanics and special relativity and describes the interactions of charged particles by exchange of a neutral, massless boson (spin-1): the photon.

All matter particles are fermions (spin- $\frac{1}{2}$) and are described by the Dirac equation. The Lagrangian density for a free fermion field, f , of mass, m , is (with $\hbar = c = 1$):

$$\mathcal{L}_{\text{Fermion}} = \bar{f}(i\gamma^\mu\partial_\mu - m)f \quad (2.2)$$

where the Greek indices denote spacetime directions (following Einstein notation), γ^μ are the Dirac matrices¹, ∂_μ are the spacetime derivatives, $\partial/\partial x_\mu$, and \bar{f} is the conjugate field, $\bar{f} = f^\dagger\gamma^0$ and f^\dagger is the complex conjugate transpose of f .

In quantum mechanics, the expectation value of an observable, Ω , of a state, $|\psi\rangle$, is given by: $\langle\Omega\rangle = \langle\psi|\hat{\Omega}|\psi\rangle$, where $\hat{\Omega}$ is the related Hermitian operator. This value is unchanged by a local (position dependent) gauge transformation from the Abelian (i.e. commutative) group U(1): $\psi \rightarrow \psi' = e^{i\omega(x)}\psi$, i.e. the physics of the system is blind to the phase $\omega(x)$ and is said to be gauge invariant.

The complete physical system can be derived from the Lagrangian density that must therefore also be gauge invariant. However, the action of this U(1) group transformation on the free fermion field introduces an unwanted extra derivative term (underlined):

$$\mathcal{L}_{\text{Fermion}} \rightarrow \mathcal{L}'_{\text{Fermion}} \equiv \bar{f}(i\gamma^\mu[\partial_\mu + \underline{i\partial_\mu\omega(x)}] - m)f . \quad (2.3)$$

Local gauge invariance can be restored by replacing the derivative in Eqn. 2.2 with a covariant derivative, D_μ , that introduces an interaction term with a vector boson (spin-1)

¹The 4×4 matrices γ^μ are defined by the anticommutator relation: $\{\gamma^\mu, \gamma^\nu\} = 2g^{\mu\nu}$, where $g^{\mu\nu}$ is the Minkowski metric.

gauge field, A_μ :

$$\partial_\mu \rightarrow D_\mu \equiv \partial_\mu + igA_\mu \quad (2.4)$$

where g is the coupling strength between the gauge and fermion fields. The interaction term with A_μ transforms to introduce an additional term in $\omega(x)$ (Eqn. 2.5) that exactly cancels with the unwanted term introduced in the derivative in Eqn. 2.3:

$$igA_\mu \rightarrow igA'_\mu \equiv igA_\mu - i\partial_\mu\omega(x) . \quad (2.5)$$

The QED Lagrangian density is completed with a gauge invariant kinetic energy term for the boson field:

$$\begin{aligned} \mathcal{L}_{\text{QED}} &= \mathcal{L}_{\text{Boson}} + \mathcal{L}_{\text{Fermion}} \\ &= -\frac{1}{4}F_{\mu\nu}F^{\mu\nu} + \bar{f}(i\gamma^\mu D_\mu - m)f \end{aligned} \quad (2.6)$$

where the electromagnetic field tensor, $F_{\mu\nu}$, can be written:

$$F_{\mu\nu} = \partial_\mu A_\nu - \partial_\nu A_\mu . \quad (2.7)$$

The gauge field required for the partial derivative to preserve U(1) symmetry contains no term proportional to $A^\mu A_\mu$, therefore the boson is massless. The field, A_μ , is interpreted as the photon field and the coupling strength, g , as the electric charge of the fermion, Qe ; where Q is ∓ 1 for an electron/positron and $+\frac{2}{3}$ for an up quark, etc.

By enforcing the concept of U(1) gauge invariance, expected for quantum mechanical observables on the free Dirac field Lagrangian, fermions are required to interact with a massless vector boson field. Spectacularly, this single concept results in a complete and precise description of electromagnetic interactions, from Compton scattering to Maxwell's equations.

The electromagnetic coupling strength, α ($\propto e^2$), is not predicted by QED and must be determined by experiment. Precise tests of QED therefore require a suitably precise measurement of α as the basis for calculating the predictions of the theory. For this reason, tests of QED are often reported as the agreement between the electromagnetic coupling strength α determined from experiments involving different physical systems. A recent comparison, between measurements of the anomalous magnetic dipole moment of the electron and the recoil of Rubidium atoms with photon absorption, gives an agreement on the value of α to about 100 parts per billion [17].

2.3 Electroweak interactions

Weak interactions had first been described by Fermi in 1934 [18] as the mechanism for radioactive β -decay. The Fermi model of a four-point “contact” interaction, with coupling constant G_F , was later thought to be only a low energy approximation for a short-range interaction, mediated by a massive “intermediate vector boson” that carried an electric charge equal to that of the β electron or positron [19, 20].

A gauge invariant quantum field theory of weak interactions was developed over the 1960s, which described the “charged current” interactions of the massive bosons, the W^\pm . The theory also included “neutral current” interactions, by exchange of the Z^0 vector boson, which were later discovered at CERN by the Gargamelle experiment [21].

In completing this theory in 1968 [22–24], Glashow, Salam and Weinberg showed that the weak and electromagnetic interactions are really two aspects of a fundamental “electroweak” symmetry. This unification of forces extended Maxwell’s joint formulation of electricity and magnetism a century earlier and provides a continuing source of inspiration for a Grand Unified Theory that may one day unite all the forces in nature.

The weak interaction is special in the Standard Model, being the only force to interact with all known fermions. Weak interactions have also uniquely been shown to violate parity (or “mirror symmetry”), P , and charge conjugation, C , as well as the combined CP symmetry; the violation of which is thought to be required to explain the imbalance of matter over antimatter in the universe [25–28].

The electroweak Lagrangian is constructed, similarly to the example of QED in Section 2.2, by the introduction of interaction terms between free fermions and boson fields to enforce gauge invariance. Unlike the case of QED, the bosons of the weak interaction W^+ , W^- and Z^0 were thought to be massive to account for the weakness of the force. To introduce these masses and maintain gauge invariance requires an additional “Higgs” term. The complete electroweak Lagrangian density can be summarised as:

$$\mathcal{L}_{\text{EW}} = \mathcal{L}_{\text{Boson}} + \mathcal{L}_{\text{Fermion}} + \mathcal{L}_{\text{Higgs}} . \quad (2.8)$$

The electroweak gauge symmetry $\text{SU}(2)_W \otimes \text{U}(1)_Y$ gives rise to four vector gauge bosons: the weak isospin mediators $W_\mu^{a=1,2,3}$ and the hypercharge mediator B_μ . The covariant derivative required to maintain this symmetry is a 2×2 matrix of the form:

$$\mathbf{D}_\mu = \partial_\mu \mathbf{I} + ig_W \mathbf{T}^a W_\mu^a + ig_Y Y B_\mu \mathbf{I} \quad (2.9)$$

where \mathbf{T}^a are the generators of $\text{SU}(2)$ and the weak isospin term is written in full as:

$$ig_W \mathbf{T}^a W_\mu^a \equiv \frac{ig_W}{2} \begin{pmatrix} W_\mu^3 & W_\mu^1 - iW_\mu^2 \\ W_\mu^1 + iW_\mu^2 & -W_\mu^3 \end{pmatrix} . \quad (2.10)$$

Since the weak interaction is known experimentally to violate parity, the electroweak theory is constructed to give different interactions to left-handed and right-handed fermion fields. A fermion field, f , can be expressed as the sum of left- and right-handed chiral components: $f = f_L + f_R$, where both fields are projections of the fermion defined by the chiral operators:

$$f_L = \frac{1}{2}(1 - \gamma^5)f \quad \text{and} \quad f_R = \frac{1}{2}(1 + \gamma^5)f \quad (2.11)$$

where $\gamma^5 (= i\gamma^0\gamma^1\gamma^2\gamma^3)$ is the fifth Dirac matrix.

The weakly interacting fermion fields form left-handed doublets and right-handed singlets under SU(2). For the first generation quarks and leptons, these are:

$$q_L = \begin{pmatrix} u_L \\ d_L \end{pmatrix}, \quad u_R, \quad d_R \quad \text{and} \quad l_L = \begin{pmatrix} \nu_{eL} \\ e_L \end{pmatrix}, \quad \nu_{eR}, \quad e_R. \quad (2.12)$$

These right-handed singlets are invariant under SU(2)_W and therefore do not couple to the W^a bosons, i.e. only left-handed fermions participate in the weak interaction. Both chiral fields however must couple to the U(1)_Y gauge boson B to preserve invariance. To achieve this handedness-dependent gauge symmetry requires two covariant derivatives derived from Eqn. 2.9:

$$\mathbf{D}_{L\mu} = \partial_\mu \mathbf{I} + ig_W \mathbf{T}^a W_\mu^a + ig_Y Y_L B_\mu \mathbf{I} \quad (2.13)$$

$$D_{R\mu} = \partial_\mu + ig_Y Y_R B_\mu \quad (2.14)$$

where the hypercharge value, Y , is allowed to differ between the left- and right-handed fermion fields.

A gauge invariant fermion Lagrangian can be written in terms of the chiral fields as:

$$\mathcal{L}_{\text{Fermion}} = \bar{f}_L (i\gamma^\mu \mathbf{D}_{L\mu}) f_L + \bar{f}_R (i\gamma^\mu D_{R\mu}) f_R - \bar{f}_L m f_R - \bar{f}_R m f_L \quad (2.15)$$

where the mass terms mix the left- and right-handed fields.

The boson field kinetic terms are introduced, similarly to the QED example in Section 2.2, as:

$$\mathcal{L}_{\text{Boson}} = -\frac{1}{4}(W_{\mu\nu}^a W^{a\mu\nu} + B_{\mu\nu} B^{\mu\nu}) \quad (2.16)$$

where the boson field tensors can be written:

$$W_{\mu\nu}^a = \partial_\mu W_\nu^a - \partial_\nu W_\mu^a + g_W \varepsilon^{abc} W_\mu^b W_\nu^c \quad (2.17)$$

$$B_{\mu\nu} = \partial_\mu B_\nu - \partial_\nu B_\mu \quad (2.18)$$

and ε^{abc} are the structure constants of SU(2) that define the commutation relations:

$$[\mathbf{T}^a, \mathbf{T}^b] = i\varepsilon^{abc}\mathbf{T}^c . \quad (2.19)$$

The SU(2) symmetry group is non-Abelian (i.e. Eqn. 2.19 $\neq 0$), which gives rise to interaction terms between the W_μ^a bosons. As with the QED derivation, the boson fields required to preserve gauge symmetry contain no mass terms. While this was suitable for the photon, this is problematic for the weak vector bosons, which have large masses.

The electroweak bosons are given mass by the ‘‘Higgs mechanism’’, described in Refs. [4, 29, 30]. In summary, a complex Higgs field, Φ , is introduced with a scalar kinetic term, \mathcal{T} , and a potential term, \mathcal{U} :

$$\mathcal{L}_{\text{Higgs}} = \mathcal{T} - \mathcal{U} = (\partial_\mu \Phi)^* \partial^\mu \Phi - (-\mu^2 \Phi^* \Phi + \lambda |\Phi^* \Phi|^2) . \quad (2.20)$$

With the conditions $\mu^2 > 0$ and $\lambda > 0$ the minimum of this potential is non-zero, leading to a gauge invariant vacuum expectation value, v , equal to:

$$v = \frac{\mu}{\sqrt{\lambda}} . \quad (2.21)$$

Each of the fields considered so far in this chapter have been treated as fluctuations about a vacuum potential equal to zero. To put the Higgs field on a similar basis, the complex field, Φ , is reformulated in terms of a doublet of its real and imaginary parts, offset by the (real) vacuum expectation value, v . This doublet is most simply written in the ‘‘unitary’’ gauge as:

$$\Phi = \frac{1}{\sqrt{2}} \begin{pmatrix} 0 \\ H + v \end{pmatrix} \quad (2.22)$$

where H is the real Higgs field and the imaginary component is set to zero.

Electroweak interactions are introduced for the Higgs field to enforce invariance under the electroweak $\text{SU}(2)_W \otimes \text{U}(1)_Y$ symmetry. The required covariant derivative, given in Eqn. 2.9, can be written in the unitary gauge (with Higgs hypercharge $Y = \frac{1}{2}$) as:

$$D_\mu \Phi = \frac{1}{\sqrt{2}} \left[i\partial_\mu \mathbf{I} + \frac{1}{2} i g_W \begin{pmatrix} W_\mu^3 + \frac{g_Y}{g_W} B_\mu & W_\mu^1 + iW_\mu^2 \\ W_\mu^1 - iW_\mu^2 & -W_\mu^3 + \frac{g_Y}{g_W} B_\mu \end{pmatrix} \right] \begin{pmatrix} 0 \\ H + v \end{pmatrix} . \quad (2.23)$$

The gauge invariant Higgs kinetic term, $(D_\mu \Phi)^* D^\mu \Phi$, produces a non-zero Higgs mass and interacts with the electroweak gauge bosons to give them masses proportional to the vacuum expectation value. These masses are not assigned to the weak isospin W_μ^a and hypercharge B_μ bosons directly but to mixtures of them, which may be written concisely

as:

$$\begin{pmatrix} W_\mu^+ \\ W_\mu^- \end{pmatrix} = \frac{1}{\sqrt{2}} \begin{pmatrix} 1 & i \\ 1 & -i \end{pmatrix} \begin{pmatrix} W_\mu^1 \\ W_\mu^2 \end{pmatrix} \quad \text{and} \quad \begin{pmatrix} Z_\mu \\ A_\mu \end{pmatrix} = \begin{pmatrix} \cos \theta_W & \sin \theta_W \\ -\sin \theta_W & \cos \theta_W \end{pmatrix} \begin{pmatrix} W_\mu^3 \\ B_\mu \end{pmatrix} \quad (2.24)$$

where θ_W is the Weinberg angle and $\tan \theta_W = g_Y/g_W$.

These mixed boson states are interpreted as the physical weak boson fields, W_μ^+ , W_μ^- , Z_μ^0 and A_μ , the photon field described by QED. The spontaneous generation of these physical bosons from interactions between the Higgs potential and the $SU(2)_W \otimes U(1)_Y$ gauge bosons is commonly referred to as “electroweak symmetry breaking”.

The associated mass terms are:

$$\mathcal{L}_{\text{Mass}} = \mu^2 H^2 + \frac{g_W^2 v^2}{4} W^{+\mu} W_\mu^- + \frac{g_W^2 v^2}{8 \cos^2 \theta_W} Z^\mu Z_\mu + 0 A^\mu A_\mu . \quad (2.25)$$

where the Lagrangian mass term for a real field ϕ is of the form $\frac{1}{2}m^2\phi^2$ and for a complex field is $m^2\phi^\dagger\phi$. [30] The masses of the resulting Higgs, weak bosons and the photon are therefore taken from Eqn. 2.25 to be:

$$m_H = \sqrt{2}\mu , \quad m_W = \frac{g_W \mu}{2\sqrt{\lambda}} , \quad m_Z = \frac{m_W}{\sqrt{2} \cos \theta_W} \quad \text{and} \quad m_A = 0 . \quad (2.26)$$

The W^\pm and Z^0 bosons were first directly observed by the UA1 experiment at CERN in SPS $p\bar{p}$ collisions. Their measured masses: $m_W = 81 \pm 5 \text{ GeV}/c^2$ and $m_Z = 95 \pm 3 \text{ GeV}/c^2$, were in excellent agreement with the predictions from electroweak theory: $m_W = 82 \pm 2 \text{ GeV}/c^2$ and $m_Z = 92 \pm 2 \text{ GeV}/c^2$ [31, 32]. The Higgs boson, and the final validation of electroweak theory it would bring, remains to be found.

N.B. The electron charge, e , can be written in terms of the electroweak parameters as: $e = g_W \sin \theta_W$. From the measured masses, m_W and m_Z , and the relationship between them and the Weinberg angle, θ_W , from Eqn. 2.26, we can write down the comparative strengths of the electromagnetic and weak coupling as: $g_W/e = 1.91_{-0.27}^{+0.52}$. The weak coupling is actually stronger! It is really the reduced range, due to the large masses of its bosons, that gives the weak force its name. In the language of electroweak theory, the experimentally determined Fermi coupling constant can be written as: $G_F = \frac{\sqrt{2}}{8}(g_W/m_W)^2$.

2.4 Strong interactions

The Rutherford model of the atom as a small, massive nucleus with positive electric charge surrounded by a cloud of negative electrons was developed in 1911 after the observation by his students Geiger and Marsden of large angle deflections of α radiation from gold foil [33, 34]. The first theory of a force that could overcome the electric repulsion between

the protons to bind the nucleus, and explain Rutherford's observations, was the short range "strong nuclear force" proposed by Yukawa in 1934. Yukawa predicted a new massive boson to mediate this force: the meson (or "middle-weight" particle – heavier than the electron but lighter than the proton), which he suggested "may also have some bearing on the shower produced by cosmic rays." [35] Two cosmic ray mesons were subsequently discovered: the muon at low altitude in 1937, then the pion at high altitude in 1947 [36,37]. The pion was Yukawa's meson but the muon was a new heavy version of the electron – "Who ordered that?", remarked Rabi [38].

Later in 1947, the picture was further complicated by observation of the V^0 particle (now called K_S^0), dubbed "strange" due to its surprisingly long lifetime [39]. By the end of the 1950s, dozens of new particles had been discovered. Some structure was required and, in 1961, Gell-Mann devised the "Eightfold Way": a system to relate particles according to their electric charge, Q , and other apparently conserved quantities, dubbed "baryon number", B , and "strangeness", S [40]. This exercise in organisation bore fruit (just as Mendeleev's Periodic Table of Elements had done) in the recognition of missing pieces to the puzzle. Gell-Mann successfully predicted the Ω^- baryon (with $Q = -1$, $B = 1$ and $S = -3$), which was discovered 3 years later [41].

Gell-Mann and Zweig independently suggested in 1964 that the Eightfold Way structure could be derived from combinations of three fundamental fermions (and three antifermions), which Gell-Mann christened "quarks" [42, 43]. The baryons ($B = 1$), like the proton, were bound states of three quarks, antibaryons ($B = -1$) contained three antiquarks and mesons ($B = 0$), like the pion, were comprised of quark/antiquark pairs. All of these quark states are collectively called "hadrons". The quarks were named "up", "down" and "strange", with charges, $Q = +\frac{2}{3}$, $-\frac{1}{3}$ and $-\frac{1}{3}$, respectively. The number of strange quarks in a given hadron accounted for its previously described "strangeness", S .

There was a problem with the quark model however: the Ω^- baryon (correctly predicted by the Eightfold Way) was described by a bound state of three strange quarks, each with the same spin. This description violated Pauli's exclusion principle, which states that no more than one fermion in the same system may have the same set of quantum numbers [44]. The solution proposed by Greenberg was the final conceptual step to the current picture of the strong force: the introduction of a new quantum number, which later became commonly known as "colour" [45]. Unlike the familiar single electric charge, there are three possible colour charges, called "red", "green" and "blue", so that each of the strange quarks in the Ω^- baryon state can be differentiated. All of the bound quark states are understood to be colour charge neutral or, continuing the colour analogy, "white". All baryons contain one quark of each colour or one antiquark of each anticolour ($W = RGB = \overline{RGB}$) and mesons are comprised of a quark of one colour and an antiquark of the corresponding anticolour, $W = R\overline{R} = G\overline{G} = B\overline{B}$. The requirement for colourless stable states implies that there can be no stable free quarks. This feature of the strong

force is known as “confinement”.

Suspicion that the quark was only a useful mathematical trick was ended at SLAC in 1969 [46–48]. The three-quark structure of the proton was directly observed by the scattering of electrons on hydrogen nuclei in an experiment analogous to that of Rutherford’s students that identified the nuclear structure of the atom.

The strong force is therefore now understood to describe the interactions of quarks with colour charge fields and is described by Quantum Chromodynamics (QCD), formalised in the early 1970s [49, 50]. Yukawa’s pion exchange remains an effective description of interactions between nucleons but can now be understood as a relatively weak residual effect of QCD analogous to the Van der Waals electromagnetic interactions between molecules.

The QCD Lagrangian is constructed by the now familiar introduction of interactions between free fermion and boson fields to enforce gauge invariance. The massless gauge bosons are named gluons and carry colour charge themselves. It is this self-interaction that accounts for confinement and the short range of the strong force, as discussed in Chapter 3. The existence of gluons was experimentally established in 1979 by the observation of three co-planar jet events ($e^+e^- \rightarrow q\bar{q}g$) by the TASSO experiment at DESY [51].

In order to produce self-interaction terms between the gluons, the strong force boson fields are generated, similarly to electroweak theory (Section 2.3), from a non-Abelian symmetry group, $SU(3)_C$, with generators, $\mathbf{T}^{a=1-8}$, defined by the non-zero commutation relations:

$$[\mathbf{T}^a, \mathbf{T}^b] = i \sum_{c \neq a \neq b}^{1-8} \varepsilon^{abc} \mathbf{T}^c. \quad (2.27)$$

where ε^{abc} are the structure constants.

The QCD covariant derivative is a 3×3 matrix, similar to Eqn. 2.9, which gives eight massless gluon fields, G_μ^a :

$$\mathbf{D}_\mu = \partial_\mu \mathbf{I} + ig_s \mathbf{T}^a G_\mu^a. \quad (2.28)$$

and g_s is the strong coupling constant.

Under $SU(3)_C$, the quark fields form colour triplets, $C = R, G, B$. For the first generation of quarks, these are:

$$u_C = \begin{pmatrix} u_R \\ u_G \\ u_B \end{pmatrix} \quad \text{and} \quad d_C = \begin{pmatrix} d_R \\ d_G \\ d_B \end{pmatrix}. \quad (2.29)$$

The QCD Lagrangian can be written as:

$$\begin{aligned}\mathcal{L}_{\text{QCD}} &= \mathcal{L}_{\text{Gluon}} + \mathcal{L}_{\text{Quark}} \\ &= -\frac{1}{4}G_{\mu\nu}^a G^{a\mu\nu} + \bar{q}^C (i\gamma^\mu \mathbf{D}_\mu - m\mathbf{I})q^C\end{aligned}\quad (2.30)$$

where the gluon field tensors are:

$$G_{\mu\nu}^a = \partial_\mu G_\nu^a - \partial_\nu G_\mu^a - g_S \sum_{b \neq a}^{1-8} \sum_{c \neq a \neq b}^{1-8} \varepsilon^{abc} G_\mu^b G_\nu^c . \quad (2.31)$$

More quarks were predicted, primarily to describe CP -violation in the weak interaction [52–54] and the discoveries followed: the charm in 1972 [55–57], the bottom or beauty in 1977 [58] and finally the top or truth in 1995 [59, 60]. The strong force and all participating particles are now believed to be known and understood. However, the complexity produced by the QCD Lagrangian has led to significant difficulties in the application of this theory to certain observable purposes, as discussed in Chapter 3.

2.5 Higgs-Yukawa interactions

So far, the fermion masses have been added by hand into the Standard Model Lagrangian. In electroweak theory, weak boson masses arise as a coupling between each of the gauge fields and the Higgs, as shown in Eqn. 2.25. It is natural to imagine that a similar coupling between fermions and the Higgs field may be the origin of their masses. These interaction terms resemble Yukawa’s theory of the strong nuclear interaction and so commonly bear his name. For a given fermion, f , the gauge invariant Higgs-Yukawa interaction term can be written (considering only a single fermion generation for simplicity) as:

$$\mathcal{L}_{\text{Higgs-Yukawa}} = -Y_a \bar{f}_L \tilde{\Phi} a_R - Y_b \bar{f}_L \Phi b_R + \text{h.c.} \quad (2.32)$$

where “h.c.” represents the Hermitian conjugate terms. Y are the Yukawa coupling constants between the fermion fields, $f_L = \begin{pmatrix} a \\ b \end{pmatrix}_L$, a_R and b_R , with the Higgs doublet field, Φ , defined in Eqn. 2.22. The alternative gauge-invariant form of this field $\tilde{\Phi}$ is defined as:

$$\tilde{\Phi} = \frac{1}{\sqrt{2}} \begin{pmatrix} H + v \\ 0 \end{pmatrix}, \quad \text{where} \quad \Phi = \frac{1}{\sqrt{2}} \begin{pmatrix} 0 \\ H + v \end{pmatrix} \quad (2.33)$$

and is required to produce coupling to fermions in the upper position of the left-handed doublet: the u quark and the electron neutrino, ν_e (N.B. The small neutrino masses are typically not included in this formalism).

All fermion masses are generated by the vacuum expectation value and each is scaled

by a unique Yukawa coupling, as:

$$m_f \equiv \frac{v}{\sqrt{2}} Y_f = \frac{\sqrt{2} m_W}{g_W} Y_f \quad (2.34)$$

where v can be written in terms of the weak coupling constant, g_W , and the mass of the W boson.

While these interactions provide a consistent framework for particle mass generation in the Standard Model, there are no predictions for the fermion masses as had been the case for the W^\pm and Z^0 bosons (Eqn. 2.26). The Yukawa couplings simply replace the masses as free parameters in the theory. It is when all three fermion generations of the Standard Model are considered that the Higgs-Yukawa model becomes more than a trivial substitution of one set of non-predicted constants for another.

In the three-generation Lagrangian, the Yukawa couplings become 3×3 complex matrices, $\mathbf{Y} = Y_{ij}$, which allows terms that combine (or “mix”) fermion flavours. Here we will focus on the mixing of quark flavours. For the Higgs-generated quark masses to be well defined for each flavour, the Yukawa matrices are substituted for real, diagonal $\mathbf{\Lambda}$ matrices by introducing four unitary matrices $\mathbf{U}_{L,R}^{u,d}$,

$$\mathbf{Y} = (\mathbf{U}_L)^\dagger \mathbf{\Lambda} \mathbf{U}_R = \mathbf{U}_L^\dagger \begin{pmatrix} Y_1 & 0 & 0 \\ 0 & Y_2 & 0 \\ 0 & 0 & Y_3 \end{pmatrix} \mathbf{U}_R \Bigg|^{u,d} \quad (2.35)$$

where the indices 1, 2, 3 indicate the generations of either u - or d -type quarks.

The unitary matrices \mathbf{U} now included in the Lagrangian operate on the quark fields like rotations in “generation” space. These rotations cause complications for the left-handed weak doublets, leading to mixing between u - and d -type quarks. The quark states that participate in the weak interaction are therefore not the same as those with a well defined mass that propagate through space. If we choose to rotate the left-handed states to the up-type mass basis, the doublets $\begin{pmatrix} u \\ d \end{pmatrix}$ must be thought of as $\begin{pmatrix} u \\ d' \end{pmatrix}$, where u identifies both the mass and weak u -type states and d' represents the weak d -type state.

The transformation between the d' -type weak states and the propagating d -type mass states is then given by the unitary CKM matrix, derived by Nicola Cabibbo, Makoto Kobayashi and Toshihide Maskawa [61, 62], so that:

$$\begin{pmatrix} d' \\ s' \\ b' \end{pmatrix} = \mathbf{V}_{\text{CKM}} \begin{pmatrix} d \\ s \\ b \end{pmatrix}, \text{ where } \mathbf{V}_{\text{CKM}} = \mathbf{U}_L^u (\mathbf{U}_L^d)^\dagger = \begin{pmatrix} V_{ud} & V_{us} & V_{ub} \\ V_{cd} & V_{cs} & V_{cb} \\ V_{td} & V_{ts} & V_{tb} \end{pmatrix}. \quad (2.36)$$

It is the existence of the chiral doublet fields in the weak interaction that produces this behaviour. Strong force interactions require no such mixing so the strong states are

equivalent to the mass states. This theory leads to the phenomenon of flavour violation, first observed experimentally for s quarks, discussed later in Chapter 6. Hadronic interactions can produce $s\bar{s}$ pairs, e.g. in the process $\pi^-p \rightarrow K^0\Lambda$ via the strong force, which conserves strangeness, $S(\pi^-p) = 0 = S(K^0\Lambda)$. The resulting strange particles can only decay to lighter hadrons by violating the conservation of strangeness, e.g. $\Lambda \rightarrow p\pi^-$ by an $s \rightarrow u$ quark transition, which is only possible because of generation mixing in the weak interaction. This transition proceeds at a rate suppressed by the matrix element V_{us} , which is small compared to the diagonal intra-generational element V_{ud} [63]:

$$\mathbf{V}_{\text{CKM}} = \begin{pmatrix} V_{ud} & V_{us} & V_{ub} \\ V_{cd} & V_{cs} & V_{cb} \\ V_{td} & V_{ts} & V_{tb} \end{pmatrix} \approx \begin{pmatrix} 0.97 & 0.23 & 3.5 \times 10^{-3} \\ 0.23 & 0.97 & 4.1 \times 10^{-2} \\ 8.6 \times 10^{-3} & 4.0 \times 10^{-2} & 1.00 \end{pmatrix} \quad (2.37)$$

contributing to the long lifetimes of these strange hadrons.

2.6 Free parameters

As we have seen, the SM contains many free parameters that must be measured. A brief consideration of each of them provides a concise summary of the theory.

There are three coupling constants for the gauge fields $SU(3)_C$ and $SU(2)_W \otimes U(1)_Y$, to describe the fundamental strong, weak and electromagnetic interactions. The Higgs potential contains two free parameters, μ and λ , from which are derived the Higgs mass and the vacuum expectation value (VEV), which gives mass to the weak bosons and to the fermions. There are the masses of the fermions, given by the Yukawa couplings that scale the VEV, as well as the four mixing parameters of the generation-mixing CKM matrix.

In addition, the phenomenon of neutrino oscillations, which is not discussed in this thesis, implies that neutrinos have non-zero mass and requires another mixing matrix with an additional four parameters. So, in total, the SM as it currently stands contains 25 free parameters.

2.7 Unanswered questions in the Standard Model

There are a number of well known open issues in the Standard Model. A selection of these is given below and separated into two categories:

Why? We're not satisfied with that:

1. The SM contains 25 free parameters, in addition to the physical constants c and \hbar , that must be measured from experiment. It is natural to imagine that there could be some underlying theory to relate or define many, if not all, of these parameters.

2. There are three known generations of leptons and quarks. This symmetry is suggestive of some deep relationship between all fermions.
3. Why should there be three generations? There is evidence from LEP for three and only three generations of neutrinos, which is suggestive of a three generation Standard Model, but this result is limited to neutrinos with mass below $m_Z/2$ (and that couple to the Z^0), leaving room for new discoveries [64].
4. Gravity is not included in the SM, i.e. there is no gauge invariant quantum field theory of gravitation.

Hints of new physics from experiment:

1. The early formulation of the Standard Model included massless neutrinos and therefore allowed no lepton flavour mixing analogous to the CKM mechanism for quarks described in Section 2.5. The discovery of neutrino oscillations [15] however, implies non-zero neutrino masses, which remain to be determined.
2. The Higgs boson remains undiscovered, putting into question the SM description of the origin of fundamental particle masses. The Higgs mechanism, outlined in Section 2.3, is one successful example of a theoretical framework for mass generation but there are alternatives, such as additional Higgs fields or Higgs-less models invoking extra dimensions [4, 65], which may become more attractive if the Higgs boson remains undiscovered at the LHC.
3. If General Relativity provides an accurate description of the universe at the galactic scale, astronomical observations suggest that baryonic matter can only account for about 17% of all mass in the universe. The remaining mass is dubbed “dark matter” as the constituent particles do not emit or absorb photons. The only stable, electrically neutral particles in the SM are the neutrinos; however their masses are not believed to be sufficient to explain the observations [63]. The flat universe seen by WMAP, has been explained by a gravitationally repulsive “dark energy”, which must account for 73% of the energy density of the universe and is also outside the Standard Model [66].

The direction taken by extensions to the Standard Model to answer these and other questions has been towards the unification of all fundamental forces, i.e. to show that electromagnetic, weak, strong and gravitational interactions can be described as different manifestations of one gauge symmetry. While the electroweak theory, introduced in Section 2.3, has been successful in relating the weak and electromagnetic interactions, the theory retains two distinct interactions with coupling terms whose relationship, $g_Y/g_W = \tan \theta_W$, must be experimentally determined. Many Grand Unified Theories have been proposed to provide a true unification but there is currently insufficient experimental evidence to

determine the correct approach. Advancement of the Standard Model will require continuing development, hand-in-hand between experiment and theory to propose and perform new tests, such as those now being carried out at the LHC.

Chapter 3

Phenomenological QCD

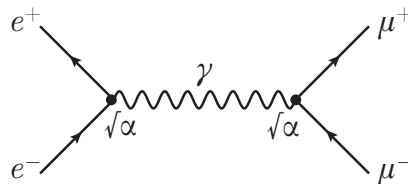
“The predictions of the model are reasonable enough physically that we expect it may be close enough to reality to be useful in designing future experiments and to serve as a reasonable approximation to compare to data. We do not think of the model as a sound physical theory . . .”

– *Richard Feynman and Rick Field, 1978 [67]*

3.1 Practical application of Standard Model theory

The Standard Model is a quantum field theory, as introduced in Chapter 2. The predictions of all physical processes in quantum theory are inherently probabilistic, with fundamental particles understood to exist in a superposition of many possible states until they are observed. A given quantum mechanical process is described mathematically by a complex probability amplitude, \mathcal{A} , of which the absolute value squared, $|\mathcal{A}|^2 = \mathcal{A}^*\mathcal{A}$, represents the probability of that process occurring.

Consider the electromagnetic (QED) process $e^+e^- \rightarrow \mu^+\mu^-$, which may be described through the creation and annihilation of a photon. This process is illustrated by a Feynman diagram with two interaction vertices:



with probability amplitude proportional to the electromagnetic coupling strength $\alpha = e^2/4\pi$. The same process may however be described by more complex diagrams with additional interaction vertices. In fact, the probability amplitude is the sum of all possible

diagrams, e.g.:

$$\begin{aligned}
 \mathcal{A}(e^+e^- \rightarrow \mu^+\mu^-) &= \text{[Diagram: A shaded circle with four external lines]} \\
 &= \alpha \left(\text{[Diagram: A wavy line connecting two vertices]} \right) \\
 &+ \alpha^2 \left(\text{[Diagram: A wavy line with a loop] + [Diagram: A circle with two external lines] + [Diagram: A box with two external lines]} \right) \\
 &+ \dots
 \end{aligned} \tag{3.1}$$

More and more diagrams are drawn for each additional order in α , quickly leading to impractically complex calculations. There are no theoretical grounds to halt the progression to higher orders of α , even up to infinity, which might suggest a serious flaw in QED. The model is however rescued as a useful predictive tool by the weakness of the electromagnetic coupling strength: well known experimentally as the fine structure constant $\alpha \approx \frac{1}{137}$. The probability amplitude of any process can therefore be treated as a perturbative expansion with the contribution of higher order diagrams increasingly suppressed. Calculations need only be made to the level of precision required for a given experiment. The most precise test of QED to date (by determination of the electron dipole moment as discussed in Section 2.2) relies on calculations to $\mathcal{O}(\alpha^8)$.

Electromagnetic processes can therefore be successfully described perturbatively but what about the other SM forces? As described in Section 2.3, electroweak theory links the coupling strengths of electromagnetic and weak interactions, by $e = g_W \sin \theta_W$, to give a small coupling $\alpha_W \approx 4\alpha$. Predictions of weak force mediated processes can therefore also be calculated perturbatively. For the strong force, it must be assumed (considering the confinement of quarks in hadrons) that the QCD coupling strength, α_S , is large and that, consequently, higher order diagrams are not suppressed and calculations seem impossible.

The perturbative approach to predictions of QCD interactions is however rescued (if only partially) by the fact that the SM interaction coupling strengths α , α_W and α_S are not actually constant. The fine structure “constant” α had long been measured as close to $\frac{1}{137}$ in electrostatics experiments; however, no particular value is predicted in the Standard Model. In fact, experiments at e^+e^- colliders, including LEP, have measured a larger value for α of about $\frac{1}{129}$ from interactions involving momentum transfer at the Z^0 mass scale [68].

This change in coupling strength as a function of the momentum transferred by an interaction can be seen, by Heisenberg’s uncertainty principle, as change as a function of the distance scale probed by the interaction, with $\Delta x \sim 1/\Delta p$. This effect can be understood using a new and dynamic quantum picture of the vacuum that highlights the very different nature of the strong and electromagnetic forces. The uncertainty principle allows violation of energy conservation over very short time scales, $\Delta E \sim 1/\Delta t$, so

that the vacuum is understood not to be empty but rather filled with a sea of “virtual” particle/antiparticle pairs that exist only for an instant.

In the case of QED, we can consider a free electron surrounded by this sea of virtual particles. When charged particle pairs appear close to the electron the vacuum becomes polarised, effectively screening the electron’s charge. The electric charge first measured by J. J. Thomson (Section 1.1) was therefore not the true, or “bare”, charge of the electron but rather the effective charge at large distance, screened by the vacuum. In modern high energy collisions, charged particles interact over significantly smaller distances than in Thomson’s cathode ray apparatus, cutting through the vacuum screening to feel more of the bare charge and increase the effective coupling, α .

In a process governed by QCD we consider a single quark surrounded by a sea of coloured particles. There is again a screening effect due to polarised virtual quark/antiquark pairs; however, the self-interactions of the gluons introduce a larger “antiscreening” effect that both changes and amplifies the colour charge of the bare quark [4]. High energy QCD interactions that occur over small distance scales therefore penetrate this antiscreening to feel a reduced effective coupling, α_S . The strong force coupling has been measured at the Z^0 mass scale to be approximately $\frac{1}{8}$ [68]. At this scale and at higher energy scales therefore, perturbative calculations become possible. A precise test of perturbative QCD is made by measurement of the inclusive decay fraction $\mathcal{B}(Z^0 \rightarrow \text{hadrons})/\mathcal{B}(Z^0 \rightarrow e^+e^-)$. Comparison between calculations to $\mathcal{O}(\alpha_S^4)$ and results from LEP show agreement at the 2% level (better than one standard deviation) [69].

For QCD processes below interaction energies of about 1 GeV (the nucleon mass scale), α_S approaches unity, as shown in Fig. 3.1, and perturbative calculations become impractical. Many alternative approaches have been developed to calculate predictions of strong interactions in this non-perturbative regime, including:

Effective field theories: Examples in QCD include Yukawa pion exchange to address nucleon interactions (see Section 2.4) and Heavy Quark Effective Theory (HQET) to describe the structure of hadrons containing c and b quarks. Effective theories approximate a particular process at a characteristic distance/energy scale, ignoring the shorter-range/higher-energy effects of the full theory, which are thought to have minimal influence on that process.

Lattice QCD: The full QCD theory is applied but only to a precision limited by a grid of quantised spacetime coordinates. The separation between nodes on this grid implicitly defines a cutoff at high energy. This model approaches a continuous theory with smaller grid spacing, requiring ever increasing computational demands. Current lattice calculations reproduce \mathcal{T} mass data using a value of α_S that is compatible with the value required by $\mathcal{O}(\alpha_S^4)$ perturbative QCD calculations to match jet production data in e^+e^- collisions [69].

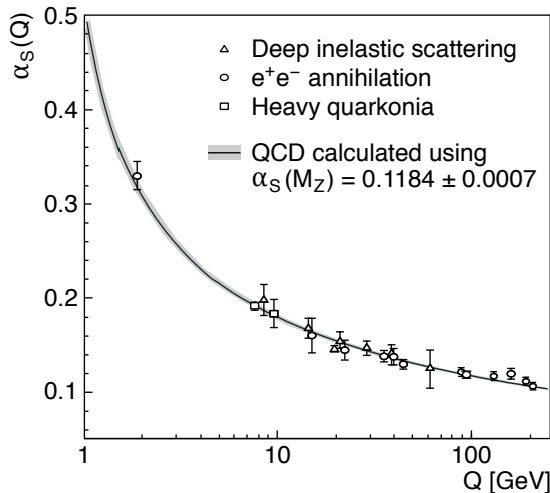


Figure 3.1: A summary of QCD coupling strength, α_s , measurements from experiments at a range of energy scales, Q . These points are compared to a curve from QCD calculations based in the world average value of α_s at the Z^0 mass of approximately $\frac{1}{8}$. [69]

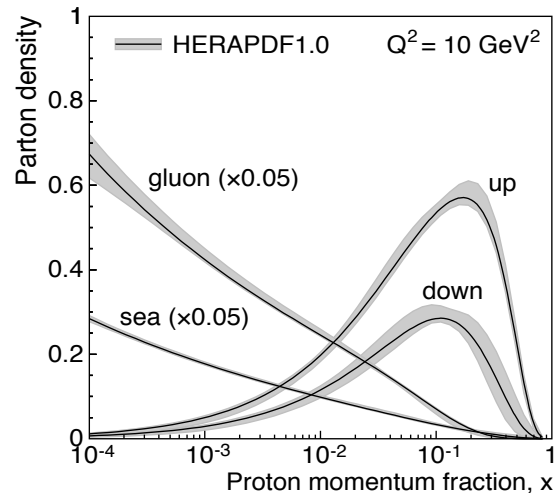


Figure 3.2: Proton PDFs at the interaction scale $Q^2 = 10 \text{ GeV}^2$ from combined experimental results from HERA e^-p collisions. The total proton momentum is shared by the valence u and d quarks with the gluons and “sea” quarks: $u\bar{u}$, $d\bar{d}$, $s\bar{s}$, etc. [70]

Phenomenological models: Various QCD-inspired models have been developed to approximate observed interactions whose description has been theoretically intractable, such as the Lund string model of hadronisation implemented in event generators (see Section 3.2).

The calculation of SM predictions at a high energy hadron collider like the LHC requires both perturbative and non-perturbative methods. Proton-proton collisions at $\sqrt{s} = 7 \text{ TeV}$ can produce hard scattering events at the parton level (i.e. involving quarks and gluons), where the effective coupling is very small. The colliding protons however, as well as the observable final state hadrons, are confined states, bound by interactions with large coupling α_s and requiring a non-perturbative description.

The simplest case is a process where the final state particles are not hadronic, such as Drell-Yan: $u\bar{u} \rightarrow Z^0/\gamma^* \rightarrow l^+l^-$. A calculation of the rate, \mathcal{R} , can be written as:

$$\mathcal{R}(u\bar{u} \rightarrow Z^0/\gamma^* \rightarrow l^+l^-) = \mathcal{R}_p \times f_1(x_1, m_l) f_2(x_2, m_l) \quad (3.2)$$

where the high energy QCD parton interaction and the subsequent weak decay of the Z^0 boson to leptons are calculated perturbatively to give \mathcal{R}_p . The factors f_1, f_2 are non-perturbative “parton density functions” (PDFs) for the quarks at the dilepton invariant mass scale, m_l . The PDFs describe the probability for a parton to carry a fraction, x , of its parent proton’s momentum and depend on the energy scale of the proton interaction. These PDFs constitute process-independent descriptions of the proton’s internal structure and are determined from scattering experiments (see Fig. 3.2).

The additional complexity of final state hadrons in a process such as $u\bar{u} \rightarrow Z^0/\gamma^* \rightarrow q\bar{q}$ is addressed by the inclusion of “parton fragmentation functions” (PFFs). These functions represent the probability that the quark or the antiquark produced in the hard process “fragments” into a particular meson or baryon state, carrying a certain fraction of that hadron’s momentum. PFFs are understood to describe the combined effects of a number of underlying processes, as discussed in Section 3.2, that can each be modelled to calculate predictions for comparison with experimental results.

Accurate predictions of the Standard Model are essential for the search for new physics at the LHC. These predictions require extrapolation of the empirical PDFs to the new high energy scale. The validity of these extrapolations, as well as that of the models used to calculate PFFs, must be tested by the LHC experiments to establish a benchmark for future discoveries.

3.2 Generators

3.2.1 Introduction

The fundamentally probabilistic nature of Standard Model interactions and the use of probability density functions to model them preclude the calculation of any individual instance of a physical process, as introduced in Section 3.1. Instead, statistical sampling methods known as “Monte Carlo” (MC) simulations have been developed to estimate the expected outcome from a large number of similar processes, or “events”. The software implementations of these methods are known as Monte Carlo event generators and are essential for contemporary High Energy Physics experiments because of their power to relate experimentally measurable variables to the parameters of the SM, or any other theory.

Each stage of a modern experiment’s development, from conceptual design to detection technology choices and optimisation relies on MC generators. Computer simulations, starting from the SM, are used to produce primary interactions in particle collisions and evolve the resulting fundamental particles, through decay processes and hadronisation, to produce the leptons, photons and hadrons observable in a detector. The distinctive small-angle design of LHCb for example was motivated by event generator predictions of the production topology of hadrons containing b -quarks (see Section 4.2).

Generators are typically combined with detector simulations to model the interactions of the outgoing particles with the experimental apparatus to give a signal that can be directly compared with data to estimate efficiencies. This approach allows relatively straightforward testing of alternative theoretical models. At LEP for example, as discussed in Section 2.7, experiments were able to compare the measured inclusive hadronic decay fraction of the Z^0 boson to theoretical predictions of the number of light SM neutrino

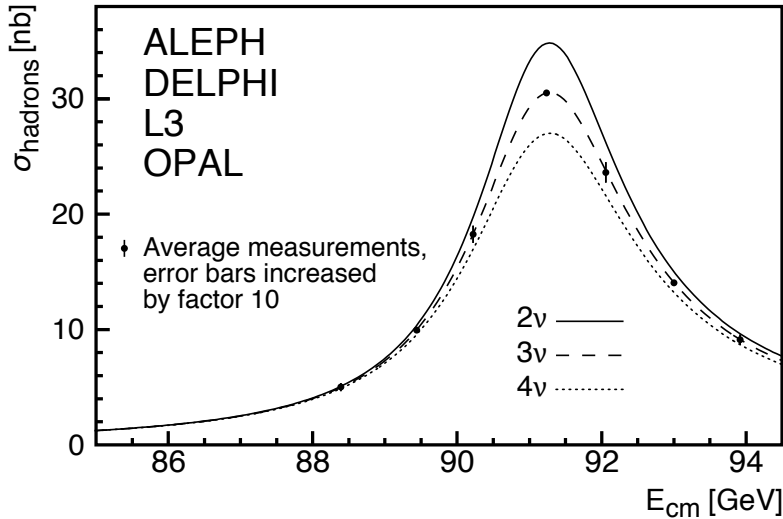


Figure 3.3: The inclusive hadron production cross section around the Z^0 resonance measured by the LEP experiments. Theory curves indicate the predicted cross sections for two, three and four light SM neutrino generations. The efficiency-corrected data strongly favour the three-generation hypothesis. [68]

families. As shown in Fig. 3.3, the data agreed with a three family hypothesis.

In this chapter discussion of specific aspects of event generators will be made with reference to PYTHIA 6 [71], a general purpose event generator used extensively by the HEP community, including the LHCb collaboration.

3.2.2 Primary interactions at a proton-proton collider

At the high centre-of-mass energy of a pp collider like the LHC, the proton beams effectively become beams of partons: quarks and gluons. Collisions involve large momentum transfer (“hard”) quark-quark, gluon-gluon or quark-gluon interactions, which can be calculated using perturbative QCD. The momentum of the protons is shared among their constituent quarks and gluons, as defined by the probabilistic parton density functions (PDFs), e.g. Fig. 3.2 in Section 3.1.

In the quark model, protons consist of three “valence” quarks, uud . High energy parton interactions however, are also sensitive to the virtual quark/antiquark pairs created from the vacuum, which are labelled “sea” quarks in Fig. 3.2. It is therefore possible for proton collisions to involve antiquarks, \bar{u} or \bar{d} , and even the heavier quark flavours; most abundantly strange, s and \bar{s} (the third lightest quark flavour, see Fig. 1.1). In high energy collisions therefore, it is useful to generalise the valence quark picture of the proton from a fixed number of quarks ($u = 2$, $d = 1$ and nothing else) to an expected number of each quark flavour, as follows:

$$\langle u - \bar{u} \rangle = 2, \quad \langle d - \bar{d} \rangle = 1 \quad \text{and} \quad \langle s - \bar{s} \rangle = 0, \quad \text{etc.} \quad (3.3)$$

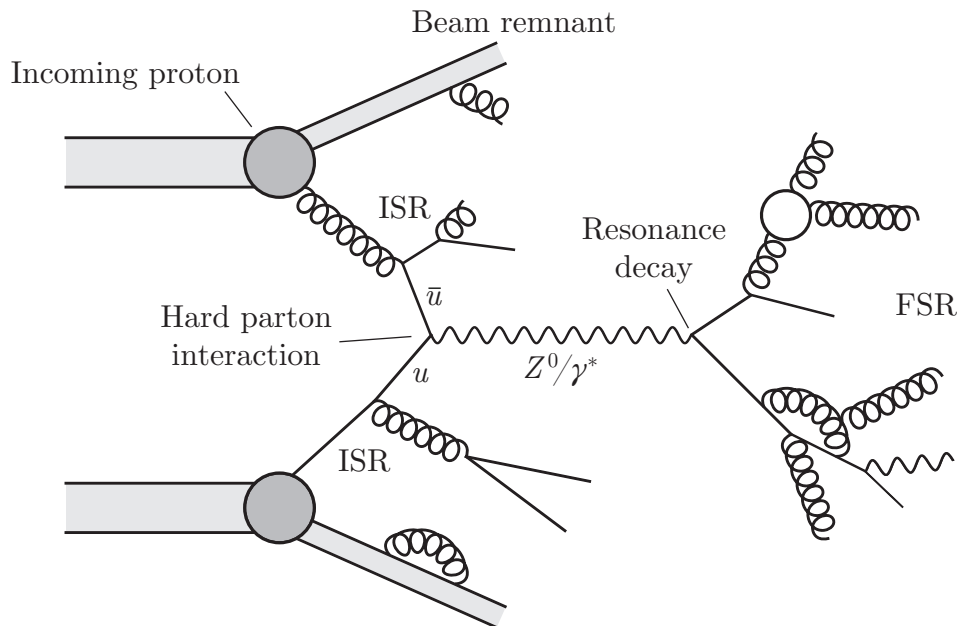


Figure 3.4: An illustration of a high energy proton-proton collision produced by an event generator. Initial State Radiation (ISR) parton showers are induced by the proximity of the incoming proton colour fields. Partons from each shower collide in a hard interaction to produce a resonance, e.g. $u\bar{u} \rightarrow Z^0$. The resonance may decay to quarks, leading to Final State Radiation (FSR). The beam remnants continue on after the collision.

A primary pp collision is modelled as a sequence of interactions as illustrated in Fig. 3.4. Each step in the event generation sequence is governed by random sampling from phenomenological probability distributions in order to approximate both the average behaviour observed in nature and its variability. Collisions may be categorised as either “elastic” ($pp \rightarrow pp$), “diffractive” ($pp \rightarrow pX$) or “inelastic non-diffractive” (IND), i.e. where neither proton survives. A hard IND scattering event proceeds as follows:

1. As two protons approach each other their colour fields interact, initiating spontaneous gluon emissions (analogous to Bremsstrahlung), triggering a parton shower called Initial State Radiation (ISR). A seed parton is selected at random from a proton in each beam to begin these showers and is allocated a fraction of its parent proton’s momentum based on experimentally-derived PDFs. The showers are modelled by an iterative branching of quarks and gluons of the form $g \rightarrow q\bar{q}$, $g \rightarrow gg$ and/or $q \rightarrow qg$, where the share of momentum at each branch is determined from a phenomenological probability distribution. The flavour of pair-produced quarks is also selected randomly using phenomenological rules.
2. Partons from each shower can participate in a hard collision, producing a short-lived resonance, e.g. $u\bar{u} \rightarrow Z^0$ in Fig. 3.4. These resonances then decay, either to other resonances, to leptons or to quarks; in the last case leading to a parton shower called Final State Radiation (FSR).

3. The remainder of the partons in the colliding protons continue along after the collision and are referred to as the beam remnant.
4. All of these partons (ISR, FSR & beam remnant) must then hadronise to produce colourless mesons and baryons, as discussed in Section 3.2.3. These hadrons can themselves be unstable, leading to further decays. N.B. There is a huge range of decays allowed in the SM and at LHCb these decays are handled by a specialist software package (see Section 4.2.8).
5. This sequence results in a large number of “final state” particles (leptons, photons and longer-lived hadrons) that can be compared to the particles observable in a detector.

A single event can be further complicated by multiple hard interactions and, to simulate LHC events, multiple primary pp collisions.

The “hard” parton collision in the event may involve more or less of the momenta of the parent protons. Events with the highest momentum transfer are typically of most interest for tests of the SM since more massive particles (maybe the Higgs) can be produced. The lower momentum events are of great interest themselves however, since they involve exactly the same type of processes that occur in the background of the hardest interactions and that can lead to significant corrections to event multiplicity and topology. In the context of a contributing background to a hard interaction, the softer processes are known as the “underlying event” (UE) and must be well understood in order to properly calculate corrections to those hard interactions. While, for example, the rate of production of high momentum Z^0 resonances may be well predicted by perturbative SM calculations, inaccurate modelling of the UE (i.e. the ISR in the case of Fig. 3.4) may lead to poor predictions for transverse momentum and rapidity distributions of the Z^0 bosons.

Experimentalists commonly refer to the study of soft events as minimum bias (MB) physics, since these events are readily observable in a detector without the need for any selection criteria, or bias (see Section 4.2.8 on LHCb’s trigger). In practice, this loose definition means that a MB data set will include elastic and diffractive scattering events as well as the soft IND interactions that are most comparable to the UE. This inclusiveness can be problematic for comparisons of MB data with the predictions from event generators such as PYTHIA 6, which treat each collision type separately (as discussed in Chapter 6).

3.2.3 Hadronisation and strange quark production

The process by which the quarks and gluons created in hard scattering events and parton showers evolve into the colourless mesons and baryons observed by experiments is known as hadronisation. This process is fundamentally non-perturbative since the creation of hadrons requires quark confinement, i.e. involving low momentum transfer interactions

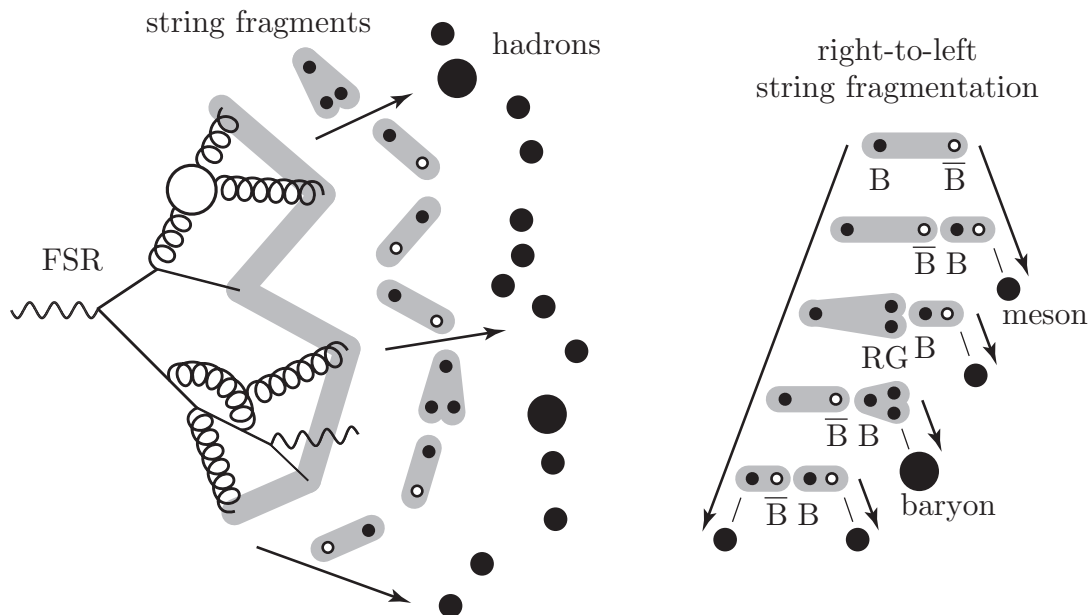


Figure 3.5: An illustration (left) indicative of the hadronisation of FSR via a Lund colour confinement string, which links all final state coloured objects. Iterative string breaking (right) leads to colourless meson and baryon production.

with large coupling, α_S . Calculations based on the QCD Lagrangian are therefore impractical or even impossible and phenomenological models must be employed.

The most common approach used currently in HEP is the Lund model of “string fragmentation”, as implemented in the PYTHIA 6 event generator [71, 72]. This model describes the gluon field between two coloured partons as a linear potential, $V(r) = \kappa \cdot r$, where r is the distance of separation between the partons and κ , the string constant, is taken to be approximately 1 GeV/fm in agreement with experimental observations.

All of the coloured objects produced from ISR, FSR and in the beam remnant are connected by these strings. As the partons move away from each other and the string stretches, the potential energy of the string becomes sufficient to give mass to (or “realise”) a virtual colour/anticolour pair produced at random from the vacuum. This pair acts to screen the colour fields of the adjacent objects, effectively snapping the string as shown in Fig. 3.5.

In this model, the production of a diquark is equivalent to that of an antiquark since their colour charge can be equivalent, e.g. $RG \equiv \bar{B}$. The appearance of a quark/antiquark pair leads to meson production and baryons are produced when a quark/diquark pair is created. The relative rate of diquark appearance and therefore of baryon production is a tuneable parameter in PYTHIA 6.

Each new parton takes some fraction of the string energy, modelled by a phenomenological distribution with free parameters to be tuned. The string repeatedly snaps until the remaining parton momentum transverse to the string is insufficient to extend the string to breaking point, i.e. until the energy contained in the string is less than the mass of the

lightest hadron, the pion. String fragmentation is modelled as a sequence in PYTHIA 6, starting from one end of the string (shown from left-to-right in Fig. 3.5). The choice of starting point is reported to be arbitrary, having no probabilistic impact on the number or kinematic distributions of hadrons produced by the Lund model [71].

The relative appearance rate of higher mass quark flavours is suppressed in the string fragmentation model. The suppression factors are calculated by analogy with a quantum tunnelling process through a linear potential and are given as:

$$u : d : s : c \approx 1 : 1 : 0.3 : 10^{-11} \quad (3.4)$$

so that effectively only u , d and s quarks are produced in hadronisation. PYTHIA 6 treats the flavour suppression factors for $s\bar{s}$, etc. as free parameters to be tuned to experimental results.

The study of strangeness production is therefore an essential goal for the LHC experiments in order to validate the hadronisation step of event generator predictions at the new high energy frontier. In Chapter 6, I present LHCb's measurements of the strange particle production ratios:

- $\bar{\Lambda}/\Lambda$: This particle/antiparticle ratio, measured as a function of rapidity, y , provides information on the changing regime from soft proton excitations at large y , where Λ production is favoured by valence quark inheritance ($uud \rightarrow uds$), to hard parton showers at small y , where the production ratio approaches unity.
- $\bar{\Lambda}/K_S^0$: Both $\bar{\Lambda}$ and K_S^0 hadrons contain antiquarks created from sea quark interactions and/or parton showers so their ratio is a direct measurement of the baryon-to-meson suppression factor in hadronisation.

Chapter 4

The LHCb experiment

4.1 CERN and the Large Hadron Collider

“The Organization shall provide for collaboration among European States in nuclear research of a pure scientific and fundamental character, and in research essentially related thereto. The Organization shall have no concern with work for military requirements and the results of its experimental and theoretical work shall be published or otherwise made generally available.”

– *Convention for the establishment of a European organization for nuclear research, Article II, Section 1, Paris, 1 July 1953* [73]

4.1.1 A short history of CERN

Heisenberg’s uncertainty principle states that $\Delta x \Delta p \geq \hbar/2$, where \hbar is the reduced Planck’s constant. Therefore, to investigate small distances, Δx , particles must be produced with high momentum, Δp , requiring powerful experimental apparatus. In 1954, 11 European states agreed to establish a centre for fundamental research to investigate the nature of the universe at the very small scale and to share the costs of the complex new machines that would have to be built [73].

The world’s first pp collider and forerunner to the LHC, the 300 m diameter Intersecting Storage Ring (ISR), began operation in 1971. Previously, physicists had fired beams onto fixed targets and the potential to create new massive particles was limited by the conservation of the incident beam’s momentum, by $E^2 = m^2c^4 + p^2c^2$. With two counter-rotating beams, ISR collisions occurred with zero net momentum and the full energy of the beams could be transformed into matter.

With this and many other technological developments the European Organization for Nuclear Research (CERN) has been the site of key discoveries such as the neutral currents predicted by electroweak unification (Section 2) first seen by the Gargamelle experiment

in 1973 [21]. The W^\pm and Z^0 bosons were discovered by the UA1 experiment at the Super Proton Synchrotron (SPS) $p\bar{p}$ collider in 1983 [31, 32]. The 27 km circumference Large Electron-Positron (LEP) collider was in operation from 1989 to 2000 and was used to prove the existence of three, and only three, generations of light neutrinos that couple to the Z^0 ; the best indication that the three generation picture for matter particles in the Standard Model is correct.

Now in 2011, CERN is supported by 20 European member states and, with participation from more than 80 countries, has become the world's focus for research in fundamental physics.

4.1.2 The Large Hadron Collider

The LHC is the highest energy particle accelerator in the world, currently producing proton-proton collisions at a centre of mass energy $\sqrt{s} = 7$ TeV. Built in the old LEP tunnel 100 m below the Franco-Swiss border, the LHC has the potential to create new high-mass particles that could never have been produced in previous facilities.

The LHC is designed to reach a target collision energy of 14 TeV with a luminosity, L , of $10^{34} \text{ cm}^{-2}\text{s}^{-1}$ [74]. This enormous particle intensity is required to search for undiscovered rare phenomena and for new particles, such as the Higgs boson, by $N = L\sigma\mathcal{B}$, where N is the number of observable events per second, σ is the production cross section and \mathcal{B} is the branching fraction for a given decay. The LHC design could therefore produce the Standard Model $115 \text{ GeV}/c^2$ Higgs at a rate of about 25 each minute in the dominant mode, with $\sigma(gg \rightarrow HX) = 58 \times 10^{-36} \text{ cm}^2$ and $\mathcal{B}(H \rightarrow b\bar{b}) = 71\%$ [75].

These record collision energies require superconducting magnets, which are cooled by liquid helium to an operating temperature of 1.9 K. Charged particles must be accelerated to ultra-relativistic speeds, where energy loss from synchrotron radiation can become an obstacle. This loss is relatively less important for more massive particles, hence CERN has moved from using electrons at LEP to hadrons at the LHC.

The high particle density required to reach this target luminosity precludes the use of antiparticles, which are expensive to create and store, hence the LHC was designed as a proton-proton collider, requiring two accelerating rings to produce opposing orbits. Twin-bore magnets were designed to overcome the space restrictions of the tunnel vacated by LEP, which could use a single ring to accelerate electrons and positrons into collisions.

As with the re-use of LEP's tunnel, CERN has upgraded a number of past accelerators to provide the feed chain for the LHC (Fig. 4.1). Protons, produced from ionised hydrogen gas, are accelerated in stages through the Linac 2 to 50 MeV, then the PSB to 1.4 GeV, the PS to 25 GeV and finally the SPS to 450 GeV before injection at two points into the LHC to produce counter-rotating beams that can both now be accelerated up to 7 TeV.

The LHC is also designed for heavy ion collisions, conducted so far with lead nuclei.

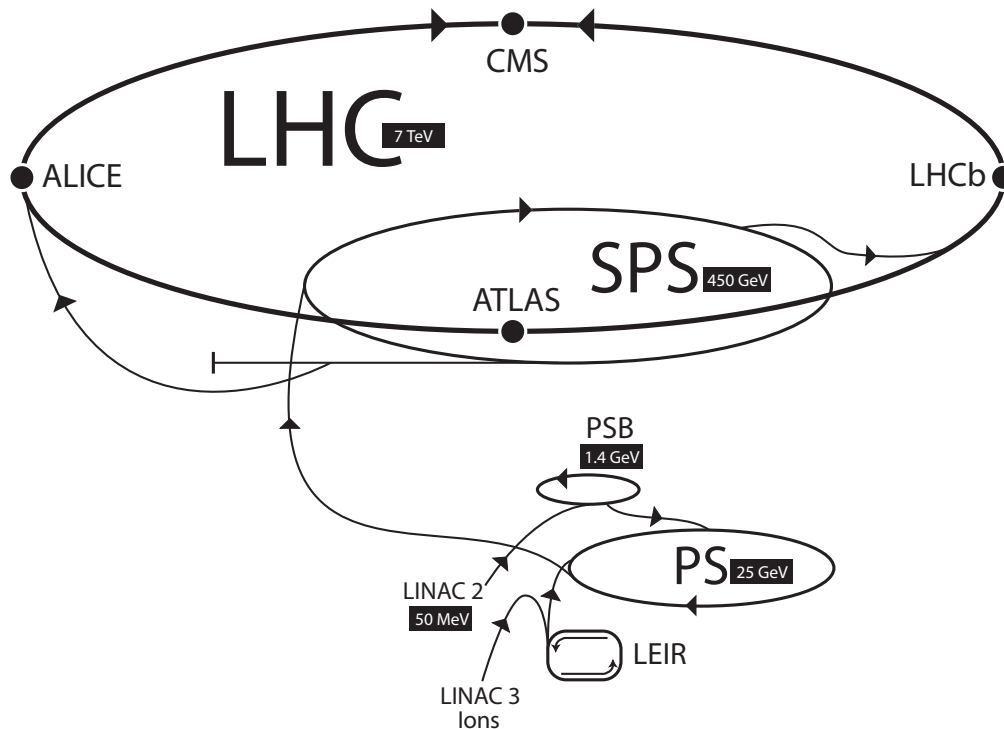


Figure 4.1: The accelerator complex at CERN used to feed protons from ionised hydrogen into the LHC at 450 GeV. The locations of the four experiments are shown at their respective interaction points [76].

High purity lead samples are heated to $500\text{ }^{\circ}\text{C}$ to produce a vapour that is ionised and accelerated through a carbon stripping foil. The ion beam is first accumulated in the Low Energy Ion Ring (LEIR) then accelerated through the same chain used for protons to reach a collision centre-of-mass energy of 2.76 TeV per nucleon pair in the LHC.

The LHC provides four collision points that are each surrounded by a major experiment: ALICE, ATLAS, CMS and LHCb (Fig. 4.1). ATLAS [77] and CMS [78] are general purpose detectors designed to search directly for new particles at the high energy frontier. They are optimised to trigger on events with high transverse momentum objects at large angles to the beamline. ALICE [79] is principally a heavy ion experiment designed to study QCD interactions and the quark-gluon plasma: a proposed new phase of matter in which quarks and gluons are unbound that may have existed in the very early universe. The LHCb experiment and its goals are introduced below.

4.2 The LHCb detector

4.2.1 Introduction

The Large Hadron Collider Beauty (LHCb) experiment was designed to search for indirect evidence of new physics in CP -violation and the rare decays of hadrons containing b (and c)

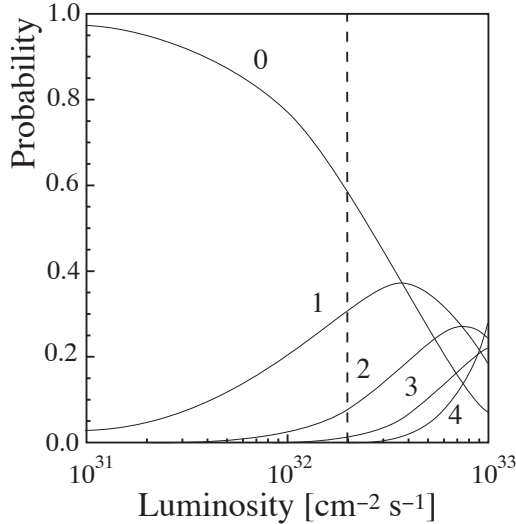


Figure 4.2: The probability of parton interactions as a function of luminosity. Events with a single interaction dominate at LHCb with $L = 2 \times 10^{32} \text{ cm}^{-2} \text{ s}^{-1}$ [83].

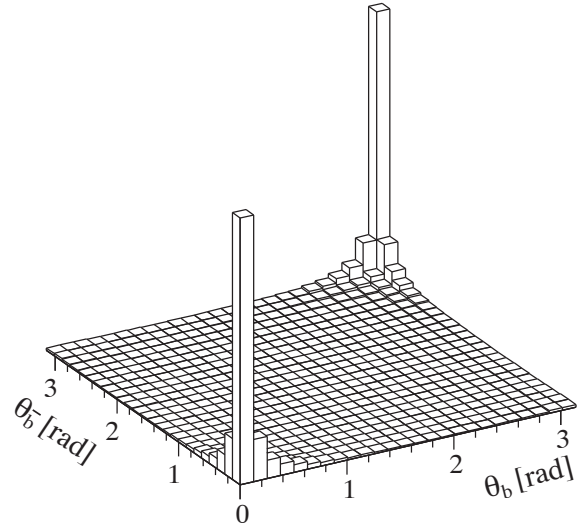


Figure 4.3: The PYTHIA 6 event generator predicts that $b\bar{b}$ pairs are predominantly produced in the same forward or backward cone at small angles to the beamline [83].

quarks. The LHC is the most plentiful source of b -hadrons in the world, with a production cross section, $\sigma(pp \rightarrow b\bar{b}X)$, of $75.3 \pm 5.4 \pm 13.0 \mu\text{b}$ in the forward pseudorapidity region $2 < \eta < 6$, measured at $\sqrt{s} = 7 \text{ TeV}$ by LHCb [80]. This potential for production should be compared to $b\bar{b}$ cross sections of about $1.3 \mu\text{b}$ at the Tevatron (measured at $\sqrt{s} = 1.96 \text{ TeV}$ by CDF [81]) and close to 1 nb at KEKB (measured at the $\Upsilon(4S)$ resonance by Belle [82]).

LHCb was designed to be operated at a modest luminosity $L = 2 \times 10^{32} \text{ cm}^{-2} \text{ s}^{-1}$, compared to the LHC's maximum $10^{34} \text{ cm}^{-2} \text{ s}^{-1}$. This luminosity was achieved in May 2011, making LHCb the first LHC experiment to reach design operating conditions. This luminosity was chosen to maximise the probability of single parton interactions per bunch crossing (Fig. 4.2) to provide the cleanest possible environment for precision reconstruction of multi-body decay chains. This interaction probability results in an average number of visible pp collisions in LHCb, μ , of about 0.4. With experience of actual running conditions and improvements in background rejection, this interaction rate has been increased to an average μ of about 1.0 to 2.5. The luminosity at the LHCb interaction point is tuned by changing the beam focus, which can be done independently from the other interaction points, allowing LHCb to maintain optimal luminosity over a given run and throughout the life of the detector.

Simulations of LHC collisions predict that b - and \bar{b} -hadron pairs are preferentially produced at small angles to the beam axis, with both hadrons boosted into the same forward or backward cone (Fig. 4.3). The LHCb detector has therefore been designed with a small angular acceptance compared to the general purpose machines, from approximately 10 to 300 (250) mrad in the bending (non-bending) plane of the LHCb magnet. Half of these $b\bar{b}$ events are sacrificed with a single arm design that fills the full length of the LHCb cavern

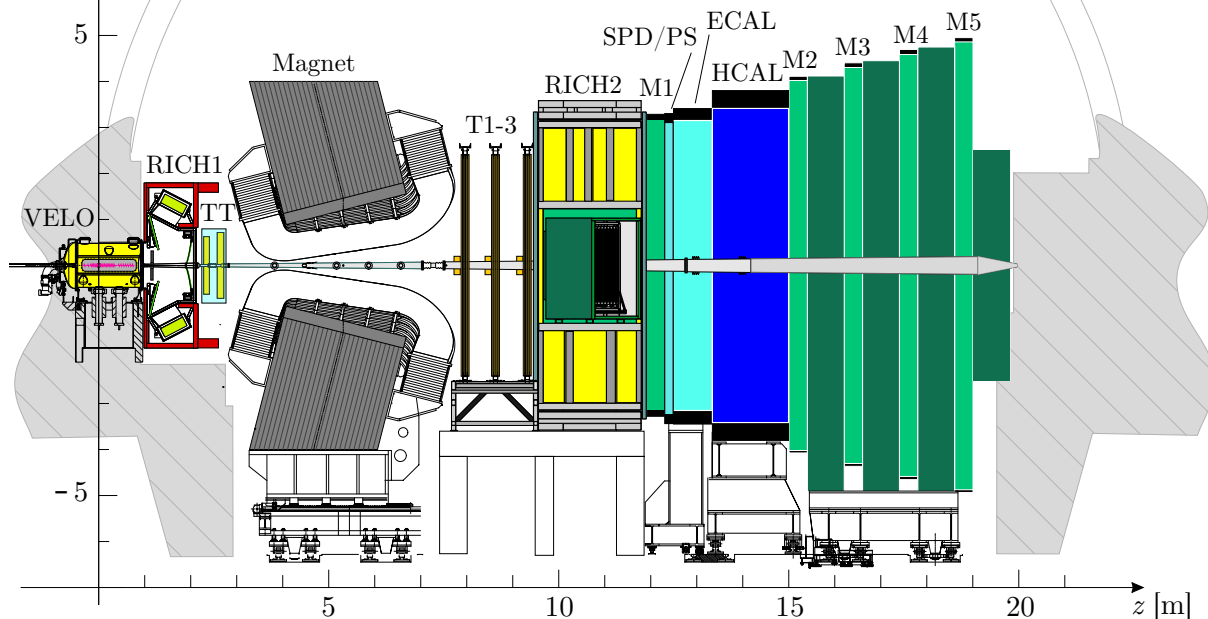


Figure 4.4: A schematic view of the LHCb detector [84].

and improve the momentum resolution of the tracking system.

4.2.2 Detector layout

To identify the characteristic displaced vertices of boosted b -hadron (B) decays, the LHCb experiment employs a specialist silicon vertexing tracker (VELO) around the interaction point. The B decay products are detected by tracking and calorimetry systems and specific decay processes are distinguished by identification (PID) of charged particle species with the Ring Imaging Cherenkov (RICH) and muon detectors. The calorimeters provide PID for photons, electrons and hadrons.

From their origin inside the VELO, the B decay products fly downstream through RICH 1, then a large-area silicon tracker (TT) before traversing the magnet and three further tracking stations, built with a mixture of straw tubes and silicon. Further downstream follows RICH 2 then the electromagnetic and hadronic calorimeters, sandwiched between five Multi-Wire Proportional Chamber (MWPC) muon stations (Fig. 4.4).

The LHCb coordinate system is defined to be right handed with its origin at the nominal interaction point, the z -axis aligned along the beamline towards the magnet and the y -axis pointing upwards. The bending plane is horizontal and the magnet has a reversible field, with the positive B_y polarity called “up” and the negative “down”. Tracks reconstructed through the full spectrometer experience an average integrated magnetic field of about 4 Tm.

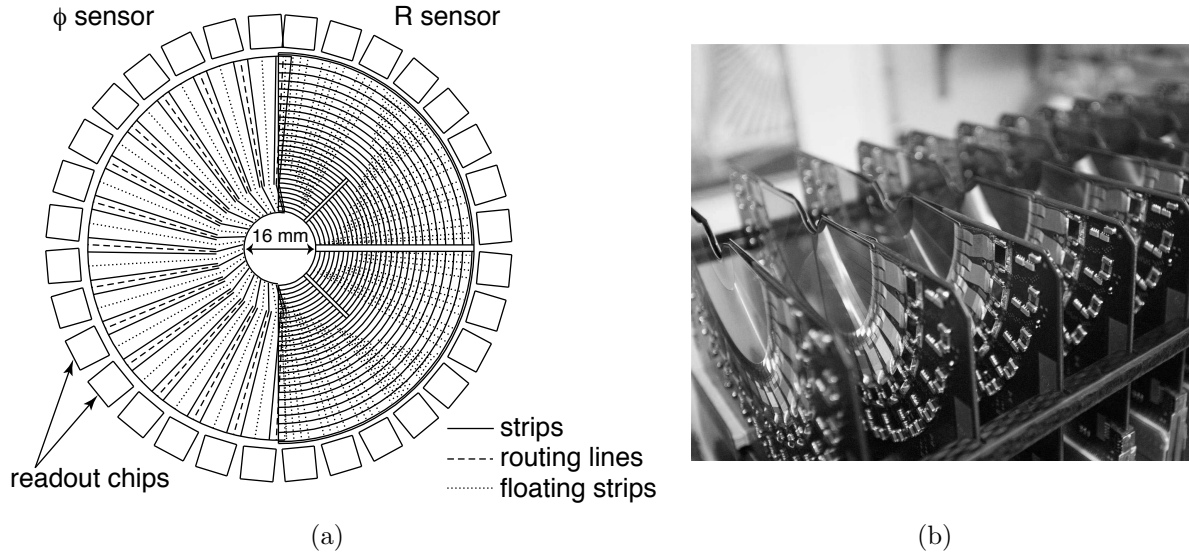


Figure 4.5: (a) A schematic view of the two halves of the VELO stations with r, ϕ geometry [85] and (b) a photograph of the silicon sensors during assembly [86].

4.2.3 Vertex Locator

The primary function of the Vertex Locator (VELO) is to identify the displaced decay vertices of long-lived or highly-boosted particles such as b -hadrons up to about 65 cm downstream of the nominal interaction point. The VELO is also employed to reconstruct primary interaction vertices, identify multiple interaction points and to provide tracking information upstream of the magnet.

To minimise the material between the primary interaction and the VELO sensors, the vacuum environment inside the LHC beam pipe has effectively been extended to accommodate the VELO system within a surrounding vessel. The sensors are separated from the beam by a 300 μm -thick foil of aluminium-magnesium alloy to protect the electronics from beam-induced radio frequency currents. The effects of radiation damage are limited by operating the sensors at -5°C .

The VELO covers the full LHCb angular acceptance. The silicon tracking system comprises 21 stations, each with 2,048 sensors with an r, ϕ geometry, as shown in Fig. 4.5. Each station is comprised of two halves, split horizontally, that are retractable along the x -axis. In normal operating conditions these halves approach the beam with an inner radius of 8 mm. This aperture was enlarged to 18 mm during low energy collisions at $\sqrt{s} = 0.9 \text{ TeV}$ to accommodate the broadened beam. During LHC injection, the VELO stations are retracted to 30 mm to bring the sensors into the shadow of the beam pipe and protect the electronics in case of beam instabilities.

From preliminary measurements, the primary interaction vertex resolution was determined to be $\sigma(x, y, z) = (16, 15, 90) \mu\text{m}$, with a cluster finding efficiency of 99.8%, and a best single hit precision of 4 μm at the optimal track angle [87]. This performance is close to expectations from Monte Carlo simulation, where the measurable precision on

the lifetime of a B is about 50 fs [84].

4.2.4 Tracking

The tracking system relies on a warm dipole magnet with peak field $B_y = 1.1$ T to bend charged particles in the x - z plane for momentum measurements. The magnet aperture encompasses the full LHCb angular acceptance from 10 to 300 (250) mrad in the bending (non-bending) plane. The aluminium coils and iron yolk weigh a total of 1,554 tons. Upstream of the magnet, tracking information is provided by the VELO and silicon Tracker Turicensis (TT) and the downstream tracking provided by three T-stations (T1-3), each comprised of a silicon Inner Tracker (IT) and Outer Tracker (OT) drift tubes. The field strength drops away from the centre of the magnet, out towards the VELO and T-stations, therefore momentum measurements are typically made by matching relatively straight upstream and downstream track segments to form “long” tracks, as illustrated in Fig. 4.6. These long tracks feel an average integrated field of 4 Tm over the full length of the tracking system.

The TT and IT stations are each built from four layers of silicon microstrips with active surface areas of 8.4 m² and 4.0 m² respectively. These layers are arranged i - j - k - i , with vertical strips for the two i layers sandwiching layers with strips rotated by $+5^\circ$ and

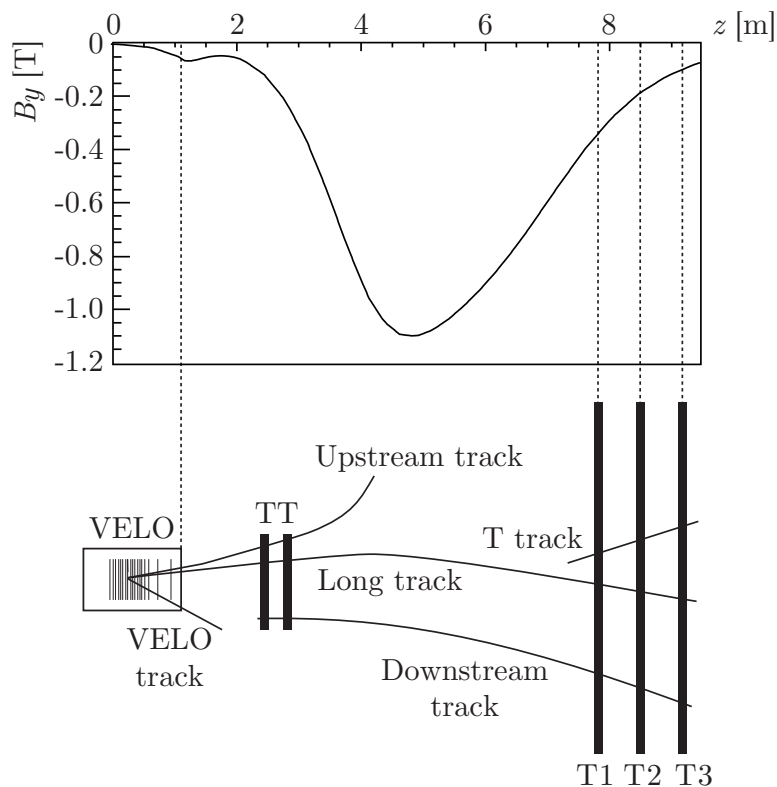


Figure 4.6: An illustration of the various track types: VELO, upstream, long, downstream and T-tracks. The evolution of the magnetic field strength, B_y , is given along the z -axis [84].

-5° about the z -axis for j and k respectively to enhance spatial resolution. These stations operate at below 5°C to slow the damaging effects of radiation. The OT drift tubes cover an active area of 29 m^2 and are filled with a gas mixture of 70 % Argon, 28.5 % CO_2 and 1.5% O_2 , resulting in a drift time of 50 ns. Each station is comprised of four layers oriented in the same i - j - k - i scheme as the silicon detectors.

The single hit resolution for both TT and IT has been measured as about $55\ \mu\text{m}$ and the position resolution of the OT drift tubes as $250\ \mu\text{m}$ [88]. This performance is close to expectations from Monte Carlo simulation, where the invariant mass resolution is $10\text{ MeV}/c^2$ for $B_s^0 \rightarrow D_s^- \pi^+$ [84]. The same mass resolution has been measured in data as about $18\text{ MeV}/c^2$ [89].

4.2.5 RICH particle identification

The discovery of Cherenkov radiation and the subsequent development of Ring Imaging Cherenkov (RICH) detectors for Particle Identification (PID) is discussed in Chapter 5. The principle is as follows: an electrical insulator (or “radiator”) will produce light at a particular angle, θ_C , to the trajectory of a charged particle passing through it with superluminal velocity, $v > c/n$, where c is the speed of light in a vacuum and n is the refractive index of the radiator. Measurement of this angle allows calculation of the particle velocity, by $v = c/(n \cos \theta_C)$. Combined with a momentum measurement from the tracking system, the particle’s mass and therefore species can be determined. RICH detectors use spherical mirrors to focus Cherenkov light to a ring, the radius of which is a function of θ_C and the detector geometry.

PID is essential for much of the LHCb physics programme, particularly for the distinction between pions and kaons, in order to separate similar decays such as $B_{(s)}^0 \rightarrow \pi^+ \pi^-$, $K^\pm \pi^\mp$ or $K^+ K^-$. In MC simulations of these decays, final state hadrons produced at large angles to the beam have a softer momentum spectrum than those produced at small angles, as shown in Fig. 4.7 for $B^0 \rightarrow \pi^+ \pi^-$. A two-detector system has therefore been designed, with RICH 1 able to identify low momentum particles (down to about $2\text{ GeV}/c$) over the full angular coverage of LHCb and RICH 2 focussed on high momentum tracks (up to about $100\text{ GeV}/c$) in a narrower acceptance from 15 to 120 (100) mrad in the bending (non-bending) plane. RICH 1 is installed upstream of the magnet and RICH 2 downstream, as shown in Fig. 4.4. The magnet sweeps low momentum particles out of the RICH 2 acceptance resulting in a lower occupancy.

Cherenkov angle increases with particle velocity up to a maximum, where $v \rightarrow c$, known as the saturation angle, $\theta_{\text{sat}} = \arccos(1/n)$. This angle is a function of the radiator refractive index only, i.e. is independent of the mass of the charged particle; so, at saturation, a RICH detector can no longer distinguish between particle types. Three complementary radiators are therefore employed to provide PID over the required momentum

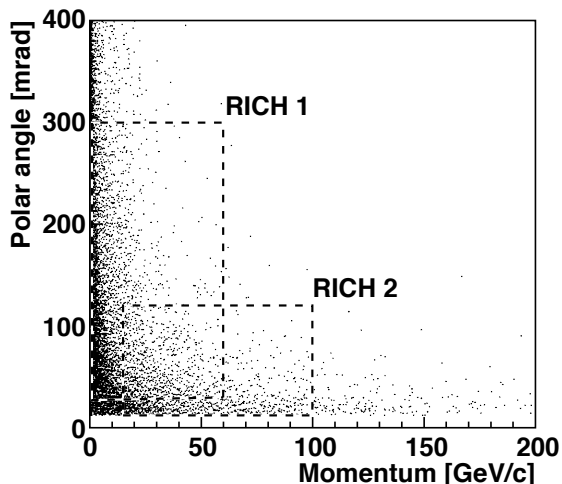


Figure 4.7: Polar angle as a function of momentum for MC generated pions from $B^0 \rightarrow \pi^+\pi^-$. Low momentum, large angle pions are identified by RICH1 and high momentum, small angle pions by RICH 2 [90].

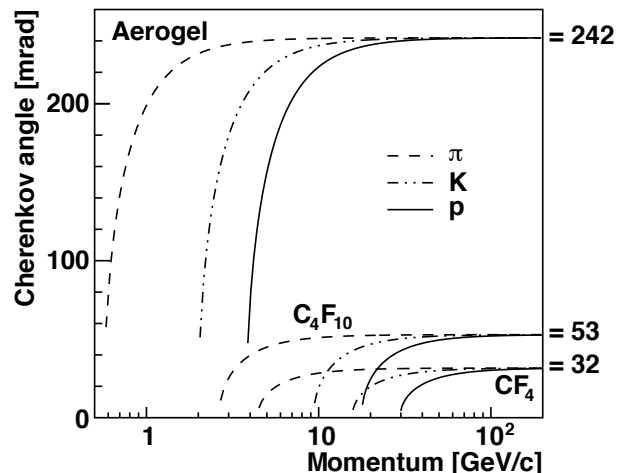


Figure 4.8: Cherenkov angle for relativistic charged π , K and p as a function of momentum. The saturated ($v \rightarrow c$) angles are given for the three LHCb RICH radiators: aerogel, C_4F_{10} and CF_4 .

range: silica aerogel & C_4F_{10} gas in RICH1 and CF_4 gas in RICH2, with refractive indices $n = 1.03$, 1.0014 and 1.0005 respectively, for photons of wavelength $\lambda = 400$ nm. The distributions of θ_C as a function of momentum are given for pions, kaons and protons for the three radiators in Fig. 4.8.

To minimise the material budget, the focusing spherical mirrors of both RICH detectors are split into two surfaces, each tilted to reflect the Cherenkov light on to a flat mirror plane and out to photon detectors installed outside the spectrometer acceptance, as shown in Fig. 4.9 for a cosmic ray event. In RICH1, the banks of photon detectors are separated vertically and in RICH2 horizontally. The RICH1 (2) spherical mirror surfaces are comprised of 2 (28) segments with the flat planes assembled from 4 (20) mirrors. The spherical mirrors in RICH1 (2) are built on a carbon fibre reinforced polymer (glass) substrate, with support outside the acceptance. The total material contributions of RICH1 and RICH2 are 0.08 and 0.15 radiation lengths, respectively.

Novel Hybrid Photon Detectors (HPDs) have been developed in collaboration with industry, combining a vacuum tube with pixel readout, described in Refs. [92, 93]. A photon incident on the quartz window produces an electron by the photoelectric effect in a photocathode layer deposited on the window surface inside the vacuum tube. The electron is accelerated across an 18 kV potential to a silicon pixel chip cathode, as shown in Fig. 4.10. This device is sensitive to single photons and the multialkali photocathode gives sensitivity for wavelengths from 200 to 600 nm, with a peak quantum efficiency of approximately 30%. The 1,024-pixel chip with binary readout provides a demagnified 2.5×2.5 cm² resolution on the entrance window. On average, photons arrive with normal incidence to the HPDs, which are arranged in planes with hexagonal close packing to cover

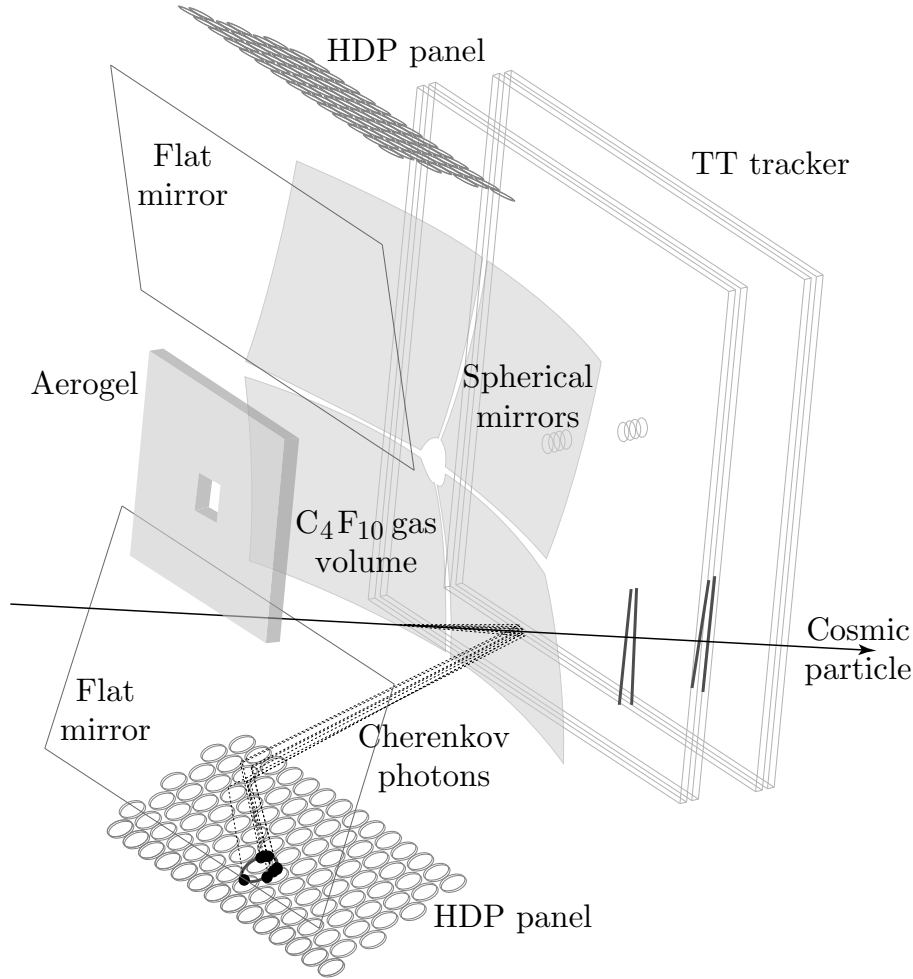


Figure 4.9: A cosmic event reconstructed in RICH 1. A charged track emits a cone of Cherenkov light on passing through the C_4F_{10} gas radiator. Mirrors focus these cones to rings on two banks of photon detectors positioned outside the LHCb acceptance [91].

a total area of about 3.5 m^2 with an active fraction of 64%. The detector arrays provide close to complete geometrical acceptance for Cherenkov photons produced in both gas radiators and about 68% for aerogel. RICH 1 (2) employs 7 (9) columns of 14 (16) HPDs in both photon detector panels.

Electron trajectories inside the HPDs are highly sensitive to an external magnetic field, so each tube is protected from the fringe field of the LHCb magnet with a 1 mm-thick cylindrical casing of nickel-iron alloy. The maximum field in the region of the detector planes is 60 mT in RICH 1 and 15 mT in RICH 2. This shielding is sufficient for optimal operating conditions ($\leq 3\text{ mT}$) in RICH 2, however RICH 1 requires additional protection provided by iron plates that enclose the photon detector arrays as described in Ref. [94].

The RICH system is currently operating at close to design expectations. The PID performance as well as aspects of the initial calibration are presented in Chapter 5.

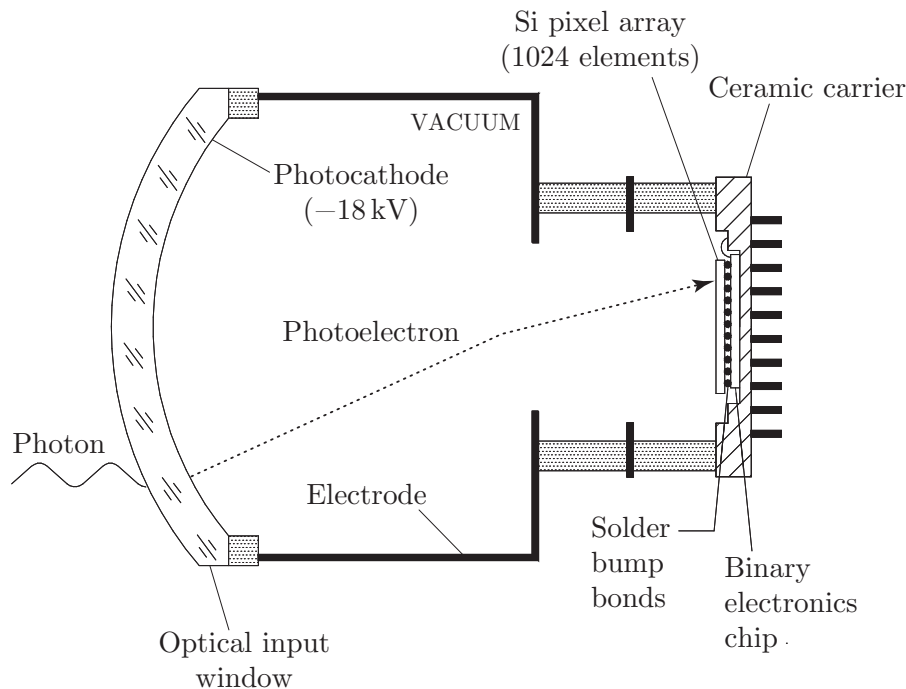


Figure 4.10: Schematic view of an HPD. Single photons are observed by production of a photoelectron that is accelerated across an 18 kV potential and focused onto a silicon pixel sensor [90].

4.2.6 Calorimetry

The calorimetry system is designed to identify photons, electrons and hadrons as well as to provide energy and position measurements. The system is comprised of the Scintillating Pad Detector (SPD), Pre-Shower (PS), Electromagnetic Calorimeter (ECAL) and Hadron Calorimeter (HCAL). Each detector employs polystyrene scintillating tiles that are sensitive to the passage of charged particles. Neutral particles are indirectly observable by the showers of charged particles produced from interactions with layers of lead or iron absorber. The scintillation light is read out through wavelength-shifting fibres to Photomultiplier Tubes (PMTs).

The SPD and PS scintillating layers are separated by a 14 mm-thick lead absorber, equivalent to two radiation lengths (X_0) or 0.1 interaction lengths (λ_I), and are used to distinguish between electrons, photons and pions. Electrons produce a minimum ionising particle (MIP) signal in the SPD and shower through to the PS. Photons are detectable only by the shower after the absorber. Pions will not shower over this short interaction length and produce a MIP signal in both scintillators.

The ECAL and HCAL are both designed to measure energy, following the “shashlik” (Russian for “kebab”) model. Multiple alternating layers of scintillator and absorber detect and contain the entire shower for the best energy estimate. The ECAL has a thickness of $25 X_0$ (or $1.1 \lambda_I$), fully containing electromagnetic showers. The HCAL is the most downstream detector and utilises thicker absorber layers (16 mm iron compared to 2 mm lead in the ECAL), equivalent to $5.6 \lambda_I$. The energy resolutions for both calorimeters are

given in Ref. [95] as:

$$\frac{\sigma_E}{E} \Big|_{\text{ECAL}} = \frac{10\%}{\sqrt{E}} \oplus 1\% \quad \text{and} \quad \frac{\sigma_E}{E} \Big|_{\text{HCAL}} = \frac{80\%}{\sqrt{E}} \oplus 10\% \quad (4.1)$$

where energy is measured in GeV.

The calorimeters cover an angular range from 30 to 300 (250) mrad in the bending (non-bending) plane. This coverage is reduced at small angles to the beam compared to the rest of LHCb to avoid extreme radiation damage from the high flux of particles. Smaller scintillator tiles are installed closer to the beam to reduce occupancy levels and enhance position measurement precision. The SPD, PS and ECAL define three regions: “inner”, “middle” and “outer” with tile areas 16, 37 and 147 cm² respectively. The HCAL defines two regions with tile areas 172 and 690 cm².

The electron identification efficiency has been measured at $\geq 90\%$, with a misidentification rate of 3-5%, for electron momentum above 10 GeV/c [96]. An invariant mass resolution of 7 MeV/c² for $\pi^0 \rightarrow \gamma\gamma$ is close to expectations from Monte Carlo simulation.

4.2.7 Muon detection

A number of LHCb’s key physics goals rely on the reconstruction of decays to muons. A first measurement of the decay rate $B_{(s)}^0 \rightarrow \mu^+\mu^-$ for example, which is predicted to be small in the SM, could reveal an enhancement from new physics [97].

Relativistic muons are essentially stable particles at LHCb, with $c\tau = 659$ m [63]. Muons are extremely penetrating and the muon system is therefore the most downstream detector in LHCb. There are five muon stations separated by 80 cm-thick iron absorbers to stop hadrons and ensure that only muons are detected. The full thickness is equivalent to $20 \lambda_I$.

Most sensitive layers consist of Multi-Wire Proportional Chambers (MWPCs), a technology pioneered at CERN that earned a Nobel Prize for Georges Charpak in 1992 [98]. The primary aim of the muon system is observation of penetrating charged particles; however, these sensors also provide some momentum and energy information. The chambers are filled with a gas mixture of argon, CO₂ and CF₄ in the proportions 40 : 55 : 5, giving a time resolution of 5 ns.

The muon system covers an angular range from 20 (16) to 306 (258) mrad in the bending (non-bending) plane with an active surface area of 435 m². Similarly to the calorimeters, smaller sensitive elements are employed at low angles to the beam to cope with the high flux of particles. The most intense region is the centre of the first muon station and is instrumented with the more radiation tolerant triple-Gas Electron Multiplier (GEM) detectors.

The muon identification efficiency has been measured as close to 97% from $J/\psi \rightarrow \mu^+\mu^-$, for muon momentum over 10 GeV/c. Misidentification rates of about 2% have been

found both for pions from $K_S^0 \rightarrow \pi^+\pi^-$ and kaons from $\phi(1020) \rightarrow K^+K^-$ [99]. There is excellent agreement with Monte Carlo simulation.

4.2.8 Trigger and data processing

In the design phase, the expected bunch crossing rate at the LHC was 40 MHz, with an interaction rate of about 10 MHz at LHCb. About 1% of interactions were expected to produce at least one $b\bar{b}$ pair, with 15% of those interactions containing a b -hadron with all decay products inside the detector acceptance, to give a “ B -physics” rate of about 15 kHz. The typical branching fractions of decays targeted for key physics goals – such as $B^- \rightarrow D^0 K^-$ for the measurement of the CP violation parameter γ [100] – are less than 10^{-3} . A target event storage rate of 2 kHz was planned and a trigger system designed to make this 1-in-5,000 rate reduction while keeping as many of the interesting events as possible.

The trigger comprises two stages: the hardware based Level 0 (L0), using custom electronics, and the software based High Level Trigger (HLT) that allows complete flexibility for future development. The L0 trigger is required to reduce the event rate to 1 MHz, which is the maximum rate that the full detector can be read out as input to the HLT. The final 2 kHz rate is written to storage for later “offline” analysis.

L0 uses information from the calorimetry and muon systems, selecting events with high E_T and/or high p_T particles. Electron, photon and hadron candidates are distinguished in the calorimeters, with each type given prescribed minimum E_T thresholds. Muon and dimuon candidates are selected using p_T measured only by the muon system, which provides a resolution of about 20%. A threshold on the minimum number of hits in the SPD was also used in the earlier periods of operation. The combinations of these criteria and the threshold values have evolved with experience and with the increasing luminosity of the LHC. The total acceptance rate is currently shared between a number of “lines”, or selection criteria, e.g. a small rate is allocated to a loose “minimum bias” (MB) selection, with only 1 event kept for every 10,000 accepted. The remainder of the rate comes from more discriminating lines for b - and c -hadron physics. The L0 decision is synchronised with the LHC 40 MHz bunch crossing rate. To facilitate a high speed result, the electronics are located inside the experiment hall and connected to the detector with optical fibres.

The HLT performs a full reconstruction of the event with a few shortcuts compared to what can be done offline to meet time constraints. The HLT decisions must be made fast enough to accept the input rate from L0 of 1 MHz. Multiple lines run in parallel, some of which are “exclusive”, e.g. with an algorithm specific to the decay $B_s^0 \rightarrow \mu^+\mu^-$, or “inclusive”, e.g. selecting events with a muon plus a high p_T track. These algorithms are written in C++ and run on a farm of commercially available computers at CERN.

The trigger to select minimum bias events used for the V^0 analysis presented in Chapter 6 had a very loose configuration, with L0 in pass-through mode and an HLT requirement of one reconstructed track section in the downstream tracking stations (T1-3).

The full data sets passed by the trigger are stored at CERN and replicated at six computer farms in France, Germany, Italy, the Netherlands, Spain and the United Kingdom. The storage and processing resources at these farms are connected through the Worldwide LHC Computing Grid (WLCG) [101] – or simply the “grid” – with additional processing farms at academic institutions throughout the world. Since the first pp collisions at $\sqrt{s} = 7$ TeV on 30 March 2010, LHCb physicists had executed over 35 million grid jobs, using about 18 PB of disk space and more than 11,000 years of CPU time (Fig. 4.11).

4.2.9 MC simulation

A framework for Monte Carlo event generation and simulation of the LHCb detector has been developed [104]. The primary pp collisions are generated by PYTHIA6 [71] using the Les Houches Accord PDFs [105]. The emerging particles decay via EVTGEN [106], with final state electromagnetic radiation handled by PHOTOS [107]. The resulting particles are transported through a detailed reproduction of LHCb in GEANT 4 [108], which models hits on the sensitive elements of the detector as well as interactions between the particles and the detector material. Secondary particles produced in these material interactions decay via GEANT 4. The output from simulation is directly comparable to experimental data

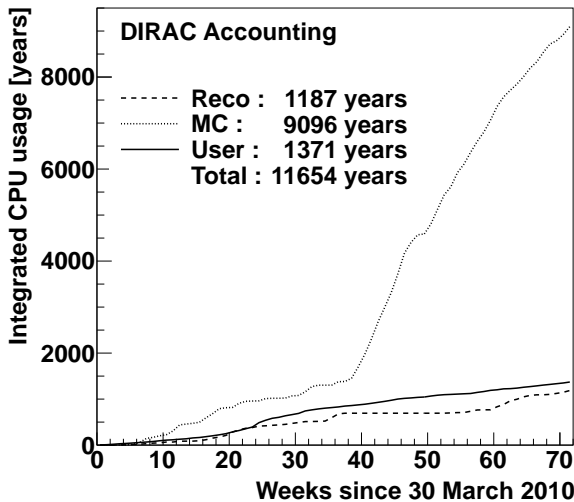


Figure 4.11: The integrated processing time used by LHCb on the grid since pp collisions began at $\sqrt{s} = 7$ TeV, as of 14 August 2011, given for official Monte Carlo (MC) production (“MC” – dotted line) & data reconstruction including reprocessing (“Reco” – dashed line) and physicists’ data analyses (“User” – solid line) [102].

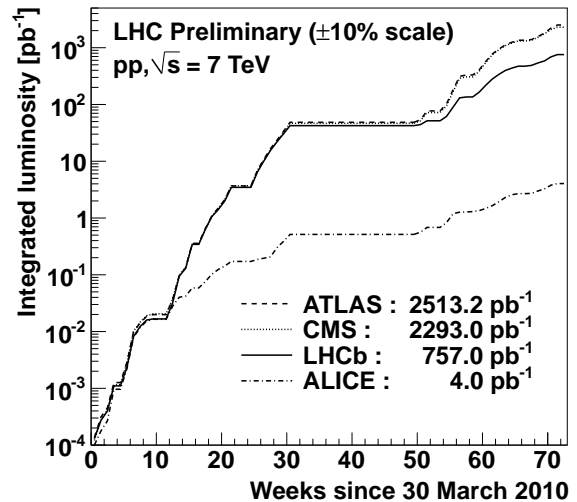


Figure 4.12: The integrated luminosity delivered to ALICE (dashed-dotted line), ATLAS (dashed line), CMS (dotted line) and LHCb (solid line) by the LHC from pp collisions at $\sqrt{s} = 7$ TeV, as of 14 August 2011 [103].

and can be used to evaluate detector performance (see Chapter 5) as well as reconstruction and selection efficiencies (see Chapter 6).

4.2.10 Performance and outlook

The LHC has now run successfully with pp collisions at centre-of-mass energies of 0.9, 2.36 and 7 TeV, as well as with PbPb collisions at a center-of-mass energy of 2.76 TeV per nucleon pair. The vast majority of the pp collisions have been delivered at 7 TeV, with 757.0 pb^{-1} as of 14 August at the LHCb interaction point. The accumulation of integrated luminosity is shown in Fig. 4.12 for all four experiments since the first 7 TeV collisions on 30 March 2010. LHCb has been fully operational to record about 90 % of these collisions. About 1.3 % of the down time results from the need to safely bring the VELO close to the beam after injection. The remainder has been the result of an accumulation of temporary issues with the high voltage and data acquisition systems.

On 1 May 2011, LHCb's design luminosity of $2 \times 10^{32} \text{ cm}^{-2}\text{s}^{-1}$ was reached. The detector has performed better than expected and the instantaneous luminosity is continuing to be increased. As of 14 August 2011, the peak luminosity record at LHCb is $6.3 \times 10^{32} \text{ cm}^{-2}\text{s}^{-1}$. An operational luminosity of $3.5 \times 10^{32} \text{ cm}^{-2}\text{s}^{-1}$ has been chosen and is maintained throughout each run by fine adjustments to the beam crossing angle. The current plan is to continue running the LHC at 7 TeV through into 2012 to collect a sizeable physics data set of $1\text{-}2 \text{ fb}^{-1}$ before shutting down to prepare the machine for collisions at 14 TeV.

Chapter 5

RICH detectors

5.1 An introduction to Cherenkov radiation

“... we made use of the method of visual photometry ... the human eye instead of a light measuring device. ... Notwithstanding its subjectivity and the comparatively large errors in the measurements, this method was at the time the only one that could be used which permitted a quantitative determination of those extremely low light intensities ...”

– *Pavel Cherenkov, Nobel Lecture, 11 December 1958* [109]

The faint blue glow of Cherenkov radiation was first observed by Sergey Vavilov and Pavel Cherenkov in 1934 [110,111] emanating from a bottle of water under the bombardment of γ rays from a radium source. They were able to deduce that this radiation is caused by fast moving charged particles (Compton electrons in the case of this first observation). In 1936 a breakthrough was made towards understanding the production of this light, with the discovery that it is only emitted at a certain angle to the charged particle's path [112]. This observation led Il'ja Frank and Igor Tamm, in 1937, to a theoretical description of the effect [113], which in turn led to a Nobel Prize in 1958 for Cherenkov, Frank and Tamm (Vavilov having died 7 years earlier).

The explanation was based on constructive interference of light and is analogous to the surface bow wave of a boat or the Mach wave (sonic boom) of a supersonic projectile (Fig. 5.1(b)). As a charged particle travels with velocity v through a medium, its electromagnetic field interacts with nearby atoms. In an electrical insulator, this interaction produces a local alignment of polarised molecules adjacent to the path of the charged particle that is restored to equilibrium by photon emission. These photons are emitted isotropically and are usually not observed due to destructive interference. However, if the charged particle is travelling faster than the phase velocity of light in that medium, $v_{\text{phase}} = c/n$ (where c is the speed of light in a vacuum and n is the refractive index),

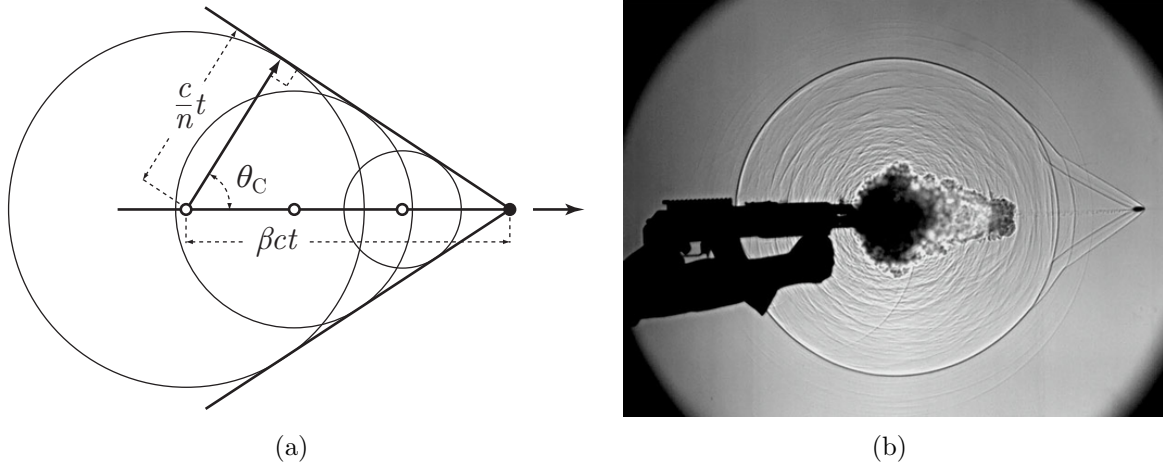


Figure 5.1: (a) A schematic of the Cherenkov light cone and (b) the analogous Mach wave from a supersonic bullet photographed by the shadowgraph method [114].

there is constructive interference at a particular angle to the moving charge, θ_C , and light is observed. This Cherenkov angle opens up with the velocity of the charged particle to a maximum where $\beta (= v/c) \rightarrow 1$ and is given by the following equation:

$$\beta ct \cos \theta_C = \frac{c}{n}t \quad \text{or} \quad \cos \theta_C = \frac{1}{n\beta} \quad (5.1)$$

derived from comparison of the distances travelled by particle and photon in the same time t (Fig. 5.1(a)). This relationship is only valid where $|\cos \theta_C| \leq 1$, i.e. above the superluminal Cherenkov threshold $\beta > 1/n$.

The spectrum of Cherenkov radiation is given by Frank and Tamm as:

$$\frac{1}{h\nu} \frac{dE}{d\nu} = \frac{2\pi L}{c} \alpha Z^2 \sin^2 \theta_C \quad (5.2)$$

where E is the energy emitted as photons with frequency ν , h is Planck's constant, α is the fine structure constant, Z is the charge of the superluminal particle and L is the length of its path through the radiator. The intensity of this light is proportional to its frequency, in agreement with Vavilov and Cherenkov's first observation of a faint blue glow. N.B. In practice this proportionality is complicated by the dependence of a radiator's permeability and refractive index on photon frequency.

With the development of signal amplification technologies such as photomultiplier tubes, Cherenkov detectors quickly became a widely used tool for the study of cosmic rays. In 1957 and '58, Cherenkov counters were launched onboard Sputnik 2 and 3 to record high- Z ¹ cosmic particles [115] and in 2003, balloon-mounted counters were launched to

¹Sputnik 2 carried three independent Cherenkov counters sensitive to particles with $Z \geq 5$, 15, and 34 respectively. An integral counter on Sputnik 3 could be incrementally adjusted to provide sensitivity over the range from $Z \geq 2$ up to $Z \geq 34$.

search for high energy (PeV) cosmic neutrinos by radio-frequency Cherenkov emission from their interactions in the polar ice caps [116–118].

Beyond simply inferring the presence of charged particles by their Cherenkov light, detectors have also been developed to measure θ_C and hence the velocity of charged particles, β . These measurements can be combined with momentum information to calculate the mass (by $p = \gamma m\beta c$, where γ is the Lorentz factor) and so determine the identity of the particle, i.e. pion, kaon or something as yet undiscovered. One such technology is the Ring Imaging Cherenkov (RICH) detector, which uses spherical mirrors to focus the Cherenkov cone to a ring, the radius of which can be easily measured and is related to θ_C by the detector geometry. The concept was pioneered at CERN for the High Energy Physics experiment DELPHI [119], which operated at LEP from 1989 to 2000 and has since been developed for a range of experiments, including LHCb. A RICH device was launched on the penultimate shuttle flight in May 2011 and mounted on to the International Space Station as an integral component of the AMS 2 cosmic particle detector [120]. At LHCb, RICH PID is essential for much of the physics program through the separation of similar decays, such as $B_{(s)}^0 \rightarrow \pi^+\pi^-$, $K^\pm\pi^\mp$ and K^+K^- .

5.2 LHCb's RICH system

Two subdetectors have been developed for the LHCb experiment, described in detail in Section 4.2.5. Three radiators are employed: silica aerogel & C_4F_{10} gas in RICH 1 and CF_4 gas in RICH 2, with complementary refractive indices $n = 1.03$, 1.0014 and 1.0005 respectively (for photons of wavelength $\lambda = 400$ nm). Combined, this system provides charged particle separation over the momentum range 2 to ~ 100 GeV/ c .

The novelty of Ring Imaging Cherenkov detectors, as introduced in Section 5.1, is in their use of focussing mirrors to project the Cherenkov light cone to a ring on an image plane such that the ring's radius (something straightforward to measure) is equivalent to the opening angle of the Cherenkov cone (something hard to measure). Both RICH detectors employ focusing spherical mirrors to reflect the Cherenkov light on to angled flat mirrors and out to photon detector planes positioned outside the detector acceptance. RICH 1 (2) is instrumented with 4 (56) spherical and 16 (40) flat mirrors and 196 (288) hexagonally close packed HPDs.

Though the radius of a ring may be easy to measure, finding the ring itself can be problematic at LHCb, where a typical b -triggered event was predicted to contain up to one hundred reconstructed tracks [121]. In LHCb's reconstruction, this problem was bypassed with a strategy to measure the Cherenkov angle for each photon independently, without ever looking for a ring. This single photon Cherenkov angle is equivalent to the radial distance from the photon to its source track seen on the image plane. A track is only considered to be the source of the photon if this radius falls within the expected range of

a true Cherenkov photon for all possible particle mass hypotheses.

5.3 Geometric alignment

The power of LHCb’s RICH system to distinguish between charged particle species depends critically on accurate knowledge of the positions of its optical components: the mirrors and photon detectors. The position of each component has been measured by survey and included in a simulation of the LHCb detector.

The detector simulation is used to map individual sensor signals from the running experiment on to coordinates in space and time, which are combined (or “reconstructed”) to create the tracks and particles to be used for physics studies (Section 4.2.8). Any discrepancy between this simulation and the real detector will introduce inaccuracies in the reconstruction process. It is therefore critical to establish a procedure to check for any such inaccuracies in the simulated RICH and to correct (or “align”) the simulation to give a more accurate representation of the detector.

To maximise the power of the RICH system, the reconstructed single photon Cherenkov angle precision, σ_C , must be optimised. This precision is limited for each radiator by four dominant sources of uncertainty (Table 5.1):

Emission point: The tilt of the spherical mirror leads to a translation of the photon image on the detector plane dependent on its emission point along the particle track. This dependence is not accounted for in LHCb reconstruction, in which all photons are assumed to originate at the mid-point of a track through the radiator.

Chromatic dispersion: The Frank-Tamm Eqn. 5.2 shows that Cherenkov photons are not monochromatic. Since refractive index is a function of wavelength and by the dependence of Cherenkov angle on refractive index (Eqn. 5.1) not all photons from a given track are produced at a single Cherenkov angle.

Table 5.1: The dominant sources of uncertainty, σ_C , on the measurement of single photon Cherenkov angle for the three LHCb RICH radiators [84].

σ_C [mrad]	RICH 1		RICH 2
	Aerogel	C ₄ F ₁₀	CF ₄
Emission point	0.4	0.8	0.2
Chromatic dispersion	2.1	0.9	0.5
Pixel size	0.5	0.6	0.2
Tracking	0.4	0.4	0.4
Total	2.6	1.5	0.7

Pixel size: Both RICH detectors employ HPDs, photomultiplier tubes with 1024-pixel silicon diode sensors. Each pixel covers a demagnified $2.5 \times 2.5 \text{ mm}^2$ area on the HPD window.

Tracking: A Cherenkov photon is necessarily found in association with a track. The calculation of the angle between the photon and track therefore incorporates the uncertainty on that track's position.

The aim for RICH alignment is to correct the detector simulation to the point where any contribution to σ_C due to differences between the simulated and the real detector is small compared with these four dominant sources.

5.4 Development of an alignment procedure

A procedure is required to establish the accuracy of the detector simulation and, if necessary, to calculate alignment corrections. Previous experiments have used the output of the running RICH detector itself as a source of alignment information [122]. This approach has been tested at LHCb in simulations and with test beam data [123–125].

In the following sections, the effects of misalignments on the output of the RICH are derived and demonstrated in simulations. A procedure is described to measure these effects and correlations are found between the measured values and the magnitudes of particular misalignments. These correlations are used for a test alignment of LHCb's RICH system using simulated collision data.

5.4.1 Observables

A misalignment of a RICH detector is seen on the image plane as a translation of the projected track point away from the ring's centre (Fig. 5.2) and will therefore be observed as a change in measured single photon Cherenkov angle as a function of the position of the photon around the Cherenkov ring, given by the angle ϕ . This change can be written as:

$$\Delta\theta = \theta_C - \theta_0 \tag{5.3}$$

where θ_C is the measured Cherenkov angle and θ_0 is the angle expected from a perfectly aligned system. This dependence of $\Delta\theta$ on ϕ can be derived in terms of the horizontal and vertical components of the translation between track and ring centre on the image plane (θ_x and θ_y in Fig. 5.2) by the cosine rule:

$$\theta_C^2 = \theta_0^2 + \theta_r^2 - 2\theta_0\theta_r \cos(\phi + \psi)$$

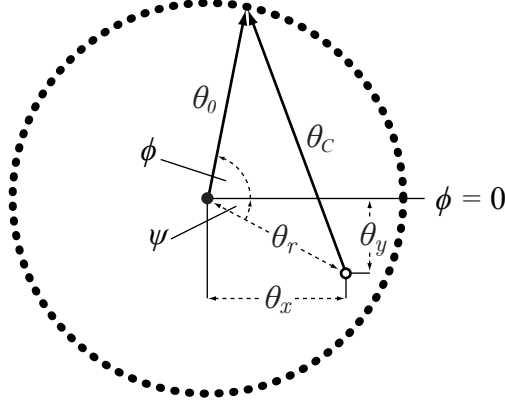


Figure 5.2: An exaggerated misalignment between LHCb's RICH and tracking systems is shown projected on to the photon detector plane as a translation, θ_r , of the track away from the centre of the Cherenkov ring (black dot \rightarrow white dot). For a given Cherenkov photon, this translation results in a change to the measured radius, $\Delta\theta = \theta_C - \theta_0$, which is dependent on ring angle, ϕ .

where ψ is the opening angle of the right-angled triangle formed by θ_x and θ_y . Substituting for Eqn. 5.3 gives:

$$\begin{aligned} (\theta_0 + \Delta\theta)^2 &= \theta_0^2 + \theta_r^2 - 2\theta_0\theta_r \cos(\phi + \psi) \\ \theta_0^2 + 2\theta_0\Delta\theta + \Delta\theta^2 &= \theta_0^2 + \theta_r^2 - 2\theta_0\theta_r \cos(\phi + \psi) \\ \Delta\theta + \frac{1}{2\theta_0}(\Delta\theta^2 - \theta_r^2) &= -\theta_r \cos(\phi + \psi) . \end{aligned}$$

The cosine of the two summed angles can be expanded,

$$= -\theta_r[\cos\phi \cos\psi - \sin\phi \sin\psi]$$

and using the trigonometric relations for the right-angled triangle ($\theta_x, \theta_y, \theta_r$),

$$\begin{aligned} &= -\theta_r \left[\frac{\theta_x}{\theta_r} \cos\phi - \frac{\theta_y}{\theta_r} \sin\phi \right] \\ &= \theta_y \sin\phi - \theta_x \cos\phi . \end{aligned}$$

For small misalignments, i.e. small θ_r and $\Delta\theta$, this equation may be reduced to:

$$\Delta\theta \approx \theta_y \sin\phi - \theta_x \cos\phi . \quad (5.4)$$

5.4.2 Simulations

Misalignments of various components in the RICH system can be simulated within the LHCb software framework (Section 4.2.8). This framework is modular, allowing any step to

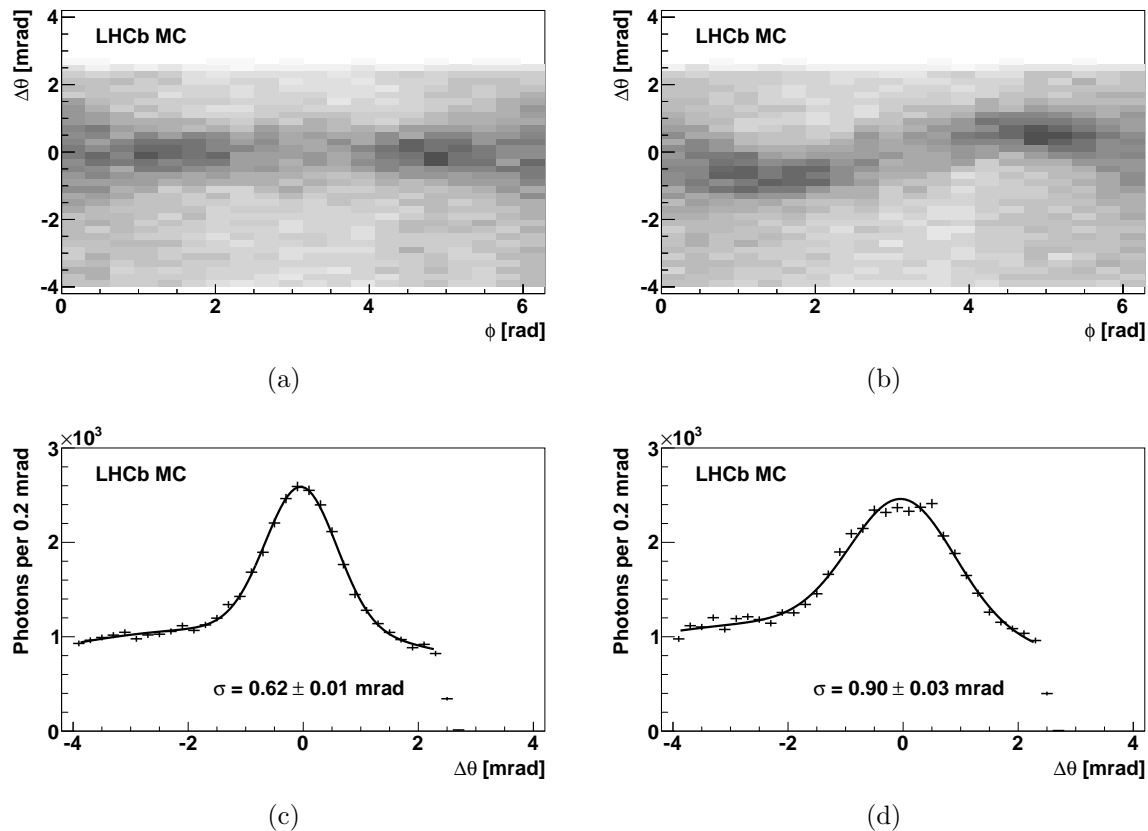


Figure 5.3: Simulated distributions of $\Delta\theta$ as a function of ring angle, ϕ , seen by one panel of HPDs in RICH 2: (a) aligned and (b) with a -3 mm translation of that panel along LHCb’s z -axis with respect to the tracking system. The corresponding degradation in precision is shown by comparison of the $\Delta\theta$ width, σ , which increases by 45 % from (c) to (d). These tests were carried out with a data set of 2,000 L0-passed events, giving some 65,000 Cherenkov photons associated to 3,000 tracks.

be repeated independently with modifications to the detector simulation. MC pp collisions are generated as described in Section 4.2.9 and fed through the detector reconstruction in exactly the same way as real pp collision data. For this study, the reconstruction step to associate HPD hits (i.e. Cherenkov photon candidates) to tracks is repeated with an artificial misalignment added to the simulated RICH geometry. Direct comparisons of the RICH output before and after this misalignment can then be made to show the change to the measured photon Cherenkov angles.

In order to calculate these changes, i.e. measure $\Delta\theta$ for each simulated photon, an expectation of its Cherenkov angle under perfect alignment, θ_0 , is required. This expectation is found from the particle momentum measured by the tracking system, assuming the particle to be a π^\pm meson, by $\beta = p/\gamma m$. In MC events, about 80 % of tracks reconstructed in the RICH detectors are pions. For this study, minimum momentum thresholds of 10 MeV/ c in RICH 1 and 30 MeV/ c in RICH 2 are applied so that θ_0 is close to the saturated Cherenkov angle. The resulting values of $\Delta\theta$ are seen to develop the expected harmonic distributions as a function of ϕ when misalignments are applied, e.g. Fig. 5.3

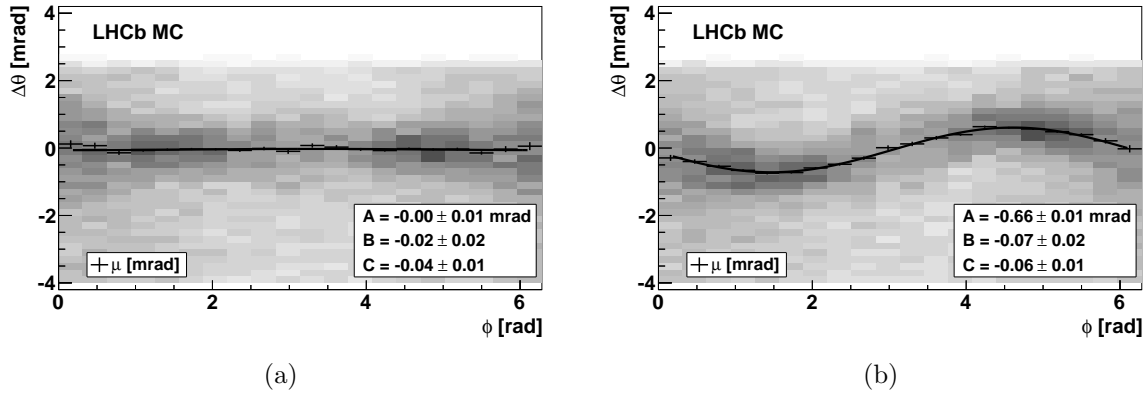


Figure 5.4: Measurement of the misalignment parameters A , B and C from simulated RICH2 output, with (a) no misalignment and (b) a -3 mm translation of the HPD panels along LHCb's z -axis. $\Delta\theta$ is first estimated in each of 20 bins in ring angle, ϕ , by the fitted mean, μ , of a signal Gaussian over a 2nd order polynomial background (error bars). The $\mu(\phi)$ distribution is then fitted with Eqn. 5.5 to extract the amplitudes of $\sin\phi$ and $\cos\phi$. This example -3 mm translation of a RICH2 HPD panel along LHCb's z -axis results in a pure $\sin\phi$ deviation, with amplitudes $A = -0.7$ and B is small.

from (a) no misalignment to (b) translation of a RICH2 photon detector plane by a -3 mm along LHCb's z -axis. The associated degradation of RICH precision is observed in the increasing width, σ , of the $\Delta\theta$ signal peak, e.g. Fig. 5.3 from (c) 0.62 mrad to (d) 0.95 mrad. This example misalignment therefore contributes (in quadrature) a 0.65 mrad uncertainty to the total precision. If this misalignment were present in real data it would be the dominant source of error on measurement of Cherenkov angle in RICH2 (see Table 5.1).

5.4.3 Measurements

Having established in simulation that RICH misalignments do produce the expected sinusoidal distribution of $\Delta\theta$ as a function of ϕ , the next step is to determine, from analysis of these distributions, which components of the RICH are misaligned, by which degrees of freedom and by what magnitudes.

By Eqn. 5.4, measurement of RICH misalignment requires determination of the $\sin\phi$ and $\cos\phi$ amplitudes of the $\Delta\theta$ distribution. Since the RICH detectors cannot determine the Cherenkov angle with perfect precision an intermediate step is required to find an estimate for $\Delta\theta$ at a given value (in practice, range) of ϕ . This estimate is given by the fitted mean, μ , of a Gaussian signal peak over a 2nd order polynomial background, e.g. Fig. 5.3(c). The evolution of $\Delta\theta$ can therefore be followed by μ found in sequential bins of ϕ . The $\sin\phi$ and $\cos\phi$ amplitudes can then be obtained, as shown in Fig. 5.4, from a

fit using the following extension of Eqn. 5.4 with a free offset, C :

$$\Delta\theta = A \sin \phi + B \cos \phi + C . \quad (5.5)$$

With this method in hand, any chosen misalignment can be applied in a series of simulations with a range of magnitudes and the resulting evolution of the alignment parameters, A , B and C , investigated for potential correlations. The first obvious misalignments to study are translations of the photon detector panels since these objects closely approximate the image planes considered in the derivation of Eqn. 5.4.

In RICH 2, for example, the photon detector panels are separated horizontally from the beam line. Their translations along the vertical (LHCb's y -axis) and parallel to the beam (LHCb's z -axis) correspond to orthogonal movements on the image plane (Fig. 5.5(d)). Translations are applied in the range up to ± 3 mm along each axis (all internal components are also moved). The $\Delta\theta(\phi)$ distribution is extracted for photons that see this HPD panel and the resulting changes in the fit parameters A , B and C are measured, e.g. Fig. 5.5(a) to (c). The amplitude A exhibits a linear correlation with translations along LHCb's z -axis with coefficient $r_A = 0.2$ mrad/mm. B shows a similar correlation with translations along LHCb's y -axis. Translations along LHCb's x -axis are perpendicular to the image plane and misalignments in the ± 3 mm range do not produce a measurable change in $\Delta\theta(\phi)$. The fit parameter C is independent of each translation, giving confidence that the small-misalignment approximation used to derive Eqn. 5.4 is appropriate for these tests.

5.4.4 Test exercise

With the correlation coefficients, r_A and r_B , it is possible to calculate corrections to the simulated positions of the HPD panels. As a demonstration, these corrections are found from the 3 mm misalignment amplitudes given in Fig. 5.4 and applied in iterations to independent data samples, each of 2,000 simulated events. After two iterations, these alignment corrections give an improved Cherenkov angle width, σ_C , of 0.64 mrad (from 0.95). Compared with the target resolution of 0.62 mrad the residual misalignment contributes (in quadrature) a 0.16 mrad uncertainty to the total precision, which is small compared to other sources of error (Table 5.1). The same procedure can be applied to any components of the RICH system.

The power of this method to establish the accuracy of the detector simulation is limited by its blindness to misalignments that do not influence $\Delta\theta(\phi)$, i.e. x -axis translations in the case of the RICH 2 photon detector panels. However, since these misalignments do not therefore degrade the RICH resolution, they are irrelevant to RICH alignment.

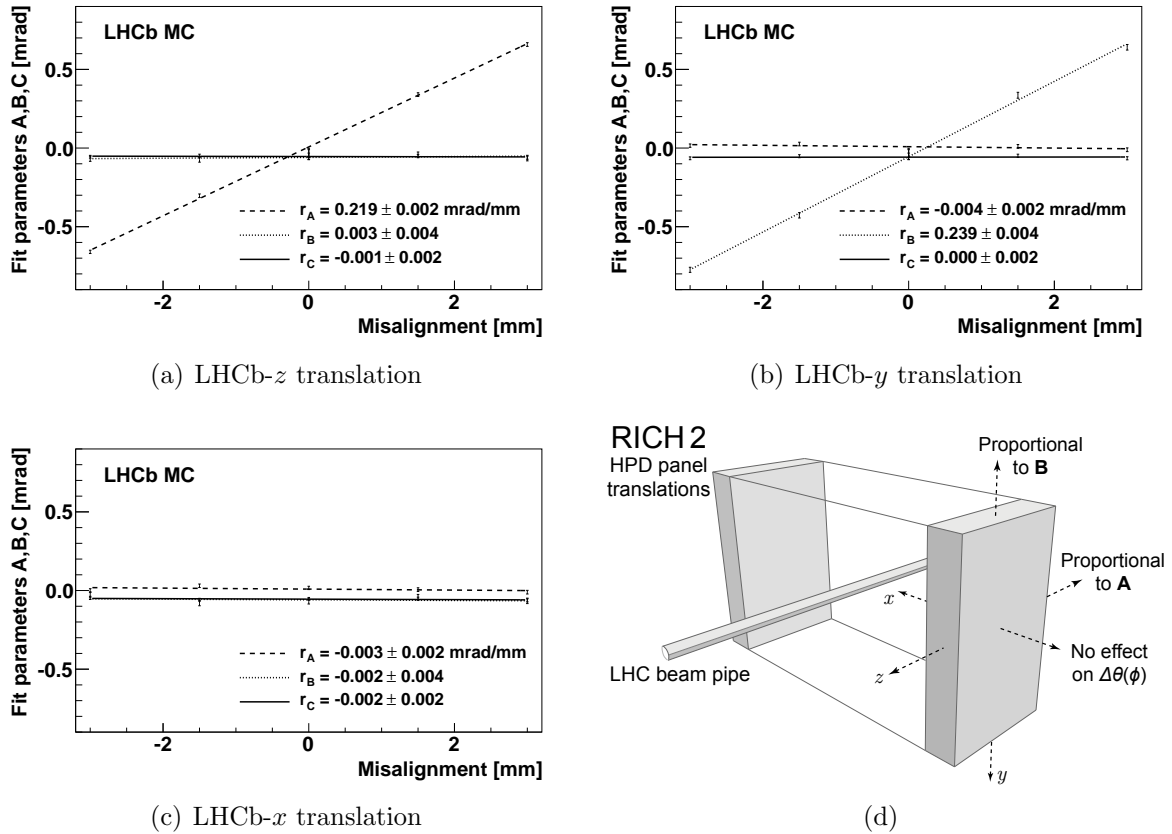


Figure 5.5: Correlated changes are observed in the misalignment amplitudes A and B with simulated translations of RICH 2 HPD photon detector panels along LHCb's z -axis (a) and y -axis (b) respectively. No effect is observed for translations along the x -axis (c). The misalignment directions are illustrated in (d).

5.5 Application to collision data

The first pp collision data was recorded by LHCb on 23 November 2009. The single photon Cherenkov angle resolutions of RICH 1 and RICH 2 were initially measured to be 4.0 & 1.5 mrad respectively. These resolutions were significantly worse than the expected 1.6 & 0.7 mrad (Table 5.1), making plain the need to investigate the alignment of both RICH detectors.

At first sight, the alignment distributions $\Delta\theta(\phi)$ did not reveal the expected sinusoidal deviations associated with misalignment, e.g. Fig. 5.6(a). However, with further investigation, the broad distribution observed was found to be the sum of many independent structures corresponding to misalignments of various optical components. These underlying misalignment distributions can be separated out by selecting only those photons that, by geometry, unambiguously hit a particular set of components, e.g. Fig. 5.6(b) from a single RICH 1 mirror pair.

A complete calibration of the RICH system requires a global minimisation of separate alignment corrections for each combination of spherical mirror, flat mirror and HPD.

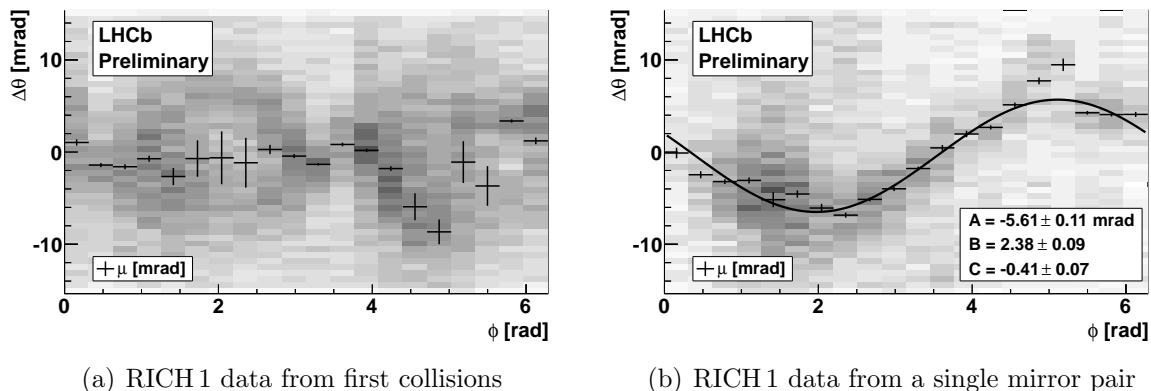


Figure 5.6: Alignment distributions, $\Delta\theta(\phi)$, in RICH 1 from first pp collision data. The broad structure observed in the total data sample (a) is comprised of multiple distributions from different misalignments of various internal components. Taking only photons that, by geometry, unambiguously hit a single pair for mirrors, e.g. (b), reveals one of these underlying distributions.

Reconstructed track-photon pairs can be assigned to a particular combination of RICH components for this analysis. In some cases this assignment is ambiguous due to the assumption in reconstruction that photons are emitted at the mid-point of the track path through a radiator. Only Cherenkov photons that can be unambiguously associated with a spherical and flat mirror pair are used for alignment. In RICH 1, there is additional ambiguity when a track can be paired with photons from both aerogel and C_4F_{10} radiators. For the initial alignment, only the gas radiator is considered as a source for photon reconstruction.

With the limited statistics of the early data-taking period, many combinations of components either do not see enough photons or do not cover a sufficient range in ϕ for the fitting procedure to be performed. In RICH 1, approximately 98% of the C_4F_{10} photons unambiguously hit one of the four flat mirrors closest to the beam in combination with a single spherical mirror. No other flat mirrors see sufficient photons in the available data set to be corrected.

In RICH 2, the larger number of mirrors requires significantly more partitioning of the data such that the smallest data subsets with sufficient ϕ coverage are the two HPD panels. For a first alignment, the four RICH 1 mirror pairs and the two RICH 2 photon detector panels are considered.

For RICH 2, this alignment will therefore represent an average correction for misalignments of all the mirrors (weighted by their occupancy) on each side of the detector and is not expected to reach the target resolution of 0.7 mrad. With the RICH 1 alignment however, a pair of individual optical components is being aligned and better results are expected.

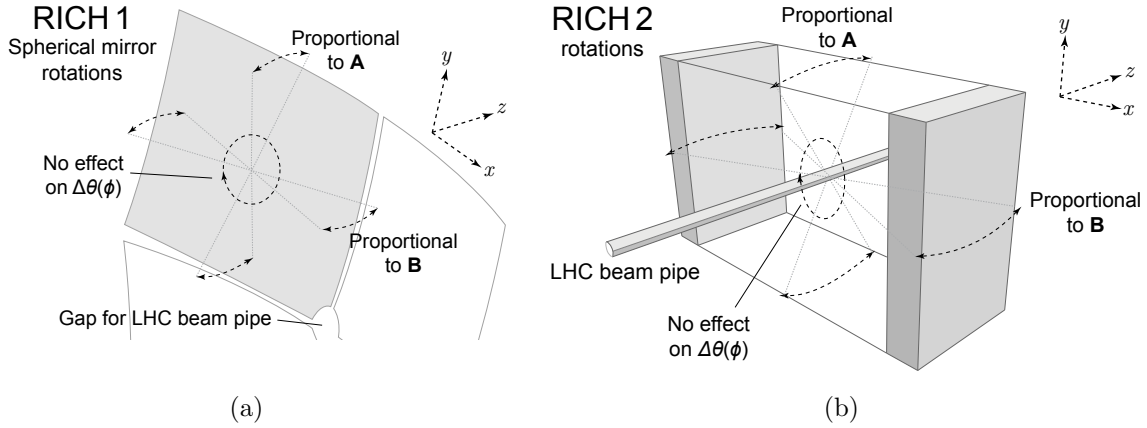


Figure 5.7: Sketches of (a) a RICH 1 spherical mirror and (b) the full RICH 2 apparatus, showing the possible rotational degrees of freedom. Two of these directions are proportional to the amplitudes A and B of the $\Delta\theta(\phi)$ distribution (Eqn. 5.5) and can be measured simultaneously. The third direction has no optical effect.

Table 5.2: Alignment corrections applied to (a) RICH 1 and (b) RICH 2 to improve Cherenkov angle resolution, σ_C , by minimisation of the misalignment amplitudes in the distribution $\Delta\theta$ vs. ϕ (Eqn. 5.5) from early data. Components are labelled as viewed from the interaction point.

(a)			(b)		
RICH 1 corrections	A	B	RICH 2 corrections	A	B
<i>Spherical mirrors</i> [mrad]			<i>Full apparatus</i> [mrad]		
· Left · Up	-1.42	+1.20		-0.69	+1.27
· Down	+1.44	-1.68	<i>HPD panels</i> [mm]		
· Right · Up	-1.67	+2.92	· Left	-3.18	-0.93
· Down	+0.43	-0.75	· Right	+4.04	-0.72

5.5.1 Method

The alignment of the RICH system is detailed in Ref. [1]. Corrections for the four RICH 1 mirror pairs are carried out by adjusting the spherical mirrors. These mirrors have two optically relevant rotational degrees of freedom, illustrated in Fig. 5.7(a). Each of these rotations is correlated to one of the two misalignment amplitudes, A or B . The correlation coefficients, r_A and r_B , are measured in simulation by a similar method to that described in Section 5.4. The alignment of RICH 2 is carried out in two stages: first by rotation of the entire apparatus about two optically relevant degrees of freedom (illustrated in Fig. 5.7(b)) and second, by translational corrections of the two HPD panels, as described in Section 5.4.4.

The alignment corrections are found by iteration of these prescriptions, with reconstructions repeated to optimise the single photon Cherenkov angle precision. The resulting corrections to be applied are given in Table 5.2.

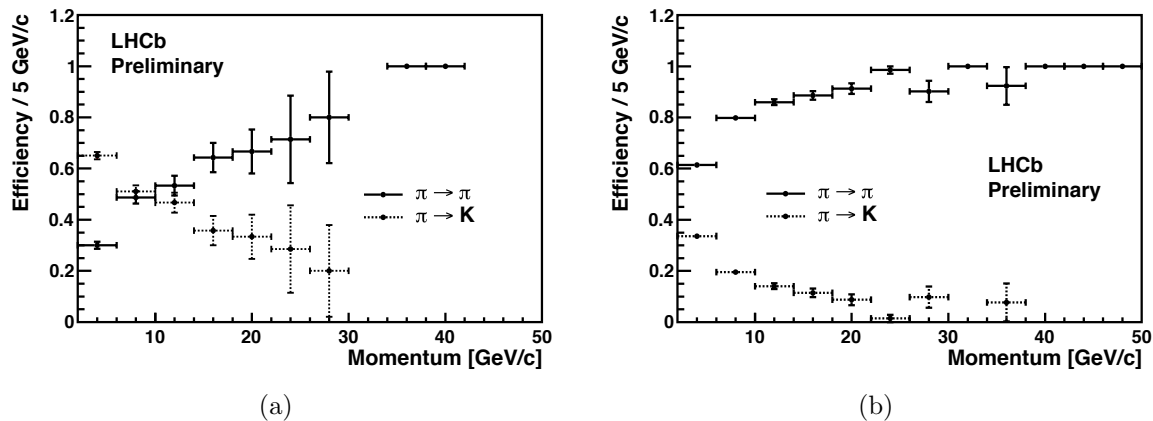


Figure 5.8: Efficiencies for correct pion identification (solid lines) and misidentification as a kaon (dotted lines), for $DLL_{\pi-K} > 0$. These efficiencies are shown (a) before and (b) after alignment of the RICH and tracking systems. Courtesy of A. Powell [private communication].

5.5.2 Results and discussion

The improvements to Cherenkov angle resolution achieved with this method are significant: from 4.0 to 2.2 mrad in RICH 1 and from 1.5 to 0.9 mrad in RICH 2 but remain far from the expected resolutions of 1.6 & 0.7 mrad. These residual differences translate to contributions to the total resolution of 1.6 mrad for RICH 1 and 0.6 mrad for RICH 2, which are significantly larger than other sources of error (Table 5.1).

The corrections applied in Table 5.2, ranging up to rotations of 3 mrad and translations of 4 mm, are larger than anticipated from survey uncertainties. Such large movements are unlikely to be physical and probably represent an average over multiple misalignments of underlying components such as the RICH 2 mirrors and the individual HPDs. More data and further study are required to address the alignment of these additional components.

5.6 PID performance after alignment

The performance of the RICH system is defined by its efficiency in separating between charged particle species, e.g. π or K . A likelihood, e.g. \mathcal{L}_π for a track having been produced by a pion, is constructed by matching the pattern of pixel hits seen in the RICH to that expected knowing the reconstructed track position and momentum. This expectation is calculated from the geometry and resolution of the RICH as well as the Cherenkov angle for the particle velocity (Eqn. 5.1) given by the track momentum and the pion mass hypothesis. A choice between two particle mass hypotheses is then based on the difference in the logarithms of these likelihoods called the ‘‘Delta Log-Likelihood’’, e.g. $DLL_{\pi-K} (\equiv \ln \mathcal{L}_\pi - \ln \mathcal{L}_K) > 0$ to favour pion over kaon [127].

The efficiencies for correct identification, and misidentification, by this method are tested in data using particles of unambiguous type. These particles are identified from

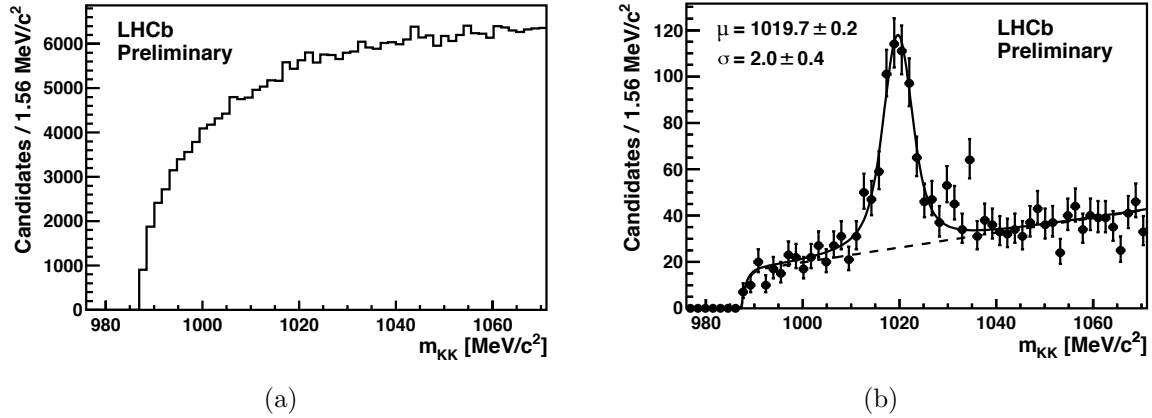


Figure 5.9: Selection of $\phi(1020) \rightarrow K^+K^-$ in 0.9 TeV data with (a) only kinematic information and (b) an additional tight cut on the kaon PID of both daughter tracks of $DLL_{K-\pi} > 15$ to reveal the $\phi(1020)$ mass peak. Courtesy of A. Powell [126].

abundant decays, e.g. pions from $K_S^0 \rightarrow \pi^+\pi^-$, and selected using only kinematic information, i.e. without the use of PID. Efficiencies are shown for pion identification in Fig. 5.8 from data reconstructed (a) before and (b) after the initial alignment of the RICH (described in this Chapter) and of the tracking systems.

A clear illustration of the power of RICH PID is given by selection of the decay $\phi(1020) \rightarrow K^+K^-$ made after the initial alignment. Fig. 5.9 shows a selection attempted with (a) only kinematic information and (b) an additional tight cut on the kaon PID of both daughter tracks, $DLL_{K-\pi} > 15$. The $\phi(1020)$ mass peak is revealed from the previously overwhelming combinatorial background.

5.7 Further investigations and outlook

Most tracks in RICH 1 are reconstructed with small angles to the beam pipe such that the vast majority of Cherenkov photons hit a relatively small number of HPDs in the central region (Fig. 5.10). As introduced in Section 5.5, the four aligned pairs of spherical and inner flat mirrors see more than 98 % of all photons. For each of these mirror pairs, about a third of photons unambiguously hit just one HPD and five photon detectors see 90 % (Fig. 5.11). The RICH 1 alignment corrections are therefore highly dependent on a few photon detectors, each of which could also be misaligned, e.g. by an offset of the pixel chip or by magnetic field effects (Section 4.2.5).

The C_4F_{10} Cherenkov rings have a larger radius than the HPDs themselves, such that individual photon detectors see only a part of the $\Delta\theta(\phi)$ distribution and cannot be aligned by the method presented in this Chapter. The ϕ coverage for one aligned mirror pair is shown per HPD in Fig. 5.12(a). Relative misalignments between HPDs can however be checked by comparison of their mean Cherenkov angle in regions of ϕ where there is

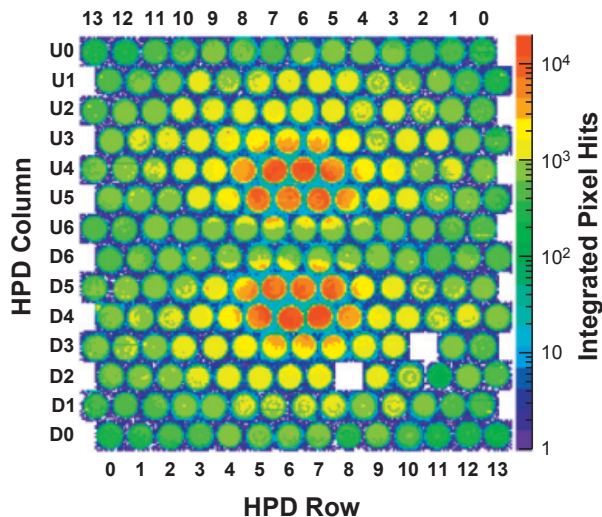


Figure 5.10: Time-integrated pixel hits in RICH 1. The HPDs are arranged in rows and columns. Empty regions indicate where photon detectors have been disabled. Courtesy of R. Young [128].

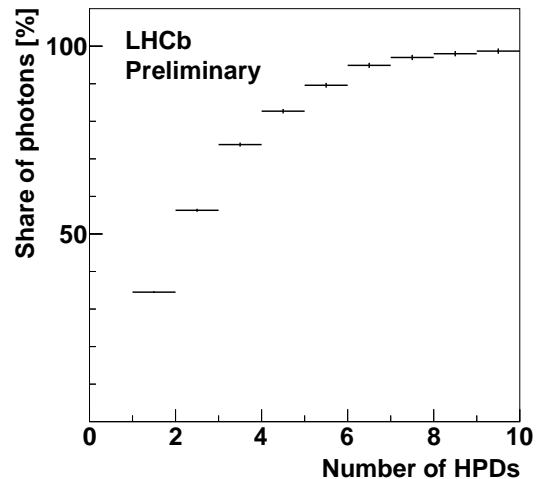


Figure 5.11: The cumulative share of Cherenkov photons seen by the busiest HPDs after hitting one of the four aligned RICH 1 mirror pairs. The top five photon detectors see 90% of these photons, with a third seen by just one HPD.

Table 5.3: The mean, μ , and width, σ , from fits (as described in Section 5.4.3) to the $\Delta\theta$ distribution for photons reflected from a single aligned mirror pair in RICH 1. Fit results from all photons are compared with subsets from three HPDs. Large μ indicate HPD misalignments. As a result, Cherenkov angle resolutions are significantly better for individual photon detectors than for all photons combined.

[mrad]	All HPDs	U4, 5	U5, 5	U5, 6
μ	+0.35	-2.73	+3.56	-0.42
σ	3.69	1.68	2.27	1.90

overlapping coverage, e.g. Fig. 5.12(b). The observed shifts in mean from zero indicate significant HPD misalignments. These offset distributions for each HPD combine to give a much broader overall $\Delta\theta$ distribution and provide a clear illustration of the source of the degradation in Cherenkov angle resolution, σ_C , observed in data.

The fitted values of μ and σ are compared in Table 5.3 for each of the HPDs shown in Fig. 5.12(b) as well as for the combination of all photons from the same mirror pair. The resolutions of individual HPDs are significantly better than for the combined data. With a future alignment of each photon detector, there is therefore confidence that the RICH 1 resolution will move significantly closer to the C_4F_{10} target of 1.5 mrad given in Table 5.1 (see Section 5.8 for the latest results).

Since the individual photon detectors appear to be misaligned for a single RICH 1 mirror pair, the alignment corrections applied to those mirrors do not describe true movements of the mirrors but must describe a photon-weighted average of the mirrors and

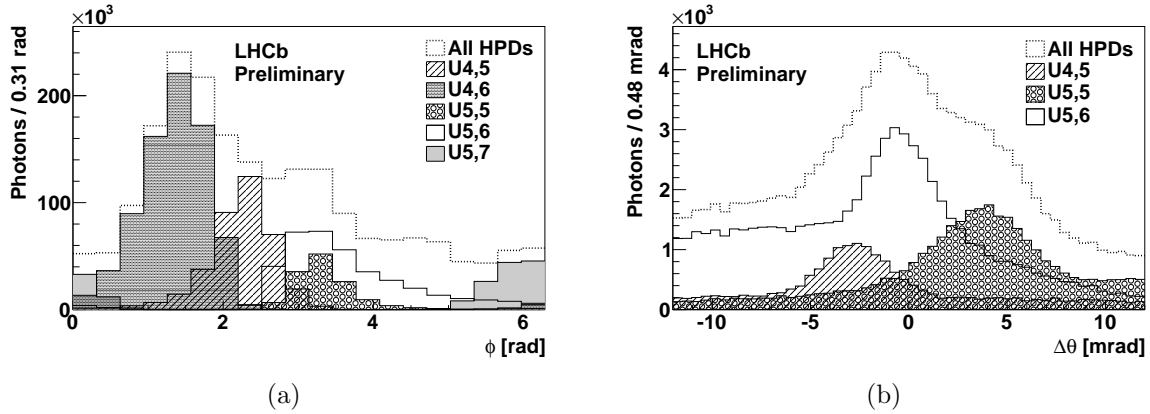


Figure 5.12: (a) The coverage in ring angle, ϕ , of individual HPDs seeing photons reflected by a single aligned RICH 1 mirror pair. (b) Comparison of the $\Delta\theta$ distributions for three HPDs in a region with overlapping ϕ coverage (bin 10 of 20 in (a), or $2.8 < \phi < 3.1$) showing evidence for HPD misalignments.

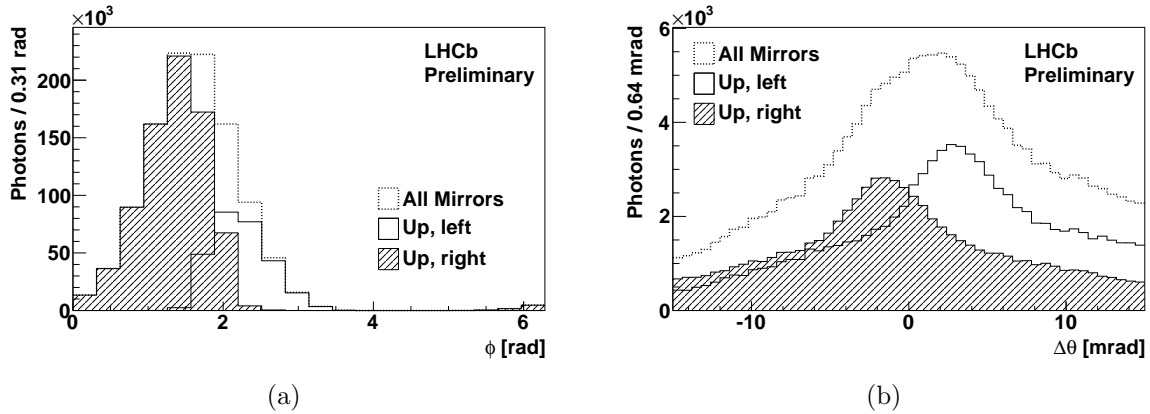


Figure 5.13: (a) The coverage in ring angle, ϕ , of a single HPD (U4, 6) seeing photons reflected by two aligned RICH 1 mirror pairs. (b) Differing mean $\Delta\theta$ values for the same HPD in combination with each mirror pair are seen in a region with overlapping ϕ coverage (bin 7 of 20 in (a), or $1.9 < \phi < 2.2$), indicating that the applied mirror corrections are wrong.

HPDs. This fact can be shown explicitly if a single HPD can be found that sees light (in an overlapping region of ϕ) from two different mirror pairs. One such HPD is shown in Fig. 5.13. The significant offset in mean of the $\Delta\theta$ peak from this single device when observing light from two mirror pairs shows that the applied mirror corrections are wrong. A separate alignment for each HPD is required before the true mirror positions can be measured.

Two additional systems exist to align the photon detectors: the Magnetic Distortion Calibration System (MDCS), which is permanently mounted inside RICH 1, and the one-off “beamer” measurements carried out for RICH 2 [129,130]. Both methods were designed to measure the effect of the LHCb magnetic field on the HPDs, introduced in Section 4.2.5. Although the HPDs are magnetically shielded, any residual field may perturb the trajectories of photoelectrons inside the vacuum tube. The effect is observed as a movement

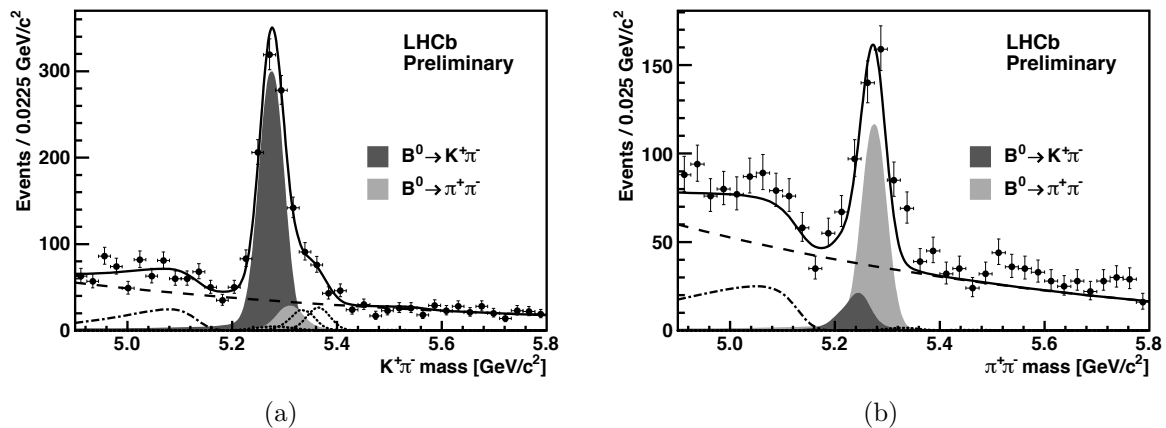


Figure 5.14: (a) Selection of the decay $B^0 \rightarrow K^+\pi^-$ with the PID cut $\text{DLL}_{\pi-K} > 0$ for a measurement of direct CP violation [131]. The data is described by a fit including the signal peak (dark gray) and a background (solid curve) comprised of combinatorics (dashed curve), three-body decays (dashed-dotted curve) & the mass peaks of kinematically similar decays: $B^0 \rightarrow \pi^+\pi^-$ (light gray), etc. (dotted curves). Each decay is selected using RICH PID information, e.g. (b) $B^0 \rightarrow \pi^+\pi^-$ with $\text{DLL}_{\pi-K} < -3$, in order to describe the overall $K^+\pi^-$ invariant mass distribution.

of the image centre on a pixel chip and is measured by comparison of the image centre position with and without the magnetic field applied. These alignment systems therefore also test for inaccurate pixel chip positions in the detector simulation.

Alignment of the RICH 2 mirrors, as well as the RICH 1 outer mirrors, requires more data than was available in early running. A selection procedure has since been developed within the collaboration to provide data sets enriched with photons from the less populated mirrors as well as a minimisation scheme to simultaneously align all mirrors.

5.8 Latest performance

At the time of writing, the latest mirror alignment and HPD magnetic field corrections give Cherenkov angle resolutions of 1.75 mrad for C_4F_{10} and 0.73 for CF_4 . The residual differences between data measurements and MC expectations translate to a contribution from misalignment towards the total resolution of 0.9 mrad for the RICH 1 gas and 0.2 mrad for RICH 2. In other words, the uncertainty due to misalignment is now of a similar magnitude to other sources (Table 5.1).

Particle Identification information from the RICH system is now being used as an effective discriminant in a number of LHCb analyses, such as measurement of direct CP violation in the decay $B^0 \rightarrow K^+\pi^-$ [131]. A kinematic selection of the signal decay for that analysis retains peaking backgrounds due to misidentified final state particles from decays such as $B^0 \rightarrow \pi^+\pi^-$ (see Fig. 5.14). Separation of each decay using DLL criteria allows an accurate description of the overall $K^+\pi^-$ invariant mass distribution.

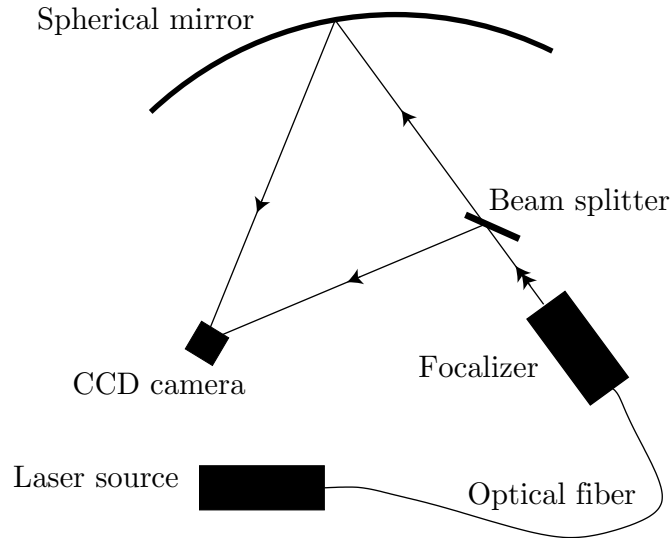


Figure 5.15: Schematic of the Laser Alignment Monitoring System (LAMS) [84].

5.9 Alignment monitoring

With the continuing progress to optimise RICH performance over the first year of data taking, the alignment of the optical components has been regularly checked. In the future this procedure will become more automated. There are already two continually running systems to monitor the alignment around the clock.

The first system employs the same alignment method described in this Chapter. The fitting procedure for the $\Delta\theta(\phi)$ distribution has been integrated into a general online monitoring framework and run approximately every 15 minutes on a small subset of the data that is reconstructed on a dedicated cluster. The evolution of the alignment amplitudes A and B are followed separately for each of the four detector panels and if either parameter were to grow to 1 mrad an alarm would be raised to notify the shift crew that some optical component has moved.

The second, and complementary, tool is the Laser Alignment Monitoring System (LAMS), installed inside both RICH detectors to monitor the mechanical stability of the mirrors. All four spherical mirrors in RICH1 are monitored as well as eight flat and eight spherical mirrors in RICH2. There exists a separate system for each mirror consisting of a laser source, beam splitter and a CCD camera that sees both the beam coming directly from the laser source and the beam reflected off the mirror, as shown in Fig. 5.15. Any relative movement between the two spots would indicate a mirror misalignment. A control system was developed using PVSSII, a Supervisory Control and Data Acquisition (SCADA) framework, to facilitate manual measurement of these spot positions and to automate the process for regular updates. This system is described in Appendix A.

5.10 Cherenkov photon yield

A useful measurement of RICH performance is the number of signal Cherenkov photons observed per track from each of the radiators. The Cherenkov photon yield expected from a charged particle passing through a radiator is predicted by Frank-Tamm theory and can be written from Eqn. 5.2 as:

$$N_\gamma = \frac{2\pi L}{c} \alpha Z^2 \int_{\beta > 1/n(\nu)} \left[1 - \frac{1}{\beta^2 n(\nu)^2} \right] d\nu . \quad (5.6)$$

for particles with velocity, β , over the Cherenkov threshold.

Monte Carlo simulations of the LHCb RICH system during the design phase predicted typical photon yields for particles with $Z = 1$ and $\beta \approx 1$ of approximately 6.5, 30 and 22 from aerogel, C_4F_{10} and CF_4 respectively, taking the detector geometry into account as well as the wavelength dependence of the refractive index and HPD response [84].

A novel method has been developed to measure this yield in data, which makes use of software employed for RICH alignment. As introduced in Section 5.2, the algorithm used in data reconstruction to match RICH photons and tracks attempts to pair each HPD hit with all tracks that pass through the relevant radiator. Candidate photon-track pairs are kept if their Cherenkov angle (found by assuming the photon was emitted at the mid-point of the track's path through the radiator) falls within a specified window in $\Delta\theta$. Individual HPD hits may be assigned to multiple tracks and, in the high track multiplicity environment of LHCb, this procedure results in a large background component to the number of photons assigned to a typical track. The new method makes use of a fit to the $\Delta\theta$ distribution to estimate the signal component of this assigned number.

The $\Delta\theta$ distribution is fitted with a Gaussian signal function, $S(\Delta\theta)$, over a 2nd order polynomial background, $B(\Delta\theta)$, as shown in Fig. 5.16(a), following the approach of the alignment procedure described in Section 5.4.3. These fitted distributions are used to calculate a signal weight for every photon as a function of the reconstructed Cherenkov angle, $W(\Delta\theta_\gamma)$. The estimated signal photon yield, N_{signal} , is found for a given track by the sum of these weights, found for all photons associated with that track during reconstruction, by the formula:

$$N_{\text{signal}} = \sum_{\gamma} W(\Delta\theta_\gamma) = \sum_{\gamma} \frac{S(\Delta\theta_\gamma)}{S(\Delta\theta_\gamma) + B(\Delta\theta_\gamma)} . \quad (5.7)$$

The initial results found from data taken during the 2009 pilot run of the LHC are given in Table 5.4. The yields estimated from each of the RICH radiators are significantly reduced compared to those found from MC simulation with contemporary reconstruction. The method however, provided a good approximation, applied to the simulated data set, of the MC true Cherenkov photon yield. N.B. this contemporary simulated yield was

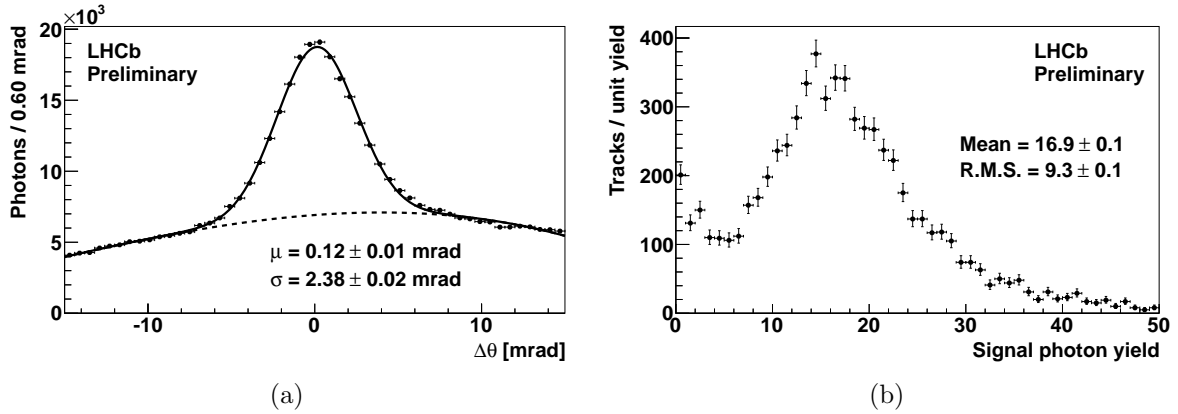


Figure 5.16: The Cherenkov photon yield is estimated by Eqn. 5.7 with a weight function found from a fit to the $\Delta\theta$ distribution (a) with a Gaussian signal component over a 2nd order polynomial background. The distribution of tracks by estimated Cherenkov photon yield (b) is found for tracks with momentum above 5 GeV/c from the C₄F₁₀ radiator in RICH 1 in 2009 data with a mean of about 17.

Table 5.4: The mean Cherenkov photon yield per track is found from 2009 data and contemporary reconstructed MC events by Eqn. 5.7. Estimations using this method are similar to MC truth. The mean estimated from data is significantly lower than from simulation for all radiators.

Radiator	Aerogel	C ₄ F ₁₀	CF ₄
Track p_T [GeV/c]	> 1	> 5	> 15
Data est.	3.8 ± 0.1	16.9 ± 0.1	10.0 ± 0.1
MC est.	5.8 ± 0.1	19.0 ± 0.1	11.2 ± 0.1
MC truth	6.1 ± 0.1	19.5 ± 0.2	11.8 ± 0.1

found to be significantly reduced compared to the design expectations quoted above for reasons not fully understood.

In the higher instantaneous luminosity running conditions of early 2010, a further reduction in yield was observed and related to the increased detector occupancy. An approximately linear correlation was observed of a 1% reduction in mean estimated yield for each additional track reconstructed in the RICH.

In late 2010, this project was handed over to a new PhD student at Imperial College, Indrek Sepp, for further development.

Chapter 6

V^0 production ratios

“Most of what we know about the universe we know thanks to a lot of guys (and ladies) who stayed up late at night.”

– Leon Lederman, 1993 [132]

6.1 An introduction to “ V ” decays

As outlined in Chapter 2, the discoveries of the surprisingly long-lived V^0 (now called the K^0) meson, by Rochester and Butler in 1947 [39] (as well as the neutral Λ baryon, by Anderson in 1950 [133]), lead to the proposal of a new quantum number: “strangeness” (S), and ultimately to Gell-Mann’s quark model [42].

These particles were named after the characteristic “ V ”-shaped track signatures of their dominant decays: $K^0 \rightarrow \pi^+\pi^-$ and $\Lambda \rightarrow p\pi^-$ (see Fig. 6.1) and are now known collectively as V^0 hadrons. The long lifetimes of these strange particles was explained by Pais with the concept of “associated production”, i.e. conservation of strangeness, in strong interactions [134]. The V^0 particles are created in pairs with no net strangeness via the strong force but cannot decay by the same force without breaking the new conservation law. Pais noted that “very weak couplings have so far only been considered in neutrino processes” and suggested that strangeness might not be conserved in weak interactions and that this force could therefore be responsible for the slow V^0 decays.

A third V^0 particle, the antimatter equivalent of the Λ baryon, was observed from the decay $\bar{\Lambda} \rightarrow \bar{p}\pi^+$ at the Bevatron in 1958, soon after the discoveries there of the antiproton and the antineutron [135–137]. The question of an antimatter equivalent of the K^0 turned out to be more complex and has had a profound influence on the development of the Standard Model.

Before the discovery of the K^0 , the only known neutral meson was the π^0 , which is understood to be its own antiparticle. The quark picture of the neutral kaon, however, suggested the existence of a distinct antimatter partner, the \bar{K}^0 . Despite the different

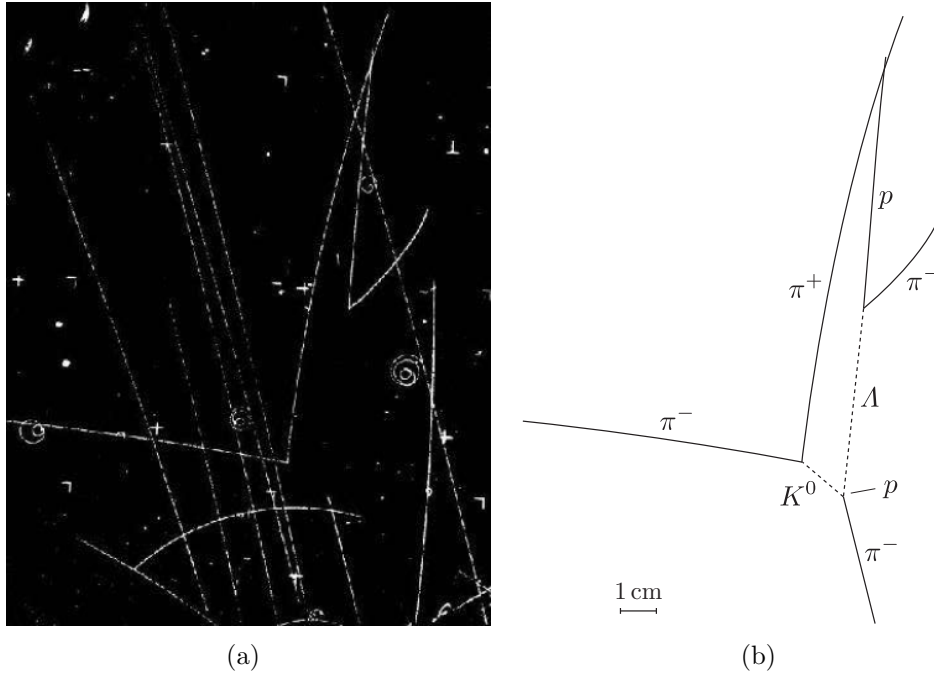


Figure 6.1: (a) Photograph showing the associated production of Λ ($S=+1$) and K^0 ($S=-1$) strange hadrons from the collision between a high energy π^- from the Berkeley Bevatron and a nuclear proton in a liquid hydrogen bubble chamber. Credit Lawrence Berkeley Laboratory. (b) A trace highlights the incident pion, the assumed paths of the neutral V^0 particles and the products of their decays: $K_S^0 \rightarrow \pi^+\pi^-$ and $\Lambda \rightarrow p\pi^-$.

quark content, however, the weak decays of both K^0 and \bar{K}^0 result in exactly the same hadronic final states:

$$K^0 \left\{ \begin{array}{l} d \\ \bar{s} \end{array} \right\} \left\{ \begin{array}{l} d \\ \bar{u} \end{array} \right\} \pi^- \quad \text{and} \quad \bar{K}^0 \left\{ \begin{array}{l} s \\ \bar{d} \end{array} \right\} \left\{ \begin{array}{l} d \\ \bar{u} \end{array} \right\} \pi^- \quad (6.1)$$

W^+ $\left\{ \begin{array}{l} u \\ \bar{d} \end{array} \right\} \pi^+$

which proceed at the same rate and are therefore experimentally indistinguishable from each other.

These equivalent final states lead Gell-Mann and Pais to make a surprising and highly original proposal: that the shared $\pi^+\pi^-$ state could act as a bridge allowing spontaneous transition between K^0 and \bar{K}^0 . Neutral kaons could therefore oscillate between particle and antiparticle states as they travel [138]. This oscillation proceeds via a second order weak process, which can be illustrated by a Feynman “box” diagram, e.g.

$$\begin{array}{ccc}
 s & \xrightarrow{u} & d \\
 \bar{K}^0 & \begin{array}{c} \downarrow W^- \\ \uparrow W^+ \end{array} & K^0 \\
 \bar{d} & \xrightarrow{\bar{u}} & \bar{s}
 \end{array} \quad (6.2)$$

and so the neutral kaons measured in an experiment are really some combination of the states K^0 and \bar{K}^0 .

Gell-Mann and Pais reasoned that the proper combinations of K^0 and \bar{K}^0 should be eigenstates of the charge conjugate operator \hat{C} , which was understood to define a symmetry between particles and antiparticles, i.e. $\hat{C}|e^- \rangle = |e^+ \rangle$ and $\hat{C}|\gamma \rangle = |\gamma \rangle$. Soon after their proposal however, it was discovered that C symmetry, as well as parity, was violated in weak interactions and the combined operator \hat{CP} was suggested to represent the correct symmetry between particles and antiparticles, i.e. $\hat{CP}|e_L^- \rangle = |e_R^+ \rangle$ [25, 26, 139, 140]. The proposed neutral kaon particle/antiparticle CP eigenstates became [4]:

$$|K_1^0 \rangle = \frac{1}{\sqrt{2}} (|K^0 \rangle - |\bar{K}^0 \rangle) \quad \text{and} \quad |K_2^0 \rangle = \frac{1}{\sqrt{2}} (|K^0 \rangle + |\bar{K}^0 \rangle) \quad (6.3)$$

with $CP(K_1^0) = +1$ and $CP(K_2^0) = -1$.

These new states could be differentiated in an experiment by their CP -conserving decays $K_1^0 \rightarrow 2\pi$ and $K_2^0 \rightarrow 3\pi$ ¹. The decay rate of the K_1^0 is significantly faster than of the K_2^0 since the mass difference is greater. Therefore, while a K^0 beam, for example, would start out as a mixture of K_1^0 and K_2^0 , over time the K_1^0 component would decay away, leaving a pure K_2^0 beam.

The conservation of CP symmetry therefore predicted that, at a large distance from a K^0 beam source, only decays to 3π should be observed. In 1964, Cronin and Fitch set out to test this prediction and, by observing a small number of downstream decays to 2π , they showed that CP symmetry is broken in weak interactions [27]. The true weak eigenstates had to be rewritten as:

$$|K_S^0 \rangle = \frac{1}{\sqrt{1 + |\epsilon|^2}} (|K_1^0 \rangle - \epsilon |K_2^0 \rangle) \quad \text{and} \quad |K_L^0 \rangle = \frac{1}{\sqrt{1 + |\epsilon|^2}} (|K_2^0 \rangle + \epsilon |K_1^0 \rangle) \quad (6.4)$$

where ϵ is small ($\sim 2 \times 10^{-3}$ [27]). These states are named “K-Short” and “K-Long” for their relative lifetimes, which are dominated by the decay rates of their respective majority component CP states, i.e. the K_S^0 typically decays like K_1^0 , fast to 2π .

While it is these K_S^0 and K_L^0 weak eigenstates that define the spontaneous decay rates of neutral kaons, their strong (production) eigenstates K^0 and \bar{K}^0 have a role in the development of a neutral kaon beam when it passes through material. The \bar{K}^0 interact more readily with nuclei than do K^0 , resulting in a higher absorption rate that changes the relative fractions of these states in the beam and by Eqns. 6.3 and 6.4 also changes the fractions of K_S^0 and K_L^0 . As first observed at Berkeley in 1961, the K_S^0 component of a kaon beam, which had decayed away far from the beam source, is partially regenerated on passing through a metal plate [141]. This regeneration, effectively turning K_L^0 into K_S^0 , occurs in particle detectors and must be taken into account when estimating the rate of

¹ $CP(2\pi) = C(2\pi) \times P(2\pi) = +1 \times (-1)^2 = +1$ and $CP(3\pi) = C(3\pi) \times P(3\pi) = +1 \times (-1)^3 = -1$.

neutral kaon production from K_S^0 decays.

The kaon V^0 decay photographed in Fig. 6.1(a) is now understood to be $K_S^0 \rightarrow \pi^+\pi^-$ and it is this same decay that shall be considered along with the Λ and $\bar{\Lambda}$ baryon V^0 decays in the remainder of this chapter.

6.2 Strangeness production ratios

As introduced in Chapter 3, the application of the Standard Model (SM) Lagrangian to low energy (“soft”) QCD interactions is problematic in practice due to the large coupling, α_S . The soft QCD regime describes quark confinement and is important for understanding the parton momentum distributions inside colliding protons as well as the hadronisation of quarks and gluons to produce the mesons and baryons observed in experiments.

Without full calculations for such processes, Monte Carlo generators have been devised employing phenomenological models (such as PYTHIA’s Lund string fragmentation, described in Section 3.2.3) that are optimised, or “tuned”, to accurately reproduce experimental observations. These generators predict how SM physics will behave at the LHC and constitute the reference for the observation of New Physics effects. This reference must therefore be validated with new measurements from the LHC experiments as an essential first step towards future discoveries.

Strange quark production is a powerful probe for hadronisation processes at pp colliders since protons have no net strangeness and the s quark mass is small enough to be produced during hadronisation (see Section 3.2.3). Recent experimental results in the area have been published by STAR from RHIC pp collisions at $\sqrt{s} = 0.2$ TeV and by ALICE, CMS and LHCb from LHC pp collisions at $\sqrt{s} = 0.9$ and 7 TeV [142–145]. LHCb can make an important contribution thanks to a full instrumentation of the detector in the forward region that is unique among the LHC experiments. The opportunity to carry out studies on data recorded at different energies with the same apparatus helps to control the experimental systematic uncertainties.

Limitation of uncertainties is a motivating factor for the choice to measure production ratios since, during the early running period of the LHC, the systematic uncertainty on luminosity was about 10%. As well as removing this uncertainty, the measurement of ratios at LHCb will also reduce the impact of potential detector effects due to the preliminary status of calibration.

In this chapter I present LHCb’s published measurements of the efficiency corrected production ratios of the strange particles $\bar{\Lambda}$, Λ and K_S^0 as observables related to the fundamental processes behind parton fragmentation and hadronisation [3]. The ratios

$$\frac{\bar{\Lambda}}{\Lambda} = \frac{\sigma(pp \rightarrow \bar{\Lambda}X)}{\sigma(pp \rightarrow \Lambda X)} \quad \text{and} \quad \frac{\bar{\Lambda}}{K_S^0} = \frac{\sigma(pp \rightarrow \bar{\Lambda}X)}{\sigma(pp \rightarrow K_S^0 X)} \quad (6.5)$$

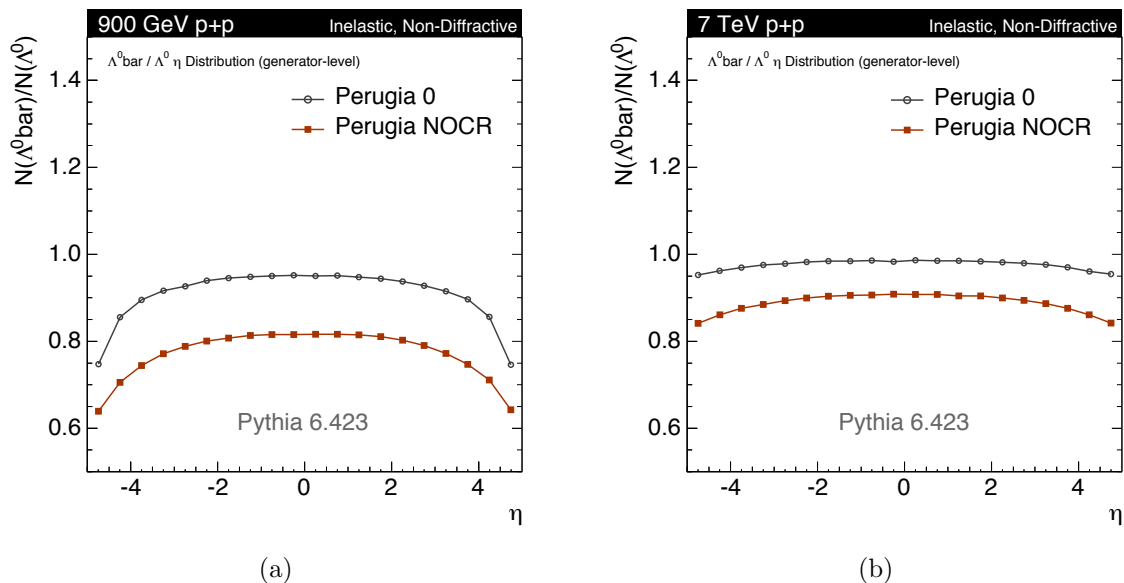


Figure 6.2: Predictions using PYTHIA 6 for the Inelastic Non-Diffractive (IND) production ratio $\bar{\Lambda}/\Lambda$ in (a) $\sqrt{s} = 0.9$ TeV and (b) $\sqrt{s} = 7$ TeV pp collisions at the LHC as a function of pseudorapidity, η . The standard tune Perugia 0 (circles) is compared to an extreme model Perugia NOCR (squares), with no colour reconnections [147].

have predicted dependences on pseudorapidity, η , (or rapidity, y)² and transverse momentum, p_T , that can vary strongly between different generator tunes, as shown in Fig. 6.2, where the example tunes given are [146]:

Perugia 0: Regarded as the standard PYTHIA 6 [71] configuration, this tune provides accurate reproduction of experimental results from SPS, LEP and the Tevatron. In particular, near perfect agreement is reported with the Drell-Yan ($q\bar{q} \rightarrow Z^0/\gamma^* \rightarrow l^+l^-$, discussed in Section 3.1) transverse momentum spectrum measured by CDF at the Tevatron. This tune is therefore considered to provide an excellent description of proton PDFs, ISR and hard scattering processes.

Perugia NOCR: An extreme PYTHIA 6 configuration, this tune is based on Perugia 0. The name stands for “no colour reconnection”, and the most significant change for this tune is the complete suppression of Lund fragmentation string connections between ISR/FSR partons and the beam remnants.³ This configuration predicts a significantly reduced ratio $\bar{\Lambda}/\Lambda$, as shown in Fig. 6.2, and is therefore considered to provide an interesting comparison for LHCb’s results.

Measurements of the ratio $\bar{\Lambda}/\Lambda$ allow the study of the transport of baryon number from pp collisions to final state hadrons. This ratio probes the changing regime from soft proton

²Pseudorapidity $\eta = -\frac{1}{2} \left[\tan\left(\frac{\theta}{2}\right) \right] \equiv \frac{1}{2} \ln\left(\frac{|p|+p_L}{|p|-p_L}\right)$ and rapidity $y = \frac{1}{2} \ln\left(\frac{E+p_L}{E-p_L}\right)$.

³The colour reconnection strength parameter PARP(78) is reduced from 0.33 in Perugia 0 to zero in Perugia NOCR.

excitations at small angles to the beam, where Λ production is expected to dominate, to hard parton showers at larger angles, where Λ and $\bar{\Lambda}$ can be produced at similar rates.

Both baryon and meson in the ratio $\bar{\Lambda}/K_S^0$ contain antiquarks that must be created in the collision from the proton sea quarks, parton showers and/or in hadronisation. This ratio is therefore a direct measurement of the baryon-to-meson suppression factor in hadronisation.

6.3 An overview of LHCb’s tracking system

The Large Hadron Collider Beauty experiment (LHCb) at CERN, introduced in Chapter 4.2, is a single arm spectrometer covering the forward rapidity region. The analysis presented in this chapter relies exclusively on the tracking detectors. The high precision tracking system begins with a silicon strip Vertex Locator (VELO), designed to identify displaced secondary vertices up to about 65 cm downstream of the nominal interaction point. A large area silicon tracker follows upstream of a dipole magnet. Tracker stations, built with a combination of straw tube and silicon strip detectors, are located downstream. The magnet has a reversible field, with the two polarity configurations called “up” and “down”. The tracking system is described in full in Section 4.2.4.

6.4 Data samples

LHCb began recording data on 23 November 2009, when the LHC first collided two proton beams at injection energy, corresponding to a centre-of-mass energy $\sqrt{s} = 0.9$ TeV. These injection energy runs represented a rare opportunity to study scaling violation in soft QCD at the LHC, a collider designed to push the energy frontier, which has been running predominantly at a collision energy of $\sqrt{s} = 7$ TeV since 30 March 2010.

A loose minimum bias trigger was employed during this early running period in which the data used for this analysis was taken, as outlined in Section 4.2.8. The L0 hardware trigger was in pass-through mode with the software High Level Trigger requiring at least one reconstructed track segment in the downstream tracking stations. The trigger is more than 99% efficient for offline selected events that contain at least two tracks reconstructed through the full spectrometer.

Complementary data sets were recorded at two collision energies: $\sqrt{s} = 0.9$ and 7 TeV, with both polarities of the dipole magnet. An integrated luminosity of 0.3 nb^{-1} (corresponding to 12.5 million triggers) was taken at the lower energy on 2-3 May 2010, of which 48% had the up magnetic field configuration. At the higher energy, 67% of a total 1.8 nb^{-1} (110.3 million triggers recorded on 8, 10 & 14 May 2010) was taken with field up.

At injection energy ($\sqrt{s} = 0.9 \text{ TeV}$), the proton beams are significantly broadened spatially compared to the accelerated beams at $\sqrt{s} = 7 \text{ TeV}$. To protect the detector, the two halves of the VELO are retracted along the x -axis from their nominal position of inner radius 8 mm to the beam, out to 18 mm. This configuration results in a reduction of the detector acceptance at small angles to the beam axis by approximately 0.5 units of rapidity.

The beams collide with a crossing angle in the horizontal plane tuned to compensate for LHCb's magnetic field. The angle required varies with beam configuration and for the data-taking period covered by this study was set to 2.1 mrad at $\sqrt{s} = 0.9 \text{ TeV}$ and 270 μrad at 7 TeV. Throughout this analysis V^0 momenta and derived quantities such as rapidity are computed in the centre-of-mass frame of the colliding protons.

6.5 Monte Carlo generation

Samples of Monte Carlo (MC) simulated events have been produced in close approximation to the data-taking conditions described in Section 6.4 for estimation of efficiencies and systematic uncertainties. A total of 73 million simulated minimum bias events were used for this analysis per magnet polarity at $\sqrt{s} = 0.9 \text{ TeV}$ and 60 (69) million events at 7 TeV for field up (down). The LHCb framework for Monte Carlo event generation is introduced in Section 4.2.9 and is based on pp collisions generated by PYTHIA 6. The $\bar{\Lambda}$, Λ and K_S^0 created in these collisions decay via EVTGEN [106]. Interactions between the resulting particles and the detector are modelled by GEANT 4 [108], including the K_S^0 regeneration introduced in Section 6.1. Secondary V^0 produced in material interactions decay via GEANT 4.

Additional samples of five million minimum bias events were generated for studies of systematic uncertainties using PYTHIA 8, with both hard and soft diffraction included⁴ [148, 149]. Similar sized samples were generated with the alternative PYTHIA 6 tunes, Perugia0 and Perugia NOCR.

6.6 Analysis procedure

6.6.1 Reconstruction and quality cuts

As introduced in Section 6.1, V^0 hadrons are named after the “V”-shaped track signature of their dominant decays: $\Lambda \rightarrow p\pi^-$, $\bar{\Lambda} \rightarrow \bar{p}\pi^+$ and $K_S^0 \rightarrow \pi^+\pi^-$, which are reconstructed for this analysis. Given the preliminary status of detector calibration in May 2010, and for the best available momentum resolution, only tracks reconstructed through the full

⁴Single- and double-diffractive process types are considered.

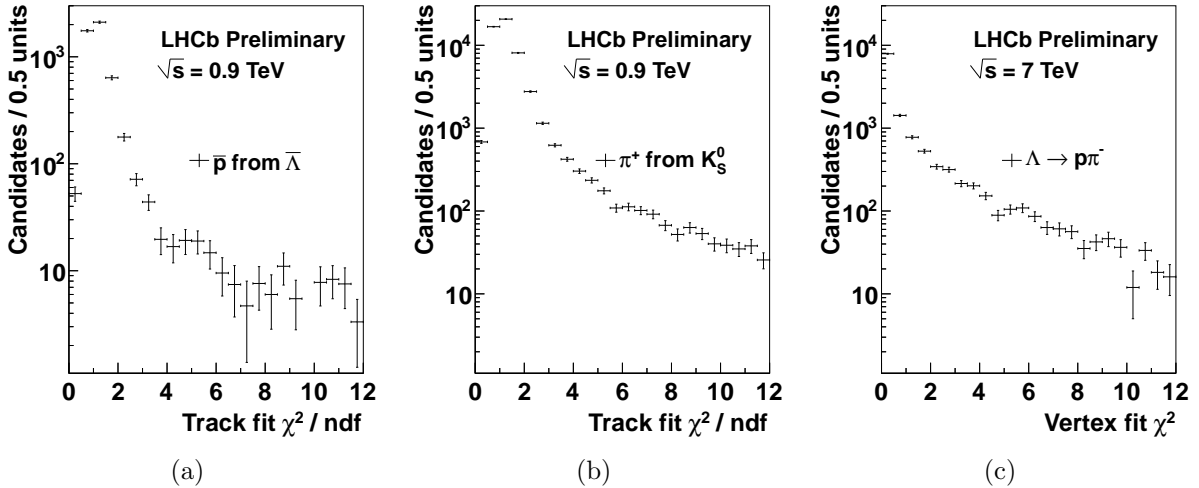


Figure 6.3: Fit quality distributions for (a) \bar{p} tracks used to reconstruct $\bar{\Lambda}$, (b) π^+ tracks from K_S^0 and (c) $\Lambda \rightarrow p\pi^-$ decay vertices. Distributions are estimated for signal V^0 by mass fit weighting. Loose quality criteria retain only candidates with $\chi^2(\text{/ndf}) < 9$.

spectrometer (or “Long” tracks, see Section 4.2.4) are considered, i.e. counting only V^0 that decay within the VELO.

Loose quality criteria are applied to reject poorly reconstructed tracks, considering only those with $\chi^2/\text{ndf} < 9$, e.g. Figs. 6.3(a) and 6.3(b). Any oppositely charged track pair is kept as a potential V^0 candidate if it forms a vertex with $\chi^2 < 9$ (with one degree of freedom for a V^0 vertex), e.g. Fig. 6.3(c).

$\bar{\Lambda}$, Λ and K_S^0 candidates are required to have invariant masses within $\pm 50 \text{ MeV}/c^2$ of their respective PDG values [63]. This mass window is large compared to the measured mass resolutions of about $2 \text{ MeV}/c^2$ for Λ ($\bar{\Lambda}$) and $5 \text{ MeV}/c^2$ for K_S^0 .

6.6.2 Selection

6.6.2.1 Fisher discriminant

Combinatorial background is reduced with a Fisher discriminant based on the impact parameters (IPs) of the daughter tracks (d^\pm) and of the reconstructed V^0 mother, where the impact parameter is defined as the minimum distance of closest approach to the nearest reconstructed primary interaction vertex measured in mm.⁵ The Fisher discriminant:

$$\mathcal{F}_{\text{IP}} = a \log_{10}(d_{\text{IP}}^+/1 \text{ mm}) + b \log_{10}(d_{\text{IP}}^-/1 \text{ mm}) + c \log_{10}(V_{\text{IP}}^0/1 \text{ mm}) \quad (6.6)$$

is optimised for signal significance ($S/\sqrt{S+B}$) on simulated events after the quality criteria described in Section 6.6.1. The coefficient values, $a = b = -c = 1$, were found to be suitable for all V^0 hadrons at both collision energies, as shown in Table 6.1, with the

⁵The Fisher discriminant is based on a selection developed for a previous LHCb analysis [145].

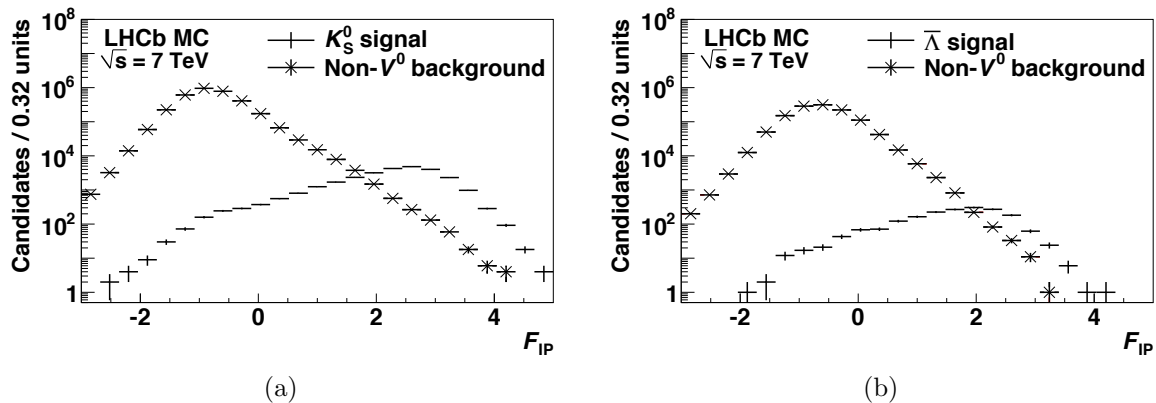


Figure 6.4: The Fisher discriminant \mathcal{F}_{IP} in 0.5 million Monte Carlo simulated minimum bias events at $\sqrt{s} = 7$ TeV for (a) K_S^0 and (b) $\bar{\Lambda}$.

Table 6.1: The optimised coefficients of the Fisher discriminant \mathcal{F}_{IP} (Eqn. 6.6) for $\bar{\Lambda}$, Λ and K_S^0 at $\sqrt{s} = 0.9$ and 7 TeV and found from MC studies using the multivariate analysis package TMVA [150]. Common values of each coefficient were used for all V^0 species at both energies to simplify analysis of the selection systematics.

\sqrt{s}	0.9 TeV			7 TeV			Used
	Λ	$\bar{\Lambda}$	K_S^0	Λ	$\bar{\Lambda}$	K_S^0	
a	1.0	0.9	1.0	1.0	0.8	1.0	1.0
b	1.0	1.0	1.0	0.8	1.0	1.0	1.0
c	-1.0	-1.0	-1.0	-1.1	-1.1	-1.1	-1.0

cut value $\mathcal{F}_{\text{IP}} > 1$. Example distributions of \mathcal{F}_{IP} are given in Fig. 6.4.

This discriminant is well suited to select V^0 particles produced directly from the primary interaction, referred to later in this chapter as “prompt”. With positive coefficients a and b , \mathcal{F}_{IP} is proportional to the daughter IPs, i.e. is large for long-lived mothers like Λ , $\bar{\Lambda}$ and K_S^0 . With a negative coefficient c , \mathcal{F}_{IP} is inversely proportional to the mother IP, i.e. is also large for prompt V^0 mothers.

The VELO working group measured significant differences between impact parameter resolution in data and in MC simulation⁶ during the early running period when the data was taken for this analysis, as shown in Fig. 6.5. This resolution varies as a function of p_T and the reduction seen in data with respect to simulation changes from 20% to 27% over the measurement range of the analysis presented in this chapter, given in Section 6.6.5. This reduction is 23% at the peak V^0 transverse momentum of about 0.7 GeV/ c .

Such a reduction in IP resolution is also observed for V^0 hadrons selected for this analysis. Since the discriminant, \mathcal{F}_{IP} , is constructed from impact parameters, any difference between data and simulation would lead to a biased efficiency (see Section 6.6.6).

⁶The impact parameter resolution is estimated from the distance of closest approach of each track found with respect to a primary interaction vertex, which is reconstructed using the remainder of tracks in the same event [88].

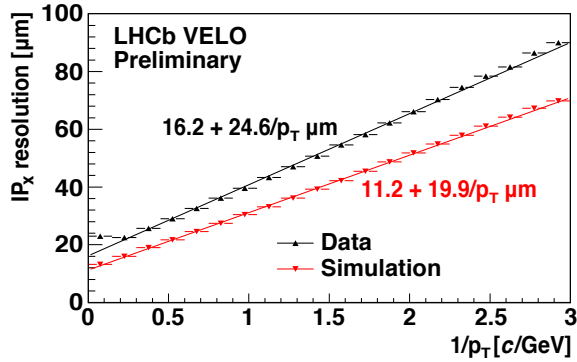


Figure 6.5: The impact parameter resolution measured as a function of p_T in data and simulation, produced by the VELO working group [88].

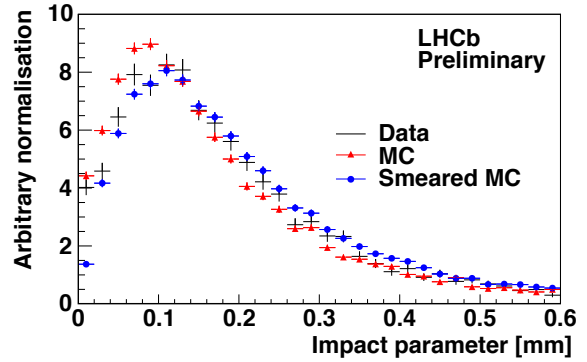


Figure 6.6: Λ impact parameter in data and MC simulation. The reduced resolution in data is modelled by smearing simulated primary and secondary vertex positions.

To avoid any bias, each simulated V^0 candidate’s IP is re-calculated after “smearing” the associated primary and secondary vertex positions to approximate this reduction in resolution.⁷ Each position coordinate is shifted by random sampling from a Gaussian with a width equal to 23% of the reconstruction uncertainty on that position. The smeared MC impact parameter distributions are closer to the data as, shown in Fig. 6.6.

6.6.2.2 V^0 background

V^0 selection can result in a well known misidentification between K_S^0 and Λ or $\bar{\Lambda}$ when one daughter pion is preferentially boosted in the laboratory frame. There is no misidentification between baryon and antibaryon because of the large mass difference between proton and pion. This V^0 background is often demonstrated using the Armenteros-Podolanski variables, q and α [152], as shown in Fig. 6.7 after the Fisher selection has been applied.

While these V^0 backgrounds can be removed with cuts on angular variables such as q and α , these cuts lead to non-linear backgrounds in the signal V^0 invariant mass distributions that can be problematic for the signal extraction fitting procedure described in Section 6.6.3.

Another well known approach to remove background from kinematically similar decays is the alternative mass veto. This method was found to be free from such background distortions and was preferred for this analysis. In this procedure, the invariant mass of each signal, say Λ , candidate is re-calculated with the appropriate background decay’s daughter mass hypotheses, e.g. $p\pi^-$ becomes $\pi^+\pi^-$. A veto around the resulting K_S^0 invariant mass peak can effectively remove the background.

This misidentified V^0 background is of greatest significance for purity of the Λ ($\bar{\Lambda}$) signals due to the relative abundance of K_S^0 . The Λ ($\bar{\Lambda}$) signal significance is optimised by a veto at $\pm 4.5 \text{ MeV}/c^2$ around the PDG K_S^0 mass after re-calculation of each candidate’s

⁷The impact parameter smearing follows the method employed for a previous LHCb analysis [151].

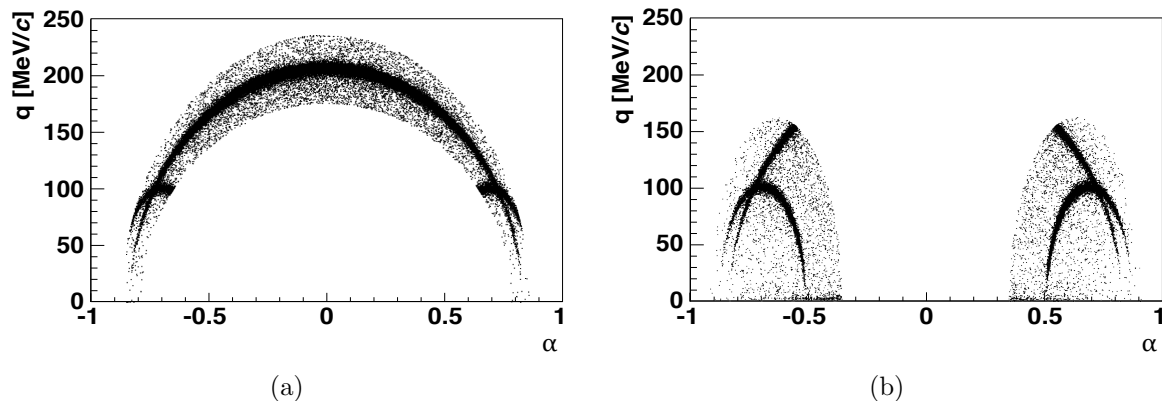


Figure 6.7: Selected (a) K_S^0 and (b) Λ & $\bar{\Lambda}$ candidates shown in the Armenteros-Podolanski parametrisation. The momentum of the negatively charged V^0 daughter perpendicular to the flight vector of the V^0 , $q = p_{\perp}^-$, is plotted against the asymmetry in the two daughters' momenta parallel to that vector, $\alpha = (p_{\parallel}^+ - p_{\parallel}^-)/(p_{\parallel}^+ + p_{\parallel}^-)$. True K_S^0 form a broad central arc, while $\bar{\Lambda}$ form a smaller arc to the left and Λ another to the right. The thickness of these signal arcs is defined by the momentum resolution of the experiment. The boundaries of the populated regions that enclose these signal arcs as well as the combinatorial background are defined by the selection mass windows.

invariant mass with the alternative daughter hypothesis. A similar veto to remove Λ ($\bar{\Lambda}$) from the K_S^0 sample is not found to improve significance so is not applied.

6.6.3 Signal extraction

After selection, V^0 yields are estimated from data and MC simulation by fits to the invariant mass distributions, examples of which are shown in Fig. 6.8. The observed invariant mass distributions of the long-lived $\bar{\Lambda}$, Λ and K_S^0 are dominated by the Gaussian measurement uncertainty on the momenta of their daughter tracks. At LHCb, these reconstructed mass distributions are each consistent with a double Gaussian function. The reasons for this are not yet understood. The invariant mass fits are carried out with the method of unbinned extended maximum likelihood and are parametrised by a double Gaussian signal (with a common mean) over a linear background.

The mean values show a small, but statistically significant, deviation from the known K_S^0 and Λ ($\bar{\Lambda}$) masses [63], reflecting the contemporary status of the momentum scale calibration of the experiment. The width of a signal peak is computed as the quadratic average of the two Gaussian widths, weighted by their signal fractions. This width is found to be constant as a function of p_T and increases linearly toward higher y , e.g. by 1.4 (0.8) MeV/c^2 per unit rapidity for K_S^0 (Λ and $\bar{\Lambda}$) at $\sqrt{s} = 7 \text{ TeV}$. The resulting signal yields are listed in Table 6.2.

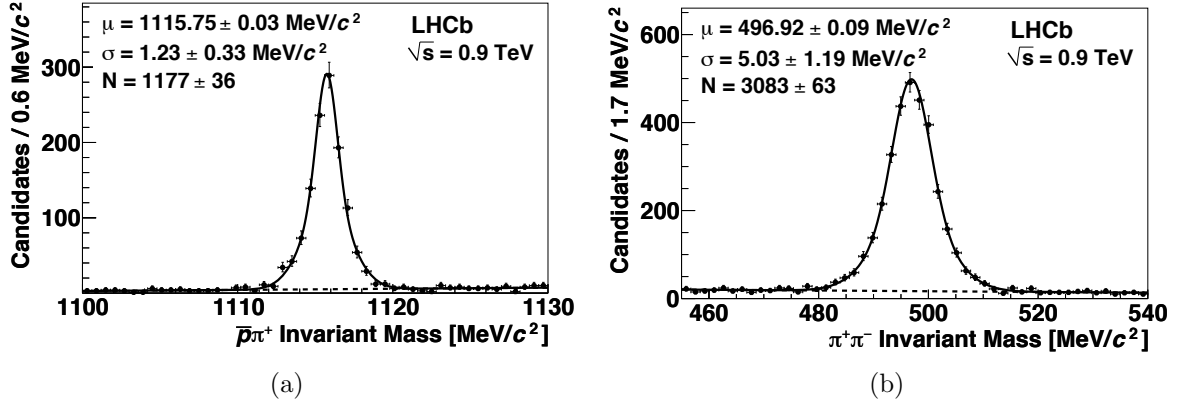


Figure 6.8: Invariant mass peaks for (a) $\bar{\Lambda}$ in the range $0.25 < p_T < 2.50$ GeV/c, $2.5 < y < 3.0$ and (b) K_S^0 in the range $0.65 < p_T < 1.00$ GeV/c, $3.5 < y < 4.0$ at $\sqrt{s} = 0.9$ TeV with field up. Signal yields, N , are found from fits (solid curves) with a double Gaussian peak with common mean, μ , over a linear background (dashed lines). The width, σ , is computed as the quadratic average of the two Gaussian widths weighted by their signal fractions.

Table 6.2: Integrated signal yields extracted by fits to the invariant mass distributions of selected V^0 candidates from data taken with magnetic field up and down at $\sqrt{s} = 0.9$ and 7 TeV.

\sqrt{s}	0.9 TeV		7 TeV		
	Magnetic field	Up	Down	Up	Down
$\bar{\Lambda}$		$3,442 \pm 64$	$4,096 \pm 72$	$258,927 \pm 642$	$132,548 \pm 459$
Λ		$4,877 \pm 75$	$5,416 \pm 80$	$294,005 \pm 677$	$141,861 \pm 463$
K_S^0		$35,785 \pm 203$	$40,234 \pm 219$	$2,737,093 \pm 1,935$	$1,365,993 \pm 1,365$

6.6.4 Kinematic corrections for simulated candidates

Significant differences are observed between V^0 kinematic variables reconstructed in data and in the Monte Carlo simulation used for efficiency determination. These differences can be a source of bias for the measurement of $\bar{\Lambda}/K_S^0$ given the different production kinematics of the baryon and meson. Simulated V^0 candidates are therefore weighted to match the two-dimensional p_T, y distributions observed in data. Examples of these distributions are shown projected along both axes in Fig. 6.9, before and after corrections.

The signal V^0 p_T and y distributions are estimated from selected data and MC candidates using sideband subtraction. Two-dimensional fits, linear in both p_T and y , are made to the ratio data/MC of these yields independently for $\bar{\Lambda}$, Λ and K_S^0 , for each magnet polarity and collision energy. The resulting functions are used to weight generated and selected V^0 candidates in the Monte Carlo simulation. These weights vary across the measured p_T, y range, with typical values between 0.8 and 1.2.

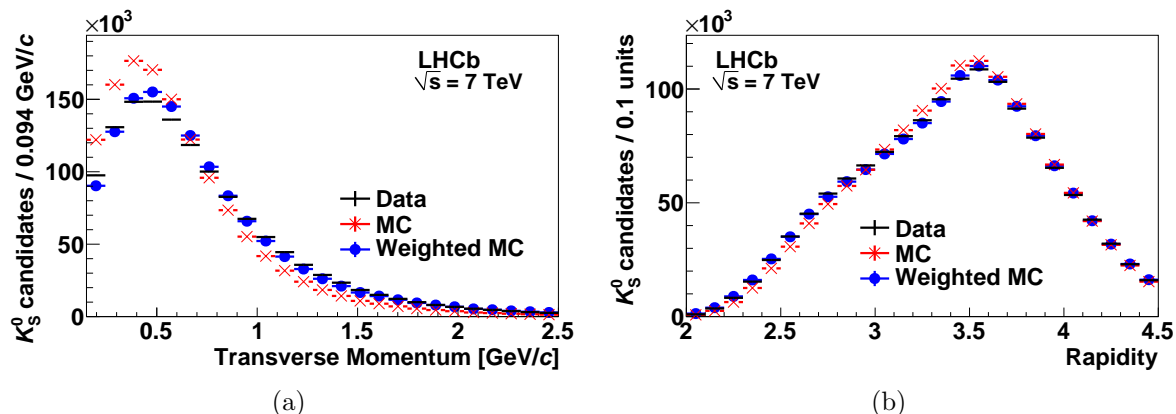


Figure 6.9: (a) Transverse momentum and (b) rapidity distributions for K_S^0 in data and Monte Carlo simulation at $\sqrt{s} = 7$ TeV. The difference between data and Monte Carlo is reduced by weighting the simulated candidates.

6.6.5 Measurement range and binning

The useful measurement range is found from selected V^0 candidates in data. Signal p_T and y distributions were estimated by weighting candidates as a function of signal and background fits to their respective invariant mass distributions.

The production ratios can be measured in the ranges $2.0 < y < 4.0$ (4.5) and 0.25 (0.15) $< p_T < 2.50$ GeV/ c from collisions at $\sqrt{s} = 0.9$ (7) TeV. The low p_T limit, for example, is defined by a drop in Λ ($\bar{\Lambda}$) signal statistics below 250 (150) MeV/ c in $\sqrt{s} = 0.9$ (7) TeV data. The reduction in acceptance over low p_T and high y at $\sqrt{s} = 0.9$ TeV is due to the retraction of the VELO described in Section 6.4.

The results are presented in three complementary binning schemes: projections over the full p_T range, the full y range, and a coarser two-dimensional binning. The rapidity range is split into 0.5-unit bins, while six bins in p_T are chosen to approximately equalise signal V^0 statistics in data. The two-dimensional binning combines adjacent pairs of p_T bins. The full analysis procedure is carried out independently in each p_T, y bin.

6.6.6 Efficiency correction

The efficiency for selecting prompt V^0 decays is estimated from simulation as

$$\varepsilon = \frac{N(V^0 \rightarrow d^+d^-)_{\text{Observed}}}{N(pp \rightarrow V^0X)_{\text{Generated}}}, \quad (6.7)$$

where the denominator is the number of prompt V^0 hadrons generated in a given p_T, y region after the weighting described in Section 6.6.4 and the numerator is the number of those weighted candidates found from the selection and fitting procedure described above. The efficiency therefore accounts for decays via other channels and losses from interactions with the detector material.

Table 6.3: A list of the longest lived ancestors of $\Lambda(\bar{\Lambda})$ baryons generated in LHCb MC simulation. A cut on the sum of all ancestor lifetimes of greater than 10^{-9} m (Eqn. 6.8) is used to select V^0 particles that are produced either directly in the primary interaction or from the short range strong and electromagnetic decays of particles produced at the PV.

Max. $c\tau$ ancestor	$c\tau$ [m]	Fraction [%]
PV	–	29.6
Σ^*	short-lived	19.4
Σ^0	10^{-11}	12.8
Ξ	10^{-2}	8.2
Ω	10^{-2}	0.1
Σ^\pm	10^{-2}	0.1
π^\pm	material interactions	4.1
K^\pm	"	12.8
K_S^0	"	0.2
K_L^0	"	9.5
p, n	"	2.8
Λ	elastic scattering	0.4
		100.0

Prompt V^0 hadrons are defined in Monte Carlo simulation by the cumulative lifetimes of their ancestors

$$\sum_{i=1}^n c\tau_i < 10^{-9} \text{ m}, \quad (6.8)$$

where τ_i is the proper decay time of the i^{th} ancestor. This veto is defined so as to keep only V^0 hadrons created either directly from the pp collisions or from the strong or electromagnetic decays of particles produced at those collisions, removing V^0 hadrons generated from material interactions (including regenerated K_S^0 , discussed in Section 6.1) and weak decays, as detailed for $\Lambda(\bar{\Lambda})$ in Table 6.3.

The Fisher discriminant \mathcal{F}_{IP} strongly favours prompt V^0 hadrons, however a small non-prompt contamination in data would lead to a systematic bias in the ratios. The fractional contamination of selected events is determined from simulation to be 2 – 6 % for $\bar{\Lambda}$ and Λ , depending on the measurement bin, and about 1 % for K_S^0 . This effect is dominated by weak decays rather than material interactions. These contaminant fractions are used to estimate systematic uncertainties on the ratios $\bar{\Lambda}/\Lambda$ and $\bar{\Lambda}/K_S^0$ of less than 2 and 3 % respectively.

6.7 Systematic uncertainties

The studies undertaken to evaluate systematic uncertainties on the ratios $\bar{\Lambda}/\Lambda$ and $\bar{\Lambda}/K_S^0$ are presented in the following sections. Each potential source of uncertainty is categorised as pertaining to either the experimental setup, Section 6.7.1, to a model-dependent re-

liance on MC generators, Section 6.7.2, or to the analysis procedure, Section 6.7.3. Where these estimates are found to be significant, their contribution to the uncertainty on each ratio is given. All important sources of systematic uncertainty are summarised in Table 6.5.

6.7.1 Experimental uncertainties

6.7.1.1 Track reconstruction

The track reconstruction efficiency depends on particle momentum. In particular, the tracking efficiency varies rapidly with momentum for tracks below 5 GeV/ c . Any bias is expected to be negligible for the ratio $\bar{\Lambda}/\Lambda$ but can be larger for $\bar{\Lambda}/K_S^0$ due to the different kinematics. Two complementary procedures are employed to check this efficiency.

First, track segments are reconstructed in the tracking stations upstream of the magnet. These track segments are then paired with the standard tracks reconstructed through the full detector and the pairs are required to form a K_S^0 to ensure only genuine tracks are considered. This track matching gives a measure of the tracking efficiency for the upstream tracking systems. The second procedure uses the downstream stations to reconstruct track segments, which are similarly paired with standard tracks to measure the efficiency of the downstream tracking stations. The agreement between these efficiencies in data and simulation is better than 5%.⁸

Again, these efficiencies are found for signal V^0 candidates by weighting using fits to the invariant mass distribution. To estimate the resulting uncertainty on $\bar{\Lambda}/\Lambda$ and $\bar{\Lambda}/K_S^0$, both ratios are re-calculated after weighting V^0 candidates by 95% for each daughter track with momentum below 5 GeV/ c . The resulting uncertainties on the ratios are negligible for $\bar{\Lambda}/\Lambda$ and less than 3% for $\bar{\Lambda}/K_S^0$.

6.7.1.2 Primary vertex reconstruction

The efficiency of primary interaction vertex reconstruction depends on the number of tracks in an event and may introduce a bias in the measured ratios if the detector occupancy is different for events containing K_S^0 , Λ or $\bar{\Lambda}$. This efficiency is compared in data and simulation using V^0 samples obtained with an alternative selection not requiring a primary vertex. Instead, the V^0 flight vector is extrapolated towards the beam axis to find the point of closest approach. The z coordinate of this point is used to define a pseudo-vertex, with $x = y = 0$.⁹ Candidates are kept if the impact parameters of their daughter tracks to this pseudo-vertex are larger than 0.2 mm. There is a significant overlap of signal candidates compared to the standard selection.

⁸The track-pairing test was carried out by T. Blake based on a previous study by the tracking working group [88].

⁹The pseudo-vertex test was carried out by T. Blake based on a previous LHCb analysis [145].

The primary vertex finding efficiency is then explored by taking the ratio of these selected events that do or do not have a standard primary vertex. This efficiency is similar for events containing $\bar{\Lambda}$, Λ and K_S^0 candidates: varying from below 10 % with 4 VELO tracks to about 80 % with 6 and above 90 % with 8 tracks. This efficiency is estimated for signal V^0 candidates using invariant mass fit weighting, similarly to Section 6.6.5. In order to investigate any bias in the measurement of $\bar{\Lambda}/\Lambda$ and $\bar{\Lambda}/K_S^0$, the ratios of these efficiencies are found for events containing different V^0 candidates, i.e. $\varepsilon_{\text{PV}}(\bar{\Lambda})/\varepsilon_{\text{PV}}(\Lambda \text{ or } K_S^0)$. Calculated in bins of p_T and y , these efficiency ratios agree between data and simulation to better than 2 % at both $\sqrt{s} = 0.9$ and 7 TeV. The resulting uncertainties on both $\bar{\Lambda}/\Lambda$ and $\bar{\Lambda}/K_S^0$ are less than 4 %.

6.7.2 Model-dependent uncertainties

6.7.2.1 Diffractive event fraction

The primary vertex finding algorithm requires at least three reconstructed tracks¹⁰ and therefore highly favours non-diffractive events due to the relatively low efficiency for finding diffractive interaction vertices, which tend to produce fewer tracks. In the LHCb MC simulation, the diffractive cross section accounts for 28 (25) % of the total minimum bias cross section of 65 (91) mb at 0.9 (7) TeV [104]. Due to the primary vertex requirement, only about 3 % of the V^0 candidates selected in simulation are produced in diffractive events.

These fractions are determined using PYTHIA 6, which models only soft diffraction. As a cross check, the fractions are also calculated with PYTHIA 8, which includes both soft and hard diffraction [149]. The variation on the overall efficiency between models is about 2 % for both ratios at $\sqrt{s} = 7$ TeV and close to 1 % at 0.9 TeV. Indeed, complete removal of diffractive events only produces a change of 1 to 2 % in the ratio $\bar{\Lambda}/\Lambda$ and 2 to 6 % for $\bar{\Lambda}/K_S^0$ across the measurement range.

6.7.2.2 Non-prompt efficiency correction

The measured efficiency corrected ratios $\bar{\Lambda}/\Lambda$ and $\bar{\Lambda}/K_S^0$ are subsequently corrected for non-prompt contamination as found from Monte Carlo simulation and defined by Eqn. 6.8. This procedure relies on simulation and the corrections may be biased by the choice of the LHCb MC generator tune.

To estimate a systematic uncertainty on the correction for non-prompt V^0 , the contaminant fractions are also calculated using two alternative tunes of PYTHIA 6: Perugia 0

¹⁰The minimum requirements for primary vertex reconstruction at LHCb can be approximated in Monte Carlo simulation by a generator-level cut requiring at least three charged particles from the collision with lifetime $c\tau > 10^{-9}$ m, momentum $p > 0.3$ GeV/c and polar angle $15 < \theta < 460$ mrad, including tracks reconstructed only in the VELO.

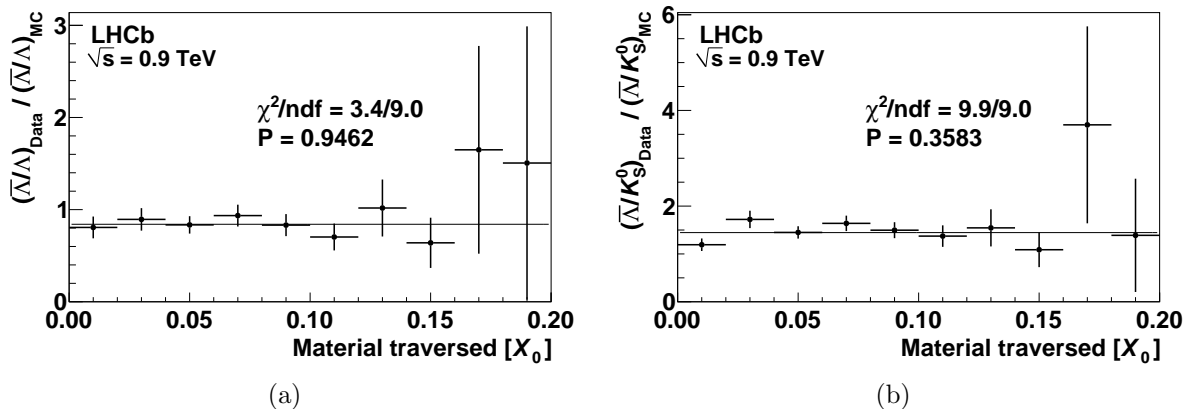


Figure 6.10: The double ratios (a) $(\bar{\Lambda}/\Lambda)_{\text{Data}}/(\bar{\Lambda}/\Lambda)_{\text{MC}}$ and (b) $(\bar{\Lambda}/K_S^0)_{\text{Data}}/(\bar{\Lambda}/K_S^0)_{\text{MC}}$ are shown as a function of the material traversed, in units of radiation length. Flat line fits, shown together with their respective χ^2 probabilities, give no evidence of a bias. Courtesy of F. Dettori.

and Perugia NOCR, introduced in Section 6.5. The maximum differences in non-prompt fraction across the measurement range and at both energies are less than 1 % for each V^0 species. The resulting uncertainties on the ratios are below 3 %.

Both this correction and its uncertainty are model dependent, therefore the final results are quoted both with and without this correction.

6.7.2.3 Material interactions

The influence of material interactions on these measurements is not expected to be large. V^0 absorption is limited by the requirement that each V^0 decay occurs within the most upstream tracker (the VELO). Secondary V^0 production in material is suppressed by the Fisher discriminant, Eqn. 6.6, which rejects V^0 candidates with large impact parameter.

Particle interactions within the detector are simulated using the GEANT 4 package, which implements interaction cross sections for each particle according to the LHEP physics list [108]. The simulated p , \bar{p} and π^\pm cross sections have been tested in the LHCb framework within the collaboration and are consistent with the LHEP values. The small measured differences are propagated to $\bar{\Lambda}/\Lambda$ and $\bar{\Lambda}/K_S^0$ to estimate uncertainties on the ratios of about 2.5 and 5 %, respectively.

The potential bias on the ratios is explored by measurement of both $\bar{\Lambda}/\Lambda$ and $\bar{\Lambda}/K_S^0$ as a function of material traversed (determined by the detector simulation), in units of radiation length, X_0 . Data and simulation are compared by their ratio, shown in Fig. 6.10. These ratios are consistent with a flat line as a function of X_0 , therefore any possible imperfections in the description of the detector material in simulation have a negligible effect on the V^0 ratio measurements. Note that the ratios of data/MC are not expected to be unity since simulations do not predict the same values for $\bar{\Lambda}/\Lambda$ and $\bar{\Lambda}/K_S^0$ as are observed in data.

6.7.3 Procedural uncertainties

6.7.3.1 Selection and signal extraction

The potential bias from the Fisher discriminant, \mathcal{F}_{IP} , is investigated using a pre-selected sample with only the track and vertex quality cuts applied. The distributions of \mathcal{F}_{IP} for Λ , $\bar{\Lambda}$ and K_S^0 in data and Monte Carlo simulation are estimated using sideband subtraction. The ratios of data/MC efficiencies are seen to be independent of the discriminant, giving confidence that the \mathcal{F}_{IP} distribution is well modelled in the simulation after the IP smearing described in Section 6.6.2. No systematic uncertainty is assigned to this selection requirement.

A good estimate of the reconstructed yields and their uncertainties in both data and simulation is provided by the fitting procedure but there may be a residual systematic uncertainty from the choice of this method. Comparisons are made using sideband subtraction and the resulting V^0 yields are in agreement with the results of the fits described in Section 6.6.3 at the 0.1% level. The resulting uncertainties on the ratios are less than 2%.

6.7.3.2 MC kinematic corrections

Simulated V^0 candidates are weighted to improve V^0 agreement with kinematic distributions in data. As described in Section 6.6, these weights are calculated from a two-dimensional fit, linear in both p_T and y , to the distribution of the ratio between reconstructed data and simulated Monte Carlo candidates.

This choice of parametrisation could be a source of systematic uncertainty, therefore alternative procedures are investigated including a two-dimensional polynomial fit to 3rd order in both p_T and y and a (non-parametric) bilinear interpolation. The results from each method are compared across the measurement range to estimate typical systematic uncertainties of 1 to 4% for $\bar{\Lambda}/\Lambda$ and 1 to 9% for $\bar{\Lambda}/K_S^0$.

6.7.4 Cross-checks

The lifetime distributions of reconstructed and selected V^0 candidates are consistent between data and simulation. The possible influence of transverse Λ ($\bar{\Lambda}$) polarisation was explored by simulations with extreme values of polarisation and found to produce no significant effect on the measured ratios. Potential acceptance effects were checked as a function of azimuthal angle, with no evidence of systematic bias.¹¹

The full analysis procedure is carried out independently on data sets taken with both field polarities. These results are compared by their χ^2 probabilities, $p(\chi^2, \text{ndf})$, considering statistical and uncorrelated systematic uncertainties. There is good agreement

¹¹These cross-checks were carried out by F. Dettori [153].

Table 6.4: Measured ratios from LHCb field up and down data sets are compared by p-value for each binning scheme and show reasonable consistency, taking into account statistical and uncorrelated systematic uncertainties.

Ratio	\sqrt{s}	Binning scheme	ndf	$p(\chi^2, \text{ndf})$
$\bar{\Lambda}/\Lambda$	0.9 TeV	p_T, y	12	0.031
		y	4	0.960
		p_T	6	0.814
	7 TeV	p_T, y	15	0.189
		y	5	0.002
		p_T	6	0.232
$\bar{\Lambda}/K_S^0$	0.9 TeV	p_T, y	12	0.176
		y	4	0.903
		p_T	6	0.613
	7 TeV	p_T, y	15	0.974
		y	5	0.631
		p_T	6	0.544

between the two sets of measurements as shown in Table 6.4, which gives confidence that any residual detector effects are small. These χ^2 probabilities are influenced by the MC kinematic correction procedure described in Section 6.6.4, particularly at the edge of the p_T, y parameter space. In the case of the $\bar{\Lambda}/\Lambda$ ratio, at $\sqrt{s} = 0.9$ TeV in the y binning scheme, this procedure leads to a divergence between LHCb field up and down results in the lowest y bin, reducing the χ^2 probability from 0.01 to 0.002. There is confidence that any change in the measured ratios due to this kinematic correction is accounted for in the systematic uncertainty, as described in Section 6.7.3.2.

6.7.5 Summary

The potential sources of systematic uncertainty or bias are summarised in Table 6.5. Limits and ranges indicate variation in uncertainty over the analysis bins. Sources of uncertainty common to both field configurations are identified for a later combination of these results (see Section 6.8.1).

6.8 Results

6.8.1 Combination of data sets

Throughout this analysis, the data sets taken with both magnetic field polarities are treated independently. There is good consistency for all measurements at both polarities, as described in Section 6.7.4. The field up and down results are therefore combined to maximise statistical significance.

Table 6.5: Relative systematic uncertainties are listed in descending order of importance. Ranges indicate uncertainties that vary across the measurement bins and/or by collision energy. Correlated sources of uncertainty between field up and down are identified.

Sources of systematic uncertainty	$\bar{\Lambda}/\Lambda$	$\bar{\Lambda}/K_S^0$
<i>Correlated between field up and down:</i>		
Material interactions	2.5 %	5 %
Diffractive event fraction	1 – 2 %	2 – 6 %
Primary vertex finding	< 4 %	< 4 %
Non-prompt fraction	< 2 %	< 3 %
Track finding	negligible	< 3 %
<i>Uncorrelated:</i>		
Kinematic correction	1 – 4 %	1 – 9 %
Signal extraction from fit	< 1 %	< 2 %
Total	3 – 6 %	6 – 10 %

The weighted average is calculated as $R = w_u R_u + w_d R_d$, where R indicates either ratio $\bar{\Lambda}/\Lambda$ or $\bar{\Lambda}/K_S^0$. The standard formula for combination of errors gives the uncertainty on R as:

$$\sigma^2 = w_u^2 \sigma_u^2 + w_d^2 \sigma_d^2 + 2w_u w_d c_u c_d \quad (6.9)$$

where σ represents the total uncertainty on a ratio measurement

$$\sigma^2 = s^2 + a^2 + c^2 \quad (6.10)$$

of which s is the statistical uncertainty and the systematic uncertainty is split into a and c , the components, which are uncorrelated and correlated respectively between field up and down data sets, as defined in Table 6.5.

We aim to find the values for the weights w_u and w_d that give minimal variance, σ^2 , on the final result, R . With substitution of $w_u = 1 - w_d$, the variance can be differentiated with respect to w_d as follows:

$$\begin{aligned} \sigma^2 &= (1 - w_d)^2 \sigma_u^2 + w_d^2 \sigma_d^2 + 2(1 - w_d)w_d c_u c_d \\ \frac{d}{dw_d}(\sigma^2) &= 2(w_d - 1)\sigma_u^2 + 2w_d \sigma_d^2 + 2(1 - 2w_d)c_u c_d \end{aligned} \quad (6.11)$$

Setting this differential equation to zero for a stationary point gives the following expression for the weight, w_d :

$$\begin{aligned} 0 &= w_d(\sigma_u^2 + \sigma_d^2 - 2c_u c_d) - \sigma_u^2 + c_u c_u \\ w_d = 1 - w_u &= \frac{\sigma_u^2 - c_u c_u}{\sigma_u^2 + \sigma_d^2 - 2c_u c_d} \end{aligned} \quad (6.12)$$

We take the second derivative to determine the type of stationary point, as follows:

$$\frac{d^2}{dw_d^2}(\sigma^2) = \sigma_u^2 + \sigma_d^2 - 2c_u c_d \quad (6.13)$$

This expression can be shown to be greater than zero for all real errors by substitution of Eqn. 6.10:

$$\begin{aligned} \frac{d^2}{dw_d^2}(\sigma^2) &= s_u^2 + s_d^2 + a_u^2 + a_d^2 + c_u^2 + c_d^2 - 2c_u c_d \\ &= s_u^2 + s_d^2 + a_u^2 + a_d^2 + (c_u - c_d)^2 \\ &> 0 \end{aligned} \quad (6.14)$$

The stationary point is therefore a minimum and the expression for the weights w_d and w_u given in Eqn. 6.12 is used to provide the desired minimal variance on the combined result, R .

6.8.2 Observations

The combined field up and down results for both ratios are shown in Fig. 6.11 as a function of y in three intervals of p_T at $\sqrt{s} = 0.9$ TeV and 7 TeV. The baryon/meson production ratio $\bar{\Lambda}/K_S^0$ shows a strong p_T dependence at both collision energies. The antibaryon/baryon production ratio $\bar{\Lambda}/\Lambda$ shows no significant p_T dependence.

Figs. 6.12 and 6.13 show comparisons between measurements of both ratios and the predictions of the PYTHIA 6 generator tunes: LHCb MC, Perugia0 and Perugia NOCR, as functions of p_T and y at $\sqrt{s} = 0.9$ TeV and $\sqrt{s} = 7$ TeV respectively. As discussed in Section 6.7.2.1, Monte Carlo studies suggest that the requirement for a reconstructed primary vertex results in only a small contribution from diffractive events to the selected V^0 sample, therefore non-diffractive simulated events are used for these comparisons. The predictions of LHCb MC and Perugia0 are similar throughout. The measured distributions of both ratios $\bar{\Lambda}/\Lambda$ and $\bar{\Lambda}/K_S^0$ as a function of p_T and y are inconsistent with each of the generator tunes tested.

Measurements of the ratio $\bar{\Lambda}/\Lambda$ are intermediate between the predictions of Perugia0 and Perugia NOCR. As a function of y , the data are consistent with Perugia0 in the low range but approach Perugia NOCR at higher rapidities. As a function of p_T , the data are closer to Perugia NOCR at $\sqrt{s} = 0.9$ TeV but closer to Perugia0 at 7 TeV.

The ratio $\bar{\Lambda}/K_S^0$ is significantly larger in data than the MC predictions at both collision energies and across all measurement bins. The data show a stronger dependence of baryon/meson production on p_T , with the ratio increasing faster than predicted by Perugia0.

Particle production in pp collisions involves a conversion of the initial protons' kinetic

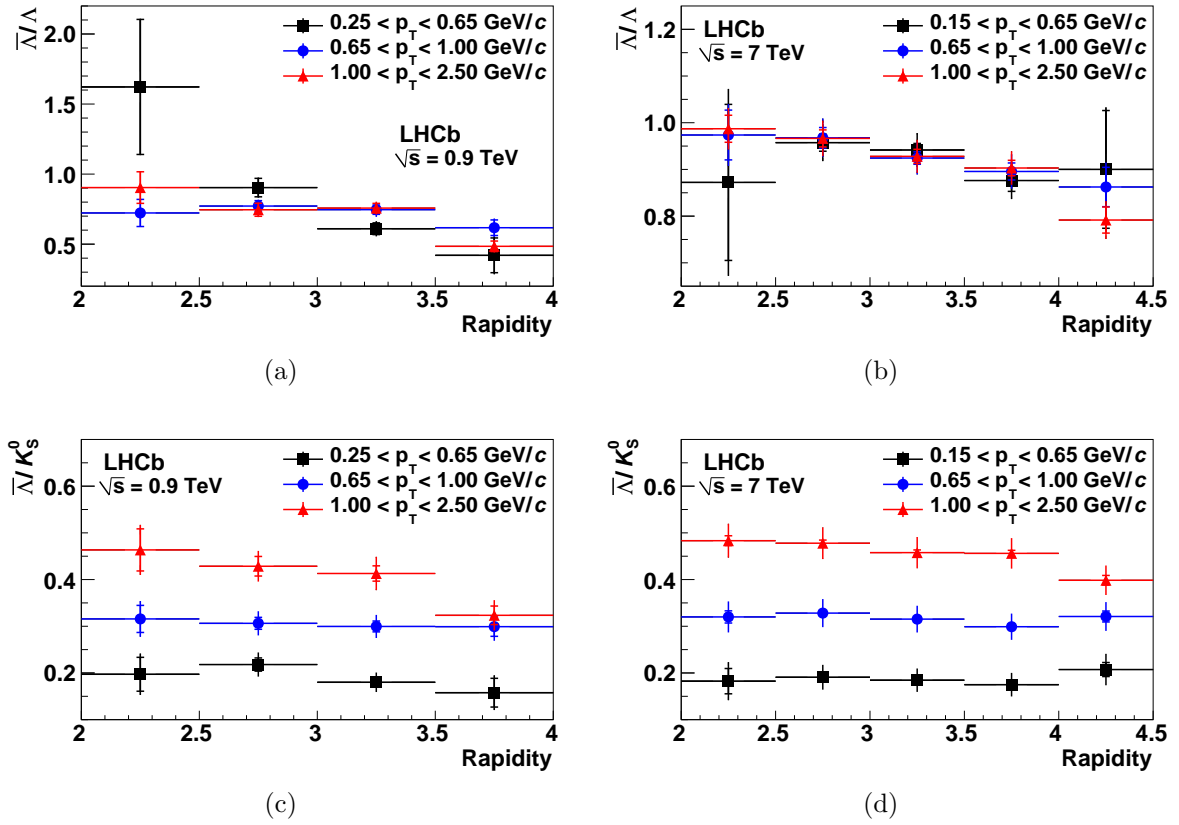


Figure 6.11: The ratios $\bar{\Lambda}/\Lambda$ and $\bar{\Lambda}/K_S^0$ from the full analysis procedure at (a) & (c) $\sqrt{s} = 0.9$ TeV and (b) & (d) 7 TeV are shown as a function of rapidity, compared across intervals of transverse momentum. Vertical lines show the combined statistical and systematic uncertainties. The statistical component lies within the short horizontal bars (where visible).

energy into the masses of the new particles, such as Λ , $\bar{\Lambda}$ and K_S^0 . This conversion can be pictured as a deceleration of the incoming protons and is related to the Lorentz invariant rapidity loss from the beam protons to the new particles produced, $\Delta y = y_{\text{beam}} - y$. To compare results at both collision energies, and to probe scaling violation, both production ratios are shown in Fig. 6.14 as a function of Δy . The rapidity of the proton beam, y_{beam} , is calculated for the protons travelling anticlockwise around the LHC, which is equivalent to travel along the positive z direction through the LHCb detector. At $\sqrt{s} = 0.9$ TeV, y_{beam} is about 6.9 and is approximately 8.9 at 7 TeV.

Excellent agreement is observed at the overlap between results at $\sqrt{s} = 0.9$ and 7 TeV as well as with results from STAR from pp collisions at $\sqrt{s} = 0.2$ TeV [142]. The measured ratios are also consistent with results published by ALICE and CMS, although their combination of Λ and $\bar{\Lambda}$ statistics does not allow comparison in Fig. 6.14 [143, 144].

The combined field up and down results are also given in tables in Appendix B.1. Results without applying the model-dependent non-prompt correction, as discussed in Section 6.7.2.2, are shown for comparison in Appendix B.2.

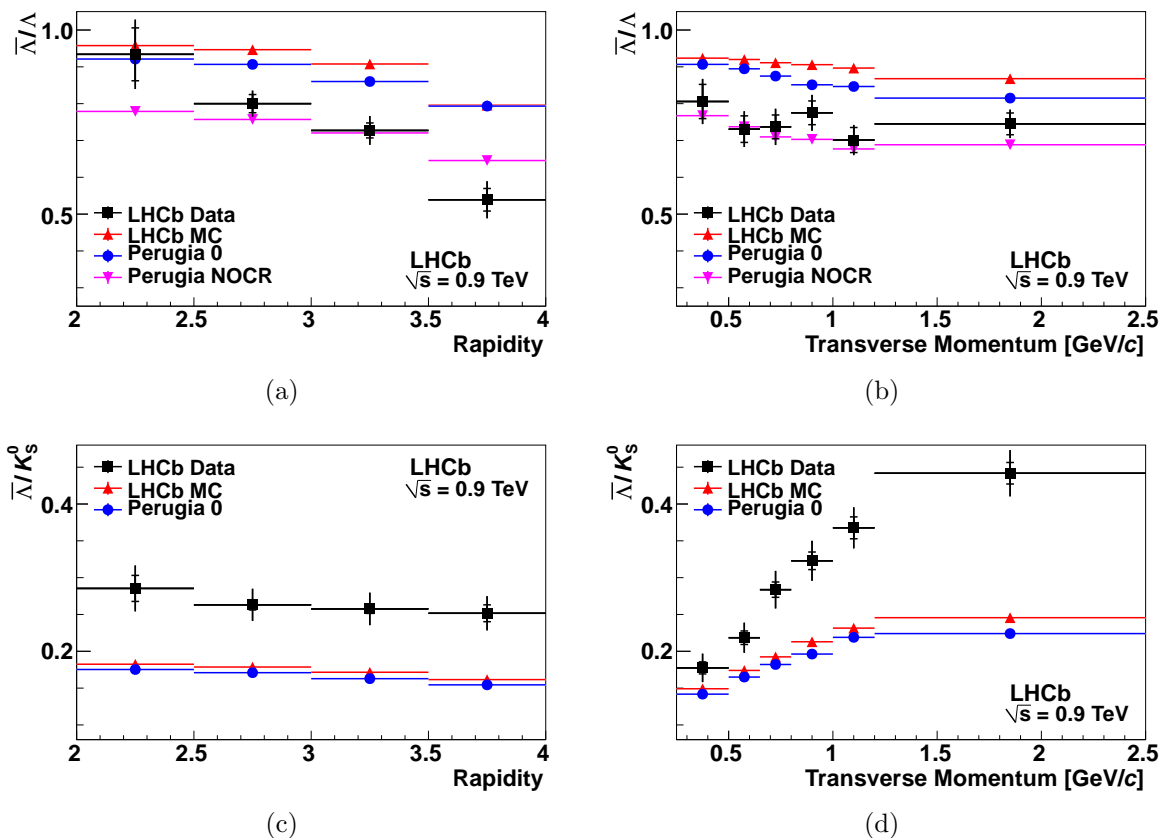


Figure 6.12: The ratios $\bar{\Lambda}/\Lambda$ and $\bar{\Lambda}/K_S^0$ at $\sqrt{s} = 0.9$ TeV are compared with the predictions of the LHCb MC, Perugia0 and Perugia NOCR as a function of (a) & (c) rapidity and (b) & (d) transverse momentum. Vertical lines show the combined statistical and systematic uncertainties. The statistical component lies within the short horizontal bars (where visible).

6.9 Recent development of the Perugia tunes

The publication of the strange hadron production ratios presented in this chapter, along with other recent minimum bias physics results, has influenced the development of the new standard PYTHIA 6 family of tunes, collectively called Perugia2011, as reported in Ref. [154].

The Perugia2011 tunes have incorporated increased baryon production, particularly for strange baryons, to match the larger-than-predicted p/π ratio from STAR [155] as well as the $\bar{\Lambda}/K_S^0$ ratio presented in this chapter. It is noted in the above report that this rate of baryon production is now at the upper limit allowed by LEP data. These changes with respect to the Perugia0 tune are made by modification of the following hadronisation model parameters:

- The diquark/quark production probability ratio in the Lund string model, $\text{PARJ}(1) = p(qq)/p(q)$, is increased from 0.073 to 0.087.
- The additional strange baryon production probability, $\text{PARJ}(3) = \frac{p(us)}{p(ud)}/\frac{p(s)}{p(d)}$, is increased slightly from 0.94 to 0.95.

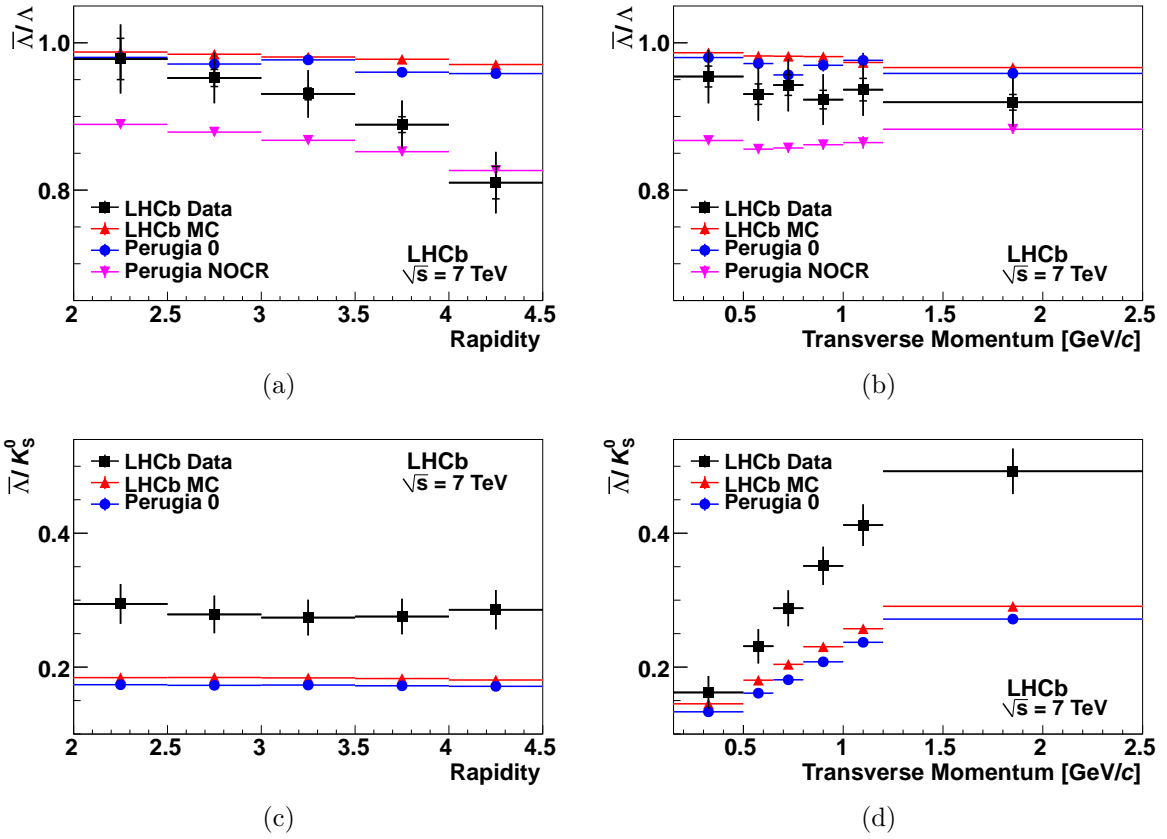


Figure 6.13: The ratios $\bar{\Lambda}/\Lambda$ and $\bar{\Lambda}/K_S^0$ at $\sqrt{s} = 7$ TeV compared with the predictions of the LHCb MC, Perugia 0 and Perugia NOCR as a function of (a) & (c) rapidity and (b) & (d) transverse momentum. Vertical lines show the combined statistical and systematic uncertainties. The statistical component lies within the short horizontal bars (where visible)

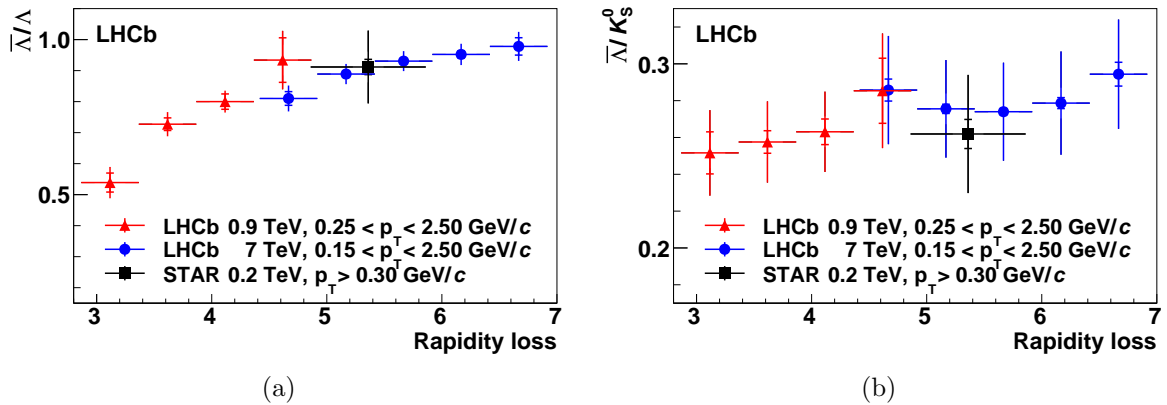


Figure 6.14: The ratios (a) $\bar{\Lambda}/\Lambda$ and (b) $\bar{\Lambda}/K_S^0$ from LHCb are compared at both $\sqrt{s} = 0.9$ TeV (triangles) and 7 TeV (circles) with the published results from STAR [142] (squares) as a function of rapidity loss, $\Delta y = y_{\text{beam}} - y$. Vertical lines show the combined statistical and systematic uncertainties. The statistical component lies within the short horizontal bars (where visible).

The Perugia 2011 tunes have introduced a new model for baryon transport from the beam remnant, motivated by the \bar{p}/p and $\bar{\Lambda}/\Lambda$ ratios measured by ALICE [156] and LHCb, respectively. The global probability of baryon transport has been increased with modifications to the string colour reconnection model parameters but the new model has introduced a suppression of these reconnections that grows with the separation in rapidity between string fragments and therefore reduces transport from the beam remnant at larger rapidities, as observed in this chapter for the ratio $\bar{\Lambda}/\Lambda$:

- The probability that a given string piece makes no colour reconnection to any other piece has previously been modelled as $p = (1 - \text{PARP}(78))^{N_{\text{int}}}$, where N_{int} is the number of interactions in the event, i.e. the reconnection probability is greater in events with many interactions. The amount of colour reconnection has been significantly increased by reducing the constant $\text{PARP}(78)$ from 0.33 to 0.036.
- The new model for colour reconnection introduces a suppression for large differences in rapidity, Δy , between any two string pieces, by a modification of the probability for no reconnections to $p = (1 - \text{PARP}(78))^{\Delta y \cdot \langle N_{\text{string}} - 1 \rangle}$, where $\langle N_{\text{string}} - 1 \rangle$ is the average number of string pieces available in an event for any given piece to reconnect with, i.e. all but itself. This model is set in PYTHIA 6 by changing the option $\text{MSTP}(95)$ from 6 to 8 [157].
- Colour reconnections are also suppressed for high transverse momentum string pieces by a factor, $f = 1/(1 + \text{PARP}(77)^2 \cdot \langle p_{\text{T}}^2 \rangle)$, where $\langle p_{\text{T}}^2 \rangle$ is the average squared transverse momentum of the hadrons that would be produced from a string piece [71]. This suppression has been enhanced by a change in the constant $\text{PARP}(77)$ from 0.9 to 1.0.

6.10 Conclusions

The measurements of the V^0 ratios $\bar{\Lambda}/\Lambda$ and $\bar{\Lambda}/K_{\text{S}}^0$ reported in this chapter show significant differences compared to the predictions of current Monte Carlo generator tunes.

There is good agreement, however, between $\bar{\Lambda}/\Lambda$ in data and the predictions of Perugia 0 at low rapidity, which is to be expected since the past experimental results used to validate this model have focused on this parameter space. The high rapidity region is better described by the extreme baryon transport model of Perugia NOCR, which does not allow interactions between final state parton showers and the proton beam remnants.

The measured ratio $\bar{\Lambda}/K_{\text{S}}^0$ is significantly larger than predicted by Perugia 0, i.e. relatively more baryons are produced in strange hadronisation at the LHC than expected, particularly at higher p_{T} . Similar results are found at both $\sqrt{s} = 0.9$ and 7 TeV.

LHCb has previously measured the production cross section of K_{S}^0 at $\sqrt{s} = 0.9$ TeV and observed good agreement with Perugia 0 [145]. This tune of PYTHIA 6 must therefore

underestimate the absolute $\bar{\Lambda}$ production rate and it may be that baryon and antibaryon production in general are underestimated. Further studies are required to determine if the agreement on K_S^0 production is also observed at $\sqrt{s} = 7$ TeV.

When plotted as a function of rapidity loss, Δy , there is excellent agreement between the measurements of both ratios at $\sqrt{s} = 0.9$ and 7 TeV, as well as with STAR's results published at 0.2 TeV. The broad coverage of the measurements in Δy provides a unique data set, which is complementary to previous results.

The V^0 production ratios presented here have already begun to help the development of hadronisation models to improve the predictions of Standard Model physics at the LHC, which will define the baseline for new discoveries.

Chapter 7

Summary

In October 2007 when I started this PhD, the LHCb detector was still under construction and the experiment hall was crowded with physicists installing components built by members of the collaboration all over the world. The RICH1 photon detector housing, for example, was manufactured by the Imperial College HEP group in London and the highly transparent aerogel tiles were developed for the RICH in Novosibirsk, by the Budker Institute of Nuclear Physics.

This preparatory period was a great time to be at CERN as a PhD student, with many opportunities to be involved in the final steps towards readiness for first collisions. In Chapter 5, I presented the RICH alignment procedure that was developed during this period. The need to align the optical components of the RICH detectors has been motivated with the aim to optimise the Cherenkov angle resolution of the system and so maximise the K/π separation efficiency. Observable quantities related to RICH misalignment were derived by geometrical arguments and correlations between these observables and the movements of individual optical components were established from simulations of the detector system using the LHCb software framework and GEANT 4 [108].

After the disappointment of the LHC's false start in 2008, collisions began successfully in November 2009, allowing me to put the RICH alignment strategy into practice. The initial detector output appeared nothing like the simulations and the data had to be divided up into sets of optical components before the characteristic sinusoidal misalignment signatures were observed. With the limited statistics of the early running period, a strategy was devised for an approximate alignment considering only four of the possible mirror pairs in RICH1 and the two photon detector panels of RICH2. These were the only component groupings for which both a sinusoidal misalignment signal was observable and for which sufficient statistics could be accumulated to calculate an alignment correction.

This initial alignment, though limited, was effective, with the Cherenkov angle resolutions for the RICH1 and RICH2 gases improved from 4.0 to 2.2 mrad and from 1.5 to 0.9 mrad respectively. Although there was still some way to go to reach the Monte Carlo predicted 1.6 and 0.7 mrad, this preliminary alignment showed that the method worked.

Further studies also revealed that Cherenkov resolutions very close to the MC target could be observed in data for individual photon detectors; pointing the way to a complete alignment including corrections to each HPD using the Magnetic Distortion Calibration System (MDCS) [129]. The results of the preliminary RICH alignment were presented at the RICH 2010 conference [1].

In the first months of running it was prudent to conduct physics studies that would be minimally affected by the early stage of calibration. With this in mind I undertook to measure strangeness production ratios with V^0 hadrons, as reported in Chapter 6, which could be triggered and selected using only tracking information. The tracking working group had measured the differences between reconstructed impact parameter resolutions in data and simulation, which allowed us to make a selection based on this quantity alone for which the simulation could be properly corrected to match data.

To motivate this study, I have introduced the Standard Model in Chapter 2, derived from the elegant concept of invariance under symmetry transformations that leads to the conservation of energy and momentum and to the generation of interactions between matter and the three fundamental forces. The weak interaction is discussed and I have outlined the mixing between quark generations that allows strange particles to decay to lighter hadrons to produce, for example, the neutral “ V ” decays considered in this thesis. The concept of a variable coupling strength has been introduced, with emphasis on the importance of this property of nature for the strong force. The difficulties encountered in predicting strong interactions in the non-perturbative regime, where the strong coupling α_s is large, are addressed by phenomenological models and Monte Carlo generators such as PYTHIA 6, used by the LHCb collaboration.

In Chapter 3 I have introduced the divide-and-conquer strategy employed to make predictions for pp interactions at the LHC. The proton momentum fraction carried by the constituent partons is extracted from experimentally determined PDFs and the hard parton-parton interactions are calculated perturbatively. These predictions can be tested at the LHC by measurements of Drell-Yan lepton production. Collisions that produce hadrons are more difficult to predict. The process of parton showering is introduced and the Lund string model is outlined, which aims to describe how these partons combine to produce the mesons and baryons observed by HEP experiments. Measurements of strangeness production are a powerful tool for the development of hadronisation models such as the Lund string, since strange quarks sit in a Goldilocks zone, where they are light enough to be produced by the hadronisation process and yet do not provide a net contribution to the structure of the colliding protons.

The V^0 ratio measurements \bar{A}/A and \bar{A}/K_S^0 , which have been reported by me and published on behalf of LHCb [3], have shown significant differences compared to current tunes of Monte Carlo generators. The baryon/meson ratio is significantly larger than predicted, suggesting an enhancement of baryon production at the LHC. The forward

rapidity coverage of LHCb provides a unique test of the antibaryon/baryon ratio. The results presented in this thesis show a significant deviation from predictions of the standard generator tune Perugia0 in the high rapidity region. This deviation is well matched by Perugia NOCR, a generator model with more localised string fragmentation, which does not connect final state parton showers to the proton beam remnants. These results have already begun to be of great use for the development of such models, as discussed in Section 6.9.

The LHCb detector had accumulated 680.8 pb^{-1} at $\sqrt{s} = 7 \text{ TeV}$ as of 14 August 2011, and the calibration of the RICH and other subdetectors has progressed significantly. To date, the LHCb collaboration has published nine papers, including measurement of the relative fractions of $B^0 \rightarrow D^- K^+$, $B^0 \rightarrow D^- \pi^+$ and $B_s^0 \rightarrow D_s^- \pi^+$, which would not have been possible without K/π separation from a well-functioning RICH system. The LHC will continue to provide pp collisions at $\sqrt{s} = 7 \text{ TeV}$ into 2012 and LHCb aims to increase its data set up to about 2 fb^{-1} . PhD students starting on LHCb this year will have the fantastic opportunity to work on world-beating measurements to test the Standard Model at the only LHC experiment to already be operating at (and beyond) optimal design conditions. I wish them well and would recommend this PhD programme to anyone.

Appendix A

The LAMS control project

A control project has been developed using the SCADA framework PVSS II 3.8 to automate the operation of the RICH Laser Alignment Monitoring System (LAMS), introduced in Section 5.9. The project includes a Graphical User Interface (GUI) to facilitate manual operation of the LAMS. The control software runs on a dedicated Linux server at the LHCb experiment site. Interaction with the 15 cameras is carried out over the internet using video servers connected to each camera.

The project is designed around a central data point archive, as illustrated in Fig. A.1. A continuously running control process follows an automated sequence of steps, updating the archive with its current progress and results and monitoring a data point that can indicate manual intervention. The automated loop proceeds as follows:

1. Check that manual control has not been requested.
2. Continue if prescribed time (to the minute) has been reached for any camera.
3. Check whether the scheduled action has already been taken (the loop may run many times per minute). If not, continue.
4. Ping camera server and, if successful, request image. Otherwise, report error.
5. Launch stand-alone analysis algorithm and monitor status code in the data point archive for its response. Timeout after 20 s.
6. If returned, check analysis status code for reported errors. If OK, the analysis results are archived with a time stamp.
7. Wait five seconds then repeat.

Image collection is scheduled for minutes with the same integer value as the camera identification number, e.g. images from RICH 2 camera 7 are taken at 7 minutes past each hour.

The RICH 2 cameras allow adjustment of exposure and gain settings in order to optimise the observed laser spot size and contrast for analysis. In RICH 1, the cameras were chosen for radiation tolerance due to their proximity to the interaction point (Fig. 4.4) and provide no possibility for customisation. The adjustment for spot size is therefore made globally for all RICH 1 cameras by variation of the laser intensity, then the RICH 2 cameras are individually optimised. Over time, it was found that the RICH 2 camera settings had to be periodically re-adjusted. The LAMS control project was therefore designed to record the exposure and gain settings along with each image.

Each camera sees two spots, as described in Section 5.9. Each image is analysed to extract these spot positions and intensities using an algorithm written in C++ by my fellow Imperial College PhD student Fatima Soomro and described in Refs. [158, 159]. Communication between the LAMS project and this algorithm is facilitated by CERN's Distributed Information Management (DIM) system [160]. Results are stored in the LAMS project's data point archive that can be accessed to view trends, for example in spot separation, which is indicative of RICH misalignment.

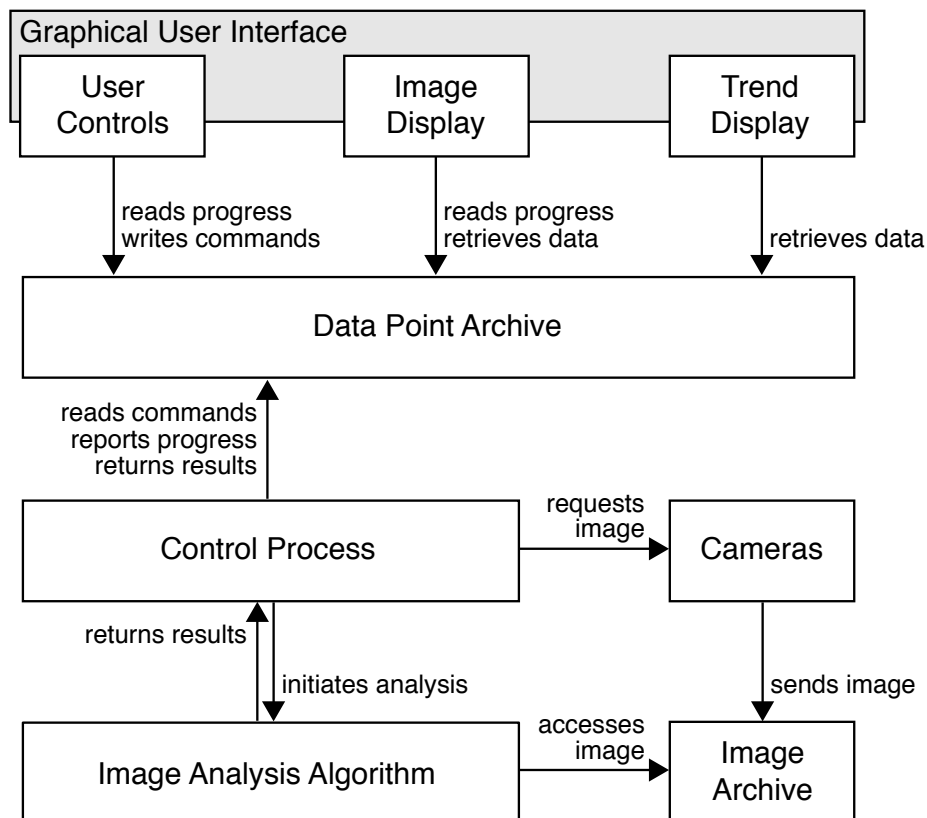
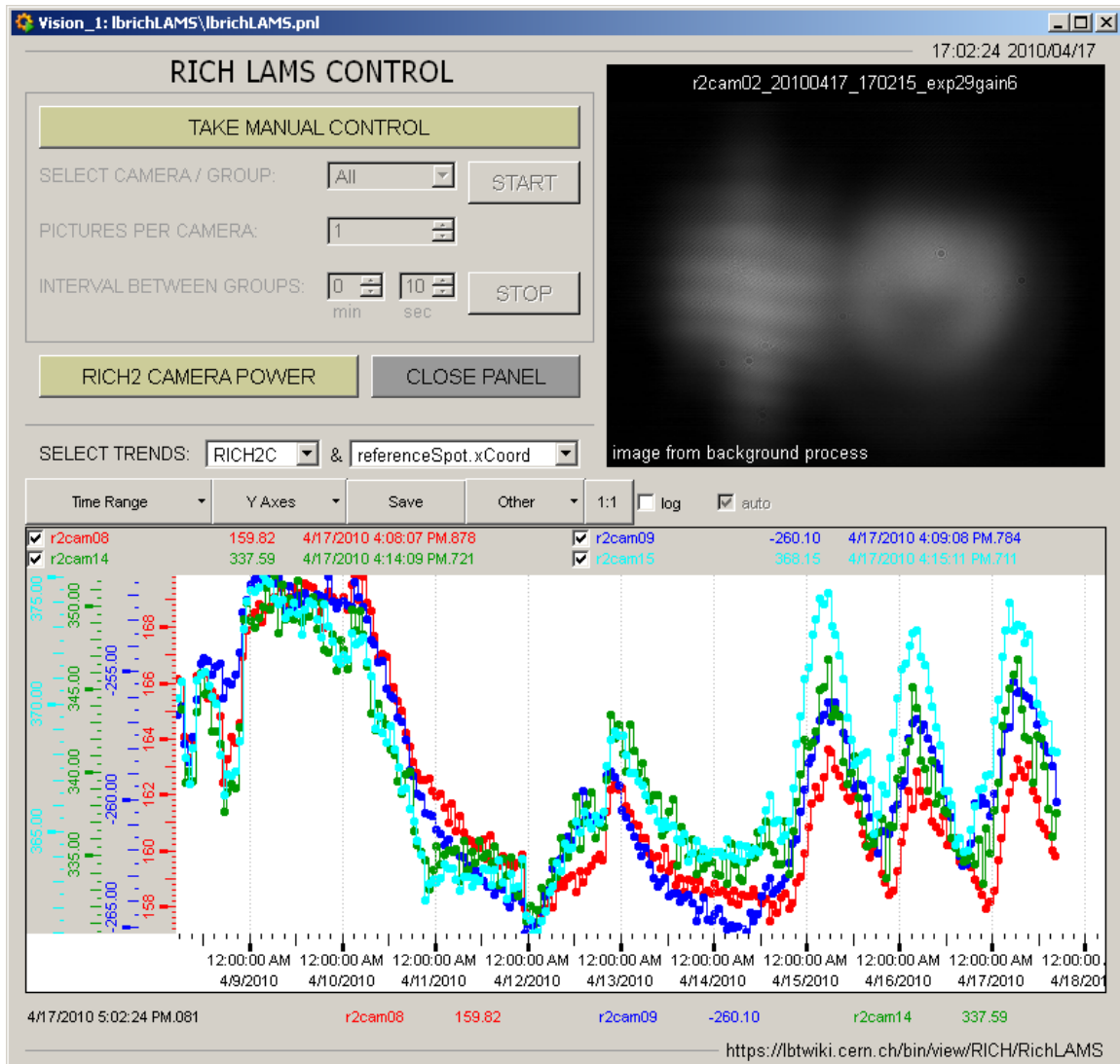
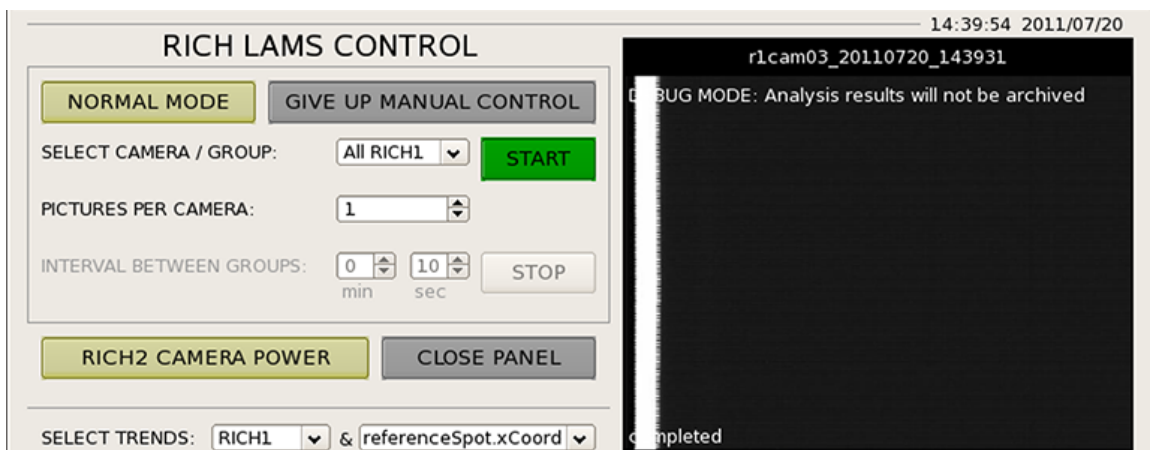


Figure A.1: A flow diagram to illustrate the major elements and communication channels of the LAMS control project. The direction of an arrow represents the flow of information or action, e.g. the image display object reads information from the data point archive. The control process object requests an image from a camera's video server, which is sent to the image archive. The control process initiates the analysis algorithm that triggers the algorithm to access an image from the archive.



(a)



(b)

Figure A.2: (a) Screenshot of the LAMS control project GUI (running under Windows XP), passively monitoring the automatic image capture process while being used to display trend data on the reference spot positions of four of the RICH 2 cameras. (b) Screenshot of the GUI (running under Scientific Linux) being used to manually take pictures of the RICH 1 cameras during testing with LHCb's magnetic field ramping up. Debug mode is used so as not to archive image analysis results from cameras that malfunction at high field strength.

A GUI has also been developed as part of the control system (Fig. A.2(a)) that allows monitoring and manual control of the processes described above, as well as the display of accumulated image analysis results. The panel can be accessed by the LHCb shift crew from computers running either Linux or Windows.

Under manual control, the panel can be used to take multiple images, at time intervals of up to 30 minutes, for one camera or a group of cameras, such as all those in RICH 1. The user may choose to block the archival of analysis results for these images by choosing “Debug Mode”, as shown in Fig. A.2(b). After 30 minutes of inactivity, manual control is rescinded and the control system restarts the automated process described above.

The control project has been successfully taking images and archiving analysis results since October 2008. The system is fully automated, including restart in case of power failure at the experiment site. The future use of this data is however unclear. This initial plan to calculate alignment corrections has been shelved after the successful alignment from collision data presented in Chapter 5.

Appendix B

V^0 production ratio tables

B.1 Tabulated results

Table B.1: The production ratios $\bar{\Lambda}/\Lambda$ and $\bar{\Lambda}/K_S^0$, measured at $\sqrt{s} = 0.9$ TeV, are quoted in percent with statistical and systematic uncertainties as a function of (a) & (b) rapidity, y , and (c) transverse momentum, p_T [GeV/ c].

(a)				
$\bar{\Lambda}/\Lambda$	$2.0 < y < 2.5$	$2.5 < y < 3.0$	$3.0 < y < 3.5$	$3.5 < y < 4.0$
$0.25 < p_T < 2.50$	$93.4 \pm 7.2 \pm 6.1$	$80.0 \pm 2.5 \pm 2.5$	$72.7 \pm 2.0 \pm 3.3$	$53.9 \pm 3.1 \pm 4.0$
$0.25 < p_T < 0.65$	$162.2 \pm 48.2 \pm 6.6$	$90.4 \pm 6.6 \pm 3.0$	$61.0 \pm 4.2 \pm 3.5$	$42.0 \pm 12.4 \pm 5.3$
$0.65 < p_T < 1.00$	$72.3 \pm 9.7 \pm 2.5$	$77.2 \pm 3.9 \pm 2.4$	$74.6 \pm 3.3 \pm 3.9$	$61.7 \pm 5.6 \pm 3.6$
$1.00 < p_T < 2.50$	$90.4 \pm 11.3 \pm 2.8$	$74.5 \pm 4.6 \pm 2.4$	$75.7 \pm 3.4 \pm 3.1$	$48.5 \pm 3.8 \pm 2.2$

(b)				
$\bar{\Lambda}/K_S^0$	$2.0 < y < 2.5$	$2.5 < y < 3.0$	$3.0 < y < 3.5$	$3.5 < y < 4.0$
$0.25 < p_T < 2.50$	$28.5 \pm 1.8 \pm 2.6$	$26.3 \pm 0.7 \pm 2.1$	$25.8 \pm 0.6 \pm 2.1$	$25.2 \pm 1.1 \pm 2.0$
$0.25 < p_T < 0.65$	$19.7 \pm 3.6 \pm 2.6$	$21.8 \pm 1.4 \pm 2.2$	$18.0 \pm 1.0 \pm 1.8$	$15.8 \pm 3.1 \pm 2.1$
$0.65 < p_T < 1.00$	$31.6 \pm 2.9 \pm 2.5$	$30.6 \pm 1.3 \pm 2.3$	$30.0 \pm 1.2 \pm 2.2$	$29.9 \pm 2.1 \pm 2.2$
$1.00 < p_T < 2.50$	$46.3 \pm 4.5 \pm 2.9$	$42.9 \pm 2.1 \pm 2.5$	$41.3 \pm 1.6 \pm 3.2$	$32.3 \pm 2.0 \pm 2.6$

(c)		
$2.0 < y < 4.0$	$\bar{\Lambda}/\Lambda$	$\bar{\Lambda}/K_S^0$
$0.25 < p_T < 0.50$	$80.6 \pm 4.6 \pm 4.0$	$17.7 \pm 0.8 \pm 1.7$
$0.50 < p_T < 0.65$	$73.1 \pm 3.6 \pm 3.2$	$21.8 \pm 0.9 \pm 1.8$
$0.65 < p_T < 0.80$	$73.7 \pm 3.2 \pm 3.7$	$28.4 \pm 1.0 \pm 2.3$
$0.80 < p_T < 1.00$	$77.5 \pm 3.2 \pm 3.7$	$32.3 \pm 1.2 \pm 2.4$
$1.00 < p_T < 1.20$	$70.1 \pm 3.4 \pm 2.3$	$36.8 \pm 1.5 \pm 2.4$
$1.20 < p_T < 2.50$	$74.5 \pm 3.0 \pm 2.5$	$44.2 \pm 1.5 \pm 2.8$

Table B.2: The production ratios $\bar{\Lambda}/\Lambda$ and $\bar{\Lambda}/K_S^0$, measured at $\sqrt{s} = 7$ TeV, are quoted in percent with statistical and systematic uncertainties as a function of (a) & (b) rapidity, y , and (c) transverse momentum, p_T [GeV/ c].

(a)					
$\bar{\Lambda}/\Lambda$	$2.0 < y < 2.5$	$2.5 < y < 3.0$	$3.0 < y < 3.5$	$3.5 < y < 4.0$	$4.0 < y < 4.5$
$0.15 < p_T < 2.50$	$97.8 \pm 2.8 \pm 3.8$	$95.2 \pm 1.2 \pm 3.2$	$93.1 \pm 0.8 \pm 3.1$	$88.9 \pm 1.1 \pm 3.1$	$81.0 \pm 2.2 \pm 3.5$
$0.15 < p_T < 0.65$	$87.2 \pm 16.7 \pm 11.0$	$95.7 \pm 1.8 \pm 3.5$	$94.2 \pm 1.4 \pm 3.3$	$87.6 \pm 2.3 \pm 3.2$	$90.0 \pm 12.6 \pm 4.2$
$0.65 < p_T < 1.00$	$97.4 \pm 5.3 \pm 3.9$	$96.8 \pm 2.2 \pm 3.5$	$92.4 \pm 1.3 \pm 3.3$	$89.6 \pm 1.8 \pm 3.2$	$86.2 \pm 4.2 \pm 3.2$
$1.00 < p_T < 2.50$	$98.7 \pm 2.9 \pm 3.4$	$96.6 \pm 1.8 \pm 3.3$	$92.8 \pm 1.5 \pm 3.2$	$90.3 \pm 1.7 \pm 3.2$	$79.2 \pm 2.8 \pm 2.9$

(b)					
$\bar{\Lambda}/K_S^0$	$2.0 < y < 2.5$	$2.5 < y < 3.0$	$3.0 < y < 3.5$	$3.5 < y < 4.0$	$4.0 < y < 4.5$
$0.15 < p_T < 2.50$	$29.4 \pm 0.6 \pm 2.9$	$27.9 \pm 0.3 \pm 2.8$	$27.4 \pm 0.2 \pm 2.7$	$27.6 \pm 0.3 \pm 2.6$	$28.6 \pm 0.6 \pm 2.9$
$0.15 < p_T < 0.65$	$18.2 \pm 2.7 \pm 3.0$	$19.1 \pm 0.3 \pm 2.6$	$18.5 \pm 0.2 \pm 2.5$	$17.5 \pm 0.4 \pm 2.5$	$20.7 \pm 1.5 \pm 3.0$
$0.65 < p_T < 1.00$	$32.0 \pm 1.3 \pm 3.0$	$32.8 \pm 0.6 \pm 3.0$	$31.5 \pm 0.4 \pm 2.8$	$29.9 \pm 0.5 \pm 2.8$	$32.1 \pm 1.2 \pm 2.9$
$1.00 < p_T < 2.50$	$48.3 \pm 1.1 \pm 3.5$	$47.8 \pm 0.7 \pm 3.3$	$45.8 \pm 0.6 \pm 3.3$	$45.6 \pm 0.7 \pm 3.2$	$39.9 \pm 1.0 \pm 3.0$

(c)		
$2.0 < y < 4.5$	$\bar{\Lambda}/\Lambda$	$\bar{\Lambda}/K_S^0$
$0.15 < p_T < 0.50$	$95.4 \pm 1.4 \pm 3.4$	$16.2 \pm 0.2 \pm 2.4$
$0.50 < p_T < 0.65$	$93.0 \pm 1.4 \pm 3.3$	$23.1 \pm 0.3 \pm 2.5$
$0.65 < p_T < 0.80$	$94.3 \pm 1.4 \pm 3.3$	$28.8 \pm 0.3 \pm 2.7$
$0.80 < p_T < 1.00$	$92.3 \pm 1.3 \pm 3.2$	$35.1 \pm 0.4 \pm 2.8$
$1.00 < p_T < 1.20$	$93.6 \pm 1.5 \pm 3.2$	$41.2 \pm 0.6 \pm 3.0$
$1.20 < p_T < 2.50$	$91.9 \pm 1.1 \pm 3.1$	$49.2 \pm 0.5 \pm 3.4$

B.2 Tabulated results before non-prompt correction

Table B.3: The production ratios $\bar{\Lambda}/\Lambda$ and $\bar{\Lambda}/K_S^0$ without non-prompt corrections at $\sqrt{s} = 0.9$ TeV are quoted in percent with statistical and systematic uncertainties as a function of (a) & (b) rapidity, y , and (c) transverse momentum, p_T [GeV/c].

(a)				
$\bar{\Lambda}/\Lambda$	$2.0 < y < 2.5$	$2.5 < y < 3.0$	$3.0 < y < 3.5$	$3.5 < y < 4.0$
$0.25 < p_T < 2.50$	$93.1 \pm 7.2 \pm 6.0$	$79.3 \pm 2.5 \pm 2.4$	$73.2 \pm 2.0 \pm 3.2$	$54.1 \pm 3.1 \pm 3.9$
$0.25 < p_T < 0.65$	$163.7 \pm 48.2 \pm 6.5$	$89.2 \pm 6.6 \pm 2.8$	$61.5 \pm 4.2 \pm 3.4$	$41.4 \pm 12.4 \pm 5.3$
$0.65 < p_T < 1.00$	$71.8 \pm 9.7 \pm 2.4$	$76.5 \pm 3.9 \pm 2.2$	$75.2 \pm 3.3 \pm 3.8$	$62.0 \pm 5.6 \pm 3.5$
$1.00 < p_T < 2.50$	$89.9 \pm 11.3 \pm 2.7$	$74.2 \pm 4.6 \pm 2.3$	$75.7 \pm 3.4 \pm 3.0$	$48.5 \pm 3.8 \pm 2.1$

(b)				
$\bar{\Lambda}/K_S^0$	$2.0 < y < 2.5$	$2.5 < y < 3.0$	$3.0 < y < 3.5$	$3.5 < y < 4.0$
$0.25 < p_T < 2.50$	$28.9 \pm 1.8 \pm 2.4$	$27.2 \pm 0.7 \pm 1.9$	$26.6 \pm 0.6 \pm 1.9$	$25.6 \pm 1.1 \pm 1.8$
$0.25 < p_T < 0.65$	$20.7 \pm 3.6 \pm 2.4$	$23.0 \pm 1.4 \pm 2.0$	$18.9 \pm 1.0 \pm 1.6$	$16.3 \pm 3.1 \pm 1.9$
$0.65 < p_T < 1.00$	$31.9 \pm 2.9 \pm 2.3$	$31.5 \pm 1.3 \pm 2.1$	$31.0 \pm 1.2 \pm 2.0$	$30.6 \pm 2.1 \pm 2.0$
$1.00 < p_T < 2.50$	$46.7 \pm 4.5 \pm 2.8$	$43.1 \pm 2.1 \pm 2.4$	$41.9 \pm 1.6 \pm 3.0$	$32.5 \pm 2.0 \pm 2.4$

(c)		
$2.0 < y < 4.0$	$\bar{\Lambda}/\Lambda$	$\bar{\Lambda}/K_S^0$
$0.25 < p_T < 0.50$	$80.1 \pm 4.6 \pm 3.9$	$18.8 \pm 0.8 \pm 1.5$
$0.50 < p_T < 0.65$	$72.9 \pm 3.6 \pm 3.1$	$22.9 \pm 0.9 \pm 1.6$
$0.65 < p_T < 0.80$	$73.9 \pm 3.2 \pm 3.6$	$29.5 \pm 1.0 \pm 2.1$
$0.80 < p_T < 1.00$	$77.5 \pm 3.2 \pm 3.5$	$33.1 \pm 1.2 \pm 2.3$
$1.00 < p_T < 1.20$	$70.1 \pm 3.4 \pm 2.1$	$37.2 \pm 1.5 \pm 2.2$
$1.20 < p_T < 2.50$	$74.4 \pm 3.0 \pm 2.3$	$44.5 \pm 1.5 \pm 2.6$

Table B.4: The production ratios $\bar{\Lambda}/\Lambda$ and $\bar{\Lambda}/K_S^0$ without non-prompt corrections at $\sqrt{s} = 7$ TeV are quoted in percent with statistical and systematic uncertainties as a function of (a) & (b) rapidity, y , and (c) transverse momentum, p_T [GeV/c].

(a)					
$\bar{\Lambda}/\Lambda$	$2.0 < y < 2.5$	$2.5 < y < 3.0$	$3.0 < y < 3.5$	$3.5 < y < 4.0$	$4.0 < y < 4.5$
$0.15 < p_T < 2.50$	$97.3 \pm 2.8 \pm 3.6$	$95.1 \pm 1.2 \pm 3.1$	$92.7 \pm 0.8 \pm 3.0$	$88.6 \pm 1.1 \pm 2.9$	$80.9 \pm 2.2 \pm 3.4$
$0.15 < p_T < 0.65$	$85.6 \pm 16.7 \pm 11.0$	$95.4 \pm 1.8 \pm 3.4$	$93.9 \pm 1.4 \pm 3.2$	$87.3 \pm 2.3 \pm 3.1$	$90.1 \pm 12.6 \pm 4.1$
$0.65 < p_T < 1.00$	$97.5 \pm 5.3 \pm 3.8$	$96.5 \pm 2.2 \pm 3.4$	$91.8 \pm 1.3 \pm 3.1$	$89.5 \pm 1.8 \pm 3.1$	$86.2 \pm 4.2 \pm 3.0$
$1.00 < p_T < 2.50$	$98.2 \pm 2.9 \pm 3.3$	$96.6 \pm 1.8 \pm 3.2$	$92.5 \pm 1.5 \pm 3.1$	$90.0 \pm 1.7 \pm 3.1$	$79.0 \pm 2.8 \pm 2.8$

(b)					
$\bar{\Lambda}/K_S^0$	$2.0 < y < 2.5$	$2.5 < y < 3.0$	$3.0 < y < 3.5$	$3.5 < y < 4.0$	$4.0 < y < 4.5$
$0.15 < p_T < 2.50$	$29.4 \pm 0.6 \pm 2.8$	$28.4 \pm 0.3 \pm 2.6$	$28.0 \pm 0.2 \pm 2.5$	$27.9 \pm 0.3 \pm 2.5$	$28.7 \pm 0.6 \pm 2.7$
$0.15 < p_T < 0.65$	$18.5 \pm 2.7 \pm 2.9$	$20.0 \pm 0.3 \pm 2.5$	$19.2 \pm 0.2 \pm 2.3$	$17.9 \pm 0.4 \pm 2.3$	$21.1 \pm 1.5 \pm 2.9$
$0.65 < p_T < 1.00$	$32.3 \pm 1.3 \pm 2.9$	$33.3 \pm 0.6 \pm 2.8$	$32.2 \pm 0.4 \pm 2.7$	$30.2 \pm 0.5 \pm 2.6$	$32.2 \pm 1.2 \pm 2.7$
$1.00 < p_T < 2.50$	$47.9 \pm 1.1 \pm 3.3$	$47.5 \pm 0.7 \pm 3.2$	$45.7 \pm 0.6 \pm 3.2$	$45.6 \pm 0.7 \pm 3.1$	$39.5 \pm 1.0 \pm 2.8$

(c)		
$2.0 < y < 4.5$	$\bar{\Lambda}/\Lambda$	$\bar{\Lambda}/K_S^0$
$0.15 < p_T < 0.50$	$95.0 \pm 1.4 \pm 3.2$	$16.9 \pm 0.2 \pm 2.3$
$0.50 < p_T < 0.65$	$92.9 \pm 1.4 \pm 3.2$	$23.8 \pm 0.3 \pm 2.4$
$0.65 < p_T < 0.80$	$94.0 \pm 1.4 \pm 3.2$	$29.4 \pm 0.3 \pm 2.5$
$0.80 < p_T < 1.00$	$91.9 \pm 1.3 \pm 3.1$	$35.5 \pm 0.4 \pm 2.7$
$1.00 < p_T < 1.20$	$93.1 \pm 1.5 \pm 3.1$	$41.3 \pm 0.6 \pm 2.9$
$1.20 < p_T < 2.50$	$91.8 \pm 1.1 \pm 3.0$	$48.9 \pm 0.5 \pm 3.2$

Appendix C

List of Acronyms

ALICE	A Large Ion Collider Experiment
AMS 2	Alpha Magnetic Spectrometer 2
ATLAS	A Toroidal LHC Apparatus
CCD	Charge-Coupled Device
CDF	Collider Detector at Fermilab
CERN	European Organization for Nuclear Research
CKM	Cabibbo Kobayashi Masukawa
CMS	Compact Muon Solenoid Experiment
<i>CP</i>	Charge-Parity Symmetry
CPU	Central Processing Unit
DIM	Distributed Information Management System
DLL	Delta Log-Likelihood Function
DØ	D Zero Experiment
DESY	German Electron Synchrotron
ECAL	Electromagnetic Calorimeter
FSR	Final State Radiation
GEM	Gas Electron Multiplier
GUI	Graphical User Interface
h.c.	Hermitian Conjugate
HCAL	Hadron Calorimeter

HEP	High Energy Physics
HERA	Hadron Electron Ring Accelerator
HLT	High Level Trigger
HPD	Hybrid Photon Detector
HQET	Heavy Quark Effective Theory
IND	Inelastic Non-Diffractive
IP	Impact Parameter
ISR	Intersecting Storage Ring
ISR	Initial State Radiation
IT	Inner Tracker
KEK	High Energy Accelerator Research Organization
KEKB	KEK B-factory
L0	Level 0 Trigger
LAMS	Laser Alignment Monitoring System
LEIR	Low Energy Ion Ring
LEP	Large Electron-Positron Collider
LHC	Large Hadron Collider
LHCb	Large Hadron Collider Beauty Experiment
MC	Monte Carlo Simulation
MDCS	Magnetic Distortion Calibration System
MB	Minimum Bias
MIP	Minimum Ionising Particle
MWPC	Multi-Wire Proportional Chamber
ndf	Number of Degrees of Freedom
NOCR	No Colour Reconnection
OT	Outer Tracker
PDF	Parton Density Function
PDG	Particle Data Group
PID	Particle Identification

PFF	Parton Fragmentation Function
PMT	Photomultiplier Tube
PS	Proton Synchrotron
PS	Pre-Shower Detector
PSB	Proton Synchrotron Booster
PV	Primary Vertex
PVSS II	Process Visualisation and Control System II, from ETM (Siemens)
QCD	Quantum Chromodynamics
QED	Quantum Electrodynamics
RICH	Ring Imaging Cherenkov Detector
RHIC	Relativistic Heavy Ion Collider
SCADA	Supervisory Control and Data Acquisition
SLAC	Stanford Linear Accelerator Center
SPD	Scintillating Pad Detector
SPS	Super Proton Synchrotron
SM	Standard Model
STAR	Solenoidal Tracker at RHIC
TT	Tracker Turicensis
UA1	Underground Area 1 Experiment
UE	Underlying Event
VEV	Vacuum Expectation Value
VELO	Vertex Locator
WLCG	Worldwide LHC Computing Grid
WMAP	Wilkinson Microwave Anisotropy Probe

Bibliography

- [1] LHCb Collaboration, C. G. Blanks, “RICH alignment at LHCb with collision data,” *Nucl. Instrum. Meth. A* **639** 215–218. Proceedings of the 7th International Workshop on Ring Imaging Cherenkov Detectors, May 2010, Cassis, France.
- [2] LHCb Collaboration, C. G. Blanks, “Particle production studies at LHCb.” PoS(ICHEP 2010)141. Proceedings of the 35th International Conference on High Energy Physics, July 2010, Paris, France.
- [3] LHCb Collaboration, R. Aaij *et al.*, “Measurement of V^0 production ratios in pp collisions at $\sqrt{s} = 0.9$ and 7 TeV,” *JHEP* **2011** (2011) 1–22.
- [4] D. J. Griffiths, “Introduction to elementary particles,” John Wiley & Sons, 1987.
- [5] L. Teng, “Particle accelerators: outlook for the twenty-first century.” Proceedings of the 2nd Asian Particle Accelerator Conference, September 2001, Beijing, China.
- [6] J. D. Cockroft, “Experiments on the interaction of high-speed nucleons with atomic nuclei,” in “Nobel Lectures, Physics 1942-1962,” Elsevier Publishing Company, Amsterdam, 1964.
- [7] E. T. S. Walton, “The artificial production of fast particles,” in “Nobel Lectures, Physics 1942-1962,” Elsevier Publishing Company, Amsterdam, 1964.
- [8] Nobelprize.org, “The Nobel Prize in physics 1906 – J. J. Thomson.” http://nobelprize.org/nobel_prizes/physics/laureates/1906.
- [9] Nobelprize.org, “The Nobel Prize in physics 1921 – A. Einstein.” http://nobelprize.org/nobel_prizes/physics/laureates/1921.
- [10] Nobelprize.org, “The Nobel Prize in physics 1936 – C. D. Anderson.” http://nobelprize.org/nobel_prizes/physics/laureates/1936.
- [11] Nobelprize.org, “The Nobel Prize in physics 1933 – P. A. M. Dirac.” http://nobelprize.org/nobel_prizes/physics/laureates/1933.
- [12] F. Halzern and A. Martin, “Quarks and leptons,” John Wiley & Sons, 1987.

- [13] L. Campbell and W. Garnett, “The life of James Clerk Maxwell,” Macmillan, 1882.
- [14] A. E. Noether, “Invariant variation problems,” *Gott. Nachr.* **1918** (1918) 235–257.
- [15] Y. Fukuda *et al.*, “Measurements of the solar neutrino flux from Super-Kamiokande’s first 300 days,” *Phys. Rev. Lett.* **81** (1998), no. 6, 1158–1162.
- [16] Nobelprize.org, “The Nobel Prize in physics 1965 – R. P. Feynman, J. Schwinger and S. Tomonaga.”
http://nobelprize.org/nobel_prizes/physics/laureates/1965.
- [17] R. Bouchendira *et al.*, “New determination of the fine structure constant and test of the quantum electrodynamics,” *Phys. Rev. Lett.* **106** (2011), no. 8, 080801.
- [18] E. Fermi, “Versuch einer theorie der β -strahlen,” *Zeitschrift für Physik A* **88** (1934) 161–177.
- [19] A. Salam, “Gauge unification of fundamental forces,” in “Nobel Lectures, Physics 1971-1980,” World Scientific Publishing Company, Singapore, 1992.
- [20] O. Klein, “On the theory of charged fields,” 1939. Proceedings of the conference organised by the International Institute of Intellectual Cooperation, Paris, France.
- [21] F. J. Hasert *et al.*, “Observation of neutrino-like interactions without muon or electron in the gargamelle neutrino experiment,” *Phys. Lett. B* **46** (1973), no. 1, 138–140.
- [22] S. L. Glashow, “Partial-symmetries of weak interactions,” *Nucl. Phys.* **22** (1961), no. 4, 579–588.
- [23] S. Weinberg, “A model of leptons,” *Phys. Rev. Lett.* **19** (1967), no. 21, 1264–1266.
- [24] A. Salam, “Weak and electromagnetic interactions.” Nobel Symposium 8, Aspenasgarden, Sweden, July 19-25, 1968. Elementary Particle Theory: Relativistic Groups and Analyticity, 367-377. Almqvist & Wiksell, Stockholm (1968).
- [25] T. D. Lee and C. N. Yang, “Question of parity conservation in weak interactions,” *Phys. Rev.* **104** (1956), no. 1, 254–258.
- [26] E. Ambler, R. W. Hayward, D. D. Hoppes, R. P. Hudson, and C. S. Wu, “Experimental test of parity conservation in beta decay,” *Phys. Rev.* **105** (1957), no. 4, 1413–1415.

- [27] J. H. Christenson, J. W. Cronin, V. L. Fitch, and R. Turlay, “Evidence for the 2π decay of the K_2^0 meson,” *Phys. Rev. Lett.* **13** (1964), no. 4, 138–140.
- [28] A. D. Sakharov, “Violation of CP invariance, C asymmetry, and baryon asymmetry of the universe,” *Pisma Zh. Eksp. Teor. Fiz.* **5** (1967) 32–35.
- [29] P. W. Higgs, “Spontaneous symmetry breakdown without massless bosons,” *Phys. Rev.* **145** (1966), no. 4, 1156–1163.
- [30] W. J. Murray *et al.*, “Proceedings of the school for experimental high energy physics students.” 30 August – 12 September 2010, Oxford, UK.
- [31] UA1 Collaboration, G. Arnison *et al.*, “Experimental observation of isolated large transverse energy electrons with associated missing energy at $\sqrt{s} = 540$ GeV,” *Phys. Lett. B* **122** (1983) 103–116.
- [32] UA1 Collaboration, G. Arnison *et al.*, “Experimental observation of lepton pairs of invariant mass around $95 \text{ GeV}/c^2$ at the CERN SPS collider,” *Phys. Lett. B* **126** (1983) 398–410.
- [33] H. Geiger and E. Marsden, “On a diffuse reflection of the α -particles,” *Proc. R. Soc. Lond., A* **82** (1909) 495–500.
- [34] E. Rutherford, “The scattering of α and β particles by matter and the structure of the atom,” *Philos. Mag.* **21** (1911) 669–688.
- [35] H. Yukawa, “On the interaction of elementary particles,” *Proc. Phys. Math. Soc. Japan* **17** (1935) 48.
- [36] S. H. Neddermeyer and C. D. Anderson, “Note on the Nature of Cosmic-Ray Particles,” *Phys. Rev.* **51** (1937) 884–886.
- [37] C. M. G. Lattes, H. Muirhead, G. P. S. Occhialini, and C. F. Powell, “Processes involving charged mesons,” *Nature* **159** (1947) 694–697.
- [38] M. Bartusiak, “Who ordered the muon?,” *The New York Times*. 27 September, 1987.
- [39] C. C. Butler and G. D. Rochester, “Evidence for the existence of new unstable elementary particles,” *Nature* **160** (1947) 855.
- [40] M. Gell-Mann, “Symmetries of baryons and mesons,” *Phys. Rev.* **125** (1962), no. 3, 1067–1084.
- [41] V. E. Barnes *et al.*, “Observation of a hyperon with strangeness minus three,” *Phys. Rev. Lett.* **12** (1964), no. 8, 204–206.

- [42] M. Gell-Mann, “A schematic model of baryons and mesons,” *Phys.Lett.* **8** (1964) 214–215.
- [43] G. Zweig, “An SU(3) model for strong interaction symmetry and its breaking,” .
Developments in the quark theory of hadrons, Vol. 1.
- [44] W. Pauli, “The connection between spin and statistics,” *Phys. Rev.* **58** (1940), no. 8, 716–722.
- [45] O. W. Greenberg, “Spin and unitary-spin independence in a paraquark model of baryons and mesons,” *Phys. Rev. Lett.* **13** (1964), no. 20, 598–602.
- [46] E. D. Bloom *et al.*, “High-energy inelastic $e-p$ scattering at 6° and 10° ,” *Phys. Rev. Lett.* **23** (1969), no. 16, 930–934.
- [47] M. Breidenbach *et al.*, “Observed behavior of highly inelastic electron-proton scattering,” *Phys. Rev. Lett.* **23** (1969), no. 16, 935–939.
- [48] Nobelprize.org, “The Nobel Prize in physics 1990 – J. I. Friedman, H. W. Kendall, R. E. Taylor.”
http://nobelprize.org/nobel_prizes/physics/laureates/1990.
- [49] H. Fritzsche and M. Gell-Mann, “Current algebra: Quarks and what else?,” *eConf C720906V2* (1972) 135–165. Proceedings of the 16th International Conference on High Energy Physics, Chicago, USA.
- [50] H. Fritzsche, M. Gell-Mann, and H. Leutwyler, “Advantages of the color octet gluon picture,” *Phys. Lett. B* **47** (1973), no. 4, 365–368.
- [51] TASSO Collaboration, R. Brandelik *et al.*, “Evidence for planar events in e^+e^- annihilation at high energies,” *Phys. Lett. B* **86** (1979), no. 2, 243–249.
- [52] S. L. Glashow, J. Iliopoulos, and L. Maiani, “Weak interactions with lepton-hadron symmetry,” *Phys. Rev. D* **2** (1970), no. 7, 1285–1292.
- [53] K. Makoto and T. Maskawa, “CP-violation in the renormalizable theory of weak interaction,” *Prog. Theo. Phys.* **49** (1973), no. 2, 652–657.
- [54] H. Harari, “A new quark model for hadrons,” *Phys. Lett. B* **57** (1975), no. 3, 265–269.
- [55] SLAC-SP-017 Collaboration, J. E. Augustin *et al.*, “Discovery of a narrow resonance in e^+e^- annihilation,” *Phys. Rev. Lett.* **33** (1974) 1406–1408.
- [56] E598 Collaboration, J. J. Aubert *et al.*, “Experimental observation of a heavy particle J,” *Phys. Rev. Lett.* **33** (1974) 1404–1406.

- [57] Nobelprize.org, “The Nobel Prize in physics 1976 – B. Richter, S. C. C. Ting.” http://nobelprize.org/nobel_prizes/physics/laureates/1976.
- [58] S. W. Herb *et al.*, “Observation of a dimuon resonance at 9.5 GeV in 400 GeV proton-nucleus collisions,” *Phys. Rev. Lett.* **39** (1977), no. 5, 252–255.
- [59] CDF Collaboration, F. Abe *et al.*, “Observation of top quark production in $p\bar{p}$ collisions with the Collider Detector at Fermilab,” *Phys. Rev. Lett.* **74** (1995), no. 14, 2626–2631.
- [60] DØ Collaboration, S. Abachi *et al.*, “Search for high mass top quark production in $p\bar{p}$ collisions at $\sqrt{s} = 1.8$ TeV,” *Phys. Rev. Lett.* **74** (1995), no. 13, 2422–2426.
- [61] N. Cabibbo, “Unitary symmetry and leptonic decays,” *Phys. Rev. Lett.* **10** (1963), no. 12, 531–533.
- [62] M. Kobayashi and T. Maskawa, “ CP -violation in the renormalizable theory of weak interaction,” *Prog. Theo. Phys.* **49** (1973), no. 2, 652–657.
- [63] K. Nakamura *et al.* (Particle Data Group), “Review of particle physics,” *J. Phys. G* **37** (2010) 075021.
- [64] ALEPH Collaboration, D. DeCamp *et al.*, “Determination of the number of light neutrino species,” *Phys. Lett. B* **231** (1989), no. 4, 519–529.
- [65] C. Csáki, C. Grojean, L. Pilo, and J. Terning, “Towards a realistic model of Higgsless electroweak symmetry breaking,” *Phys. Rev. Lett.* **92** (2004), no. 10, 101802.
- [66] N. Jarosik *et al.*, “Seven-year Wilkinson microwave anisotropy probe (WMAP) observations: Sky maps, systematic errors, and basic results,” *Astrophys. J. Sup. Ser.* **192** (2011), no. 2, .
- [67] R. P. Feynman and R. D. Field, “A parametrization of the properties of quark jets,” *Nucl. Phys. B* **136** (1978), no. 1, 1–76.
- [68] LEP Electroweak Working Group, SLD Electroweak Group, SLD Heavy Flavour Group, ALEPH Collaboration, DELPHI Collaboration, L3 Collaboration, OPAL Collaboration, SLD Collaboration, “Precision electroweak measurements on the Z resonance,” *Phys. Rept.* **427** (2006) 257–454.
- [69] S. Bethke, “The 2009 world average of $\alpha(s)$,” *Eur. Phys. J.* **C64** (2009) 689–703.

- [70] H1 Collaboration and ZEUS Collaboration, A. M. Cooper-Sarkar, “HERAPDF fits including $F_2(\text{charm})$ data.” PoS(DIS 2010)023. Proceedings of the 28th International Conference on Deep Inelastic Scattering and Related Subjects, April 2010, Florence, Italy.
- [71] S. M. T. Sjöstrand and P. Z. Skands, “PYTHIA 6.4 physics and manual,” *JHEP* **05** (2006) 026.
- [72] B. Andersson, G. Gustafson, G. Ingelman, and T. Sjöstrand, “Parton fragmentation and string dynamics,” *Phys. Rep.* **97** (1983), no. 2-3, 31–145.
- [73] “Convention for the establishment of a European organization for nuclear research,” CERN. Paris, 1 July 1953.
- [74] L. Evans and P. Bryant, “LHC machine,” *JINST* **3** (2008) S08001.
- [75] S. Dittmaier *et al.*, “Handbook of LHC Higgs cross sections: 1. Inclusive observables,” *arXiv* (2011) 1101.0593.
- [76] C. Lefevre, “LHC: The guide,” Jan, 2008. CERN-Brochure-2008-001.
- [77] ATLAS Collaboration, G. Aad *et al.*, “The ATLAS experiment at the CERN Large Hadron Collider,” *JINST* **3** (2008) S08003.
- [78] CMS Collaboration, R. Adolphi *et al.*, “The CMS experiment at the CERN LHC,” *JINST* **3** (2008) S08004.
- [79] ALICE Collaboration, K. Aamodt *et al.*, “The ALICE experiment at the CERN LHC,” *JINST* **3** (2008) S08002.
- [80] LHCb Collaboration, R. Aaij *et al.*, “Measurement of $\sigma(pp \rightarrow b\bar{b}x)$ at $s = 7$ TeV in the forward region,” *Phys. Lett. B* **694** (2010), no. 3, 209–216.
- [81] CDF Collaboration, T. Aaltonen *et al.*, “Measurement of the b -hadron production cross section using decays to $\mu^- D^0 X$ final states in $p\bar{p}$ collisions at $s = 1.96$ TeV,” *Phys. Rev. D* **79** (2009), no. 9, 092003.
- [82] Belle Collaboration, Y. Sakai, “Recent results from Belle experiment,” *Nucl. Phys. B* **157** (2006), no. 1, 83–90.
- [83] LHCb Collaboration, S. Amato *et al.*, “LHCb technical proposal.” CERN-LHCC-98-04.
- [84] LHCb Collaboration, R. Aaij *et al.*, “The LHCb detector at LHC,” *JINST* **3** (2008) S08005.

- [85] LHCb Collaboration, P. R. Barbosa-Marinho *et al.*, “LHCb VELO: Technical design report,” CERN, Geneva, 2001.
- [86] B. Maximilien, “Assembling the last module of the vertex locator for LHCb.” CERN-EX-0703012 14, Mar 2007.
- [87] LHCb Collaboration, S. Borghi, “First results from the LHCb Vertex Locator.” PoS(ICHEP 2010)030. Proceedings of the 35th International Conference on High Energy Physics, July 2010, Paris, France.
- [88] LHCb Collaboration, S. Borghi, “Performance of the tracking system at the LHCb Experiment.” PoS(ICHEP 2010)005. Proceedings of the 35th International Conference on High Energy Physics, July 2010, Paris, France.
- [89] LHCb Collaboration, S. Blusk, “ $B_s \rightarrow D_s h$ and $B \rightarrow Dh$ decays in LHCb,” Presentation at the 13th International Conference on B-Physics at Hadron Machines, April 2011, Amsterdam, The Netherlands.
- [90] LHCb Collaboration, S. Amato *et al.*, “LHCb RICH: Technical design report,” CERN, Geneva, 2000.
- [91] LHCb Collaboration, S. Koblitz, “Particle ID and baryon production asymmetries from LHCb,” Presentation at the 22nd Rencontres de Blois on Particle Physics and Cosmology, July 2010, Blois, France.
- [92] TA2 Collaboration, M. Alemi *et al.*, “First operation of a hybrid photon detector prototype with electrostatic cross-focussing and integrated silicon pixel readout,” *Nucl. Instrum. Meth. A* **449** (2000) 48–59.
- [93] LHCb Collaboration, L. Somerville, “Pixel hybrid photon detectors for the ring imaging Cherenkov detectors of LHCb,” *Nucl. Instrum. Meth. A* **546** (2005) 81–85.
- [94] R. Plackett, “Photon detectors for the Ring Imaging Cherenkov detectors of the LHCb experiment,” PhD thesis, Imperial College London, July 2011.
- [95] LHCb Collaboration, S. Amato *et al.*, “LHCb calorimeters: Technical design report,” CERN, Geneva, 2000.
- [96] LHCb Collaboration, A. Golutvin, “LHCb status and highlights.” PoS(ICHEP 2010)541. Proceedings of the 35th International Conference on High Energy Physics, July 2010, Paris, France.
- [97] CDF Collaboration, T. Aaltonen *et al.*, “Search for $B_s^0 \rightarrow \mu^+ \mu^-$ and $B^0 \rightarrow \mu^+ \mu^-$ decays with 2 fb^{-1} of $p\bar{p}$ collisions,” *Phys. Rev. Lett.* **100** (2008), no. 10, 101802.

- [98] Nobelprize.org, “The Nobel Prize in physics 1992 – G. Charpak.”
http://nobelprize.org/nobel_prizes/physics/laureates/1992.
- [99] LHCb Collaboration, A. Powell, “Particle Identification at LHCb.” PoS(ICHEP 2010)020. Proceedings of the 35th International Conference on High Energy Physics, July 2010, Paris, France.
- [100] LHCb Collaboration, B. Adeva *et al.*, “Roadmap for selected key measurements of lhcb.” LHCb-PUB-2009-029.
- [101] “WLCG - Worldwide LHC computing grid.” <http://lcg.web.cern.ch/lcg>.
- [102] “DIRAC - Distributed infrastructure with remote agent control.”
<https://lhcbweb.pic.es/DIRAC>.
- [103] “LHC programme coordination.” <http://lpc.web.cern.ch/lpc>.
- [104] I. Beiyayev *et al.*, “Handling of the generation of primary events in GAUSS, the LHCb simulation framework,” in “Nuclear Science Symposium Conference Record (NSS/MIC),” p. 1155–1161. IEEE, 2010.
- [105] “The Les Houches accord PDFs: LHAPDF and LHAGLUE.”
<http://hepforge.cedar.ac.uk/lhapdf>.
- [106] D. J. Lange *et al.*, “The EVTGEN particle decay simulation package,” *Nucl. Instrum. Meth. A* **462** (2001) 152.
- [107] P. Golonka and Z. Was, “PHOTOS Monte Carlo: a precision tool for QED corrections in Z and W decays,” *Eur. Phys. J. C* **45** (2006) 97.
- [108] S. Agostinelli *et al.*, “GEANT 4: a simulation toolkit,” *Nucl. Instrum. Meth. A* **506** (2003) 250.
- [109] P. A. Cherenkov, “Radiation of particles moving at a velocity exceeding that of light, and some of the possibilities for their use in experimental physics,” in “Nobel Lectures, Physics 1942-1962,” Elsevier Publishing Company, Amsterdam, 1964.
- [110] S. I. Vavilov *Dokl. Akad. Nauk SSSR* **2** (1934) 457.
- [111] P. A. Cherenkov *Dokl. Akad. Nauk SSSR* **2** (1934) 451.
- [112] P. A. Cherenkov *Dokl. Akad. Nauk SSSR* **3** (1936) 413.
- [113] I. E. Tamm and I. M. Frank *Dokl. Akad. Nauk SSSR* **14** (1937) 107.
- [114] M. Biss *et al.*, “High-speed digital shadowgraphy of shock waves from explosions and gunshots,” in “Shock Waves,” p. 91–96. Springer Berlin Heidelberg, 2009.

- [115] L. Kurnosova *et al.*, “Energy spectra of different groups of cosmic ray nuclei from Cerenkov counter measurements in satellite vehicles,” *Planetary and Space Science* **11** (1963), no. 2, 193–208.
- [116] RICE Collaboration, I. Kravchenko *et al.*, “Limits on the ultra-high energy electron neutrino flux from the RICE experiment,” *Astroparticle Physics* **20** (2003), no. 2, 195–213.
- [117] FORTE Collaboration, G. Lehtinen *et al.*, “FORTE satellite constraints on ultra-high energy cosmic particle fluxes,” *Phys. Rev. D* **69** (2004), no. 1, 013008.
- [118] GLUE Collaboration, P. W. Gorham *et al.*, “Experimental limit on the cosmic diffuse ultra-high energy neutrino flux,” *Phys. Rev. Lett.* **93** (2004), no. 4, 041101.
- [119] DELPHI Collaboration, W. Adam *et al.*, “The ring imaging Cherenkov detector of DELPHI,” *Nucl. Instrum. Meth. A* **343** (1994), no. 1, 68–73.
- [120] AMS Collaboration, J. Casaus, “The AMS-02 experiment on the ISS,” *J. Phys. Conf. Ser.* **171** (2009) 012045.
- [121] LHCb Collaboration, M. Adinolfi, N. Brook, R. W. Forty, M. John, J. Libby, B. Simmons, and G. Wilkinson, “A simulation study of the LHCb RICH performance.” LHCb-2000-66.
- [122] HERA-B Collaboration, A. Gorišek *et al.*, “Alignment of the HERA-B RICH optical system with data,” *Nucl. Instrum. Meth. A* **433** (1999) 408–412.
- [123] LHCb Collaboration, A. Papanestis, “Limits of software compensation for mirror misalignment of the RICH detectors,” Tech. Rep., LHCb-2001-141, CERN, Geneva, 2001.
- [124] LHCb Collaboration, M. Adinolfi *et al.*, “Performance of the LHCb RICH photo-detectors and readout in a system test using charged particles from a 25 ns-structured beam,” *Nucl. Instrum. Meth. A* **603** (2009), no. 3, 287–293.
- [125] C. E. Eames, “Alignment of the ring imaging Cherenkov detectors and sensitivity to the isospin asymmetry in the rare decay $B^0 \rightarrow K^* \mu^+ \mu^-$ at LHCb,” PhD thesis, Imperial College London, January 2010.
- [126] LHCb Collaboration, A. Powell, “Particle ID at LHCb,” Presentation at the 35th International Conference on High Energy Physics, July 2010, Paris, France.
- [127] LHCb Collaboration, R. W. Forty and O. Schneider, “RICH pattern recognition,” Tech. Rep., LHCb-98-040, CERN, Geneva, 1998.

- [128] LHCb Collaboration, R. Young, “Operating the Hybrid Photon Detectors in the LHCb RICH counters,” *Nucl. Instrum. Meth. A* **639** (2011), no. 1, 94–98. Proceedings of the 7th International Workshop on Ring Imaging Cherenkov Detectors.
- [129] LHCb Collaboration, F. Xing, “Magnetic Distortion Calibration for LHCb RICH Detectors,” Poster at the 7th International Workshop on Ring Imaging Cherenkov Detectors, May 2010.
- [130] LHCb Collaboration, R. Cardinale *et al.*, “Analysis and correction of the magnetic field effects in the Hybrid Photo-Detectors of the RICH 2 detector of LHCb,” Tech. Rep., LHCb-PUB-2011-013, CERN, Geneva, 2011.
- [131] LHCb Collaboration, A. Carbone *et al.*, “Measurement of direct CP violation in charmless charged two-body B decays at LHCb using 2010 data,” Les Rencontres de Physique de la Vallée d’Aoste, La Thuile, Italy, 27 February–5 March 2011. LHCb-CONF-2011-011.
- [132] L. M. Lederman, “The God particle: If the universe is the answer, what is the question?,” Dell, 1993.
- [133] C. D. Anderson *et al.*, “Cloud-chamber observations of the new unstable cosmic-ray particles,” *Phys. Rev.* **78** (1950), no. 3, 290–291.
- [134] A. Pais, “Some remarks on V -particles,” *Phys. Rev.* **86** (1952), no. 5, 663–672.
- [135] M. Baldo-Ceolin and D. J. Prowse, “Anti-lambda hyperon,” *Phys. Rev. Lett.* **1** (1958), no. 5, 179–180.
- [136] O. Chamberlain, E. Segrè, C. Wiegand, and T. Ypsilantis, “Observation of antiprotons,” *Phys. Rev.* **100** (1955), no. 3, 947–950.
- [137] J. Button, T. Elioff, E. Segrè, H. M. Steiner, R. Weingart, C. Wiegand, and T. Ypsilantis, “Antineutron production by charge exchange,” *Phys. Rev.* **108** (1957), no. 6, 1557–1561.
- [138] M. Gell-Mann and A. Pais, “Behavior of neutral particles under charge conjugation,” *Phys. Rev.* **97** (1955), no. 5, 1387–1389.
- [139] T. D. Lee, R. Oehme, and C. N. Yang, “Remarks on possible noninvariance under time reversal and charge conjugation,” *Phys. Rev.* **106** (1957), no. 2, 340–345.
- [140] R. L. Garwin, L. M. Lederman, and M. Weinrich, “Observations of the failure of conservation of parity and charge conjugation in meson decays: the magnetic moment of the free muon,” *Phys. Rev.* **105** (1957), no. 4, 1415–1417.

- [141] R. H. Good, R. P. Matsen, F. Muller, O. Piccioni, W. M. Powell, K. S. White, W. B. Fowler, and R. W. Birge, “Regeneration of neutral K mesons and their mass difference,” *Phys. Rev.* **124** (1961), no. 4, 1223–1239.
- [142] STAR Collaboration, B. I. Abelev *et al.*, “Strange particle production in $p + p$ collisions at $\sqrt{s} = 200$ GeV,” *Phys. Rev. C* **75** (2007) 064901.
- [143] ALICE Collaboration, K. Aamodt *et al.*, “Strange particle production in proton-proton collisions at $\sqrt{s} = 0.9$ TeV with ALICE at the LHC,” *Eur. Phys. J. C* **71** (2011) 1594.
- [144] CMS Collaboration, V. Khachatryan *et al.*, “Strange particle production in pp collisions at $\sqrt{s} = 0.9$ and 7 TeV,” *JHEP* **2011** (2011) 1–40.
- [145] LHCb Collaboration, R. Aaij *et al.*, “Prompt K_S^0 production in pp collisions at $\sqrt{s} = 0.9$ TeV,” *Phys. Lett. B* **693** (2010) 69.
- [146] P. Z. Skands, “Tuning Monte Carlo generators: The Perugia tunes,” *Phys. Rev. D* **82** (2010) 074018.
- [147] P. Z. Skands, “Peter’s PYTHIA plots.”
<http://home.fnal.gov/~skands/leshouches-plots/>.
- [148] S. M. T. Sjöstrand and P. Z. Skands, “A brief introduction to PYTHIA 8.1,” *Comput. Phys. Commun.* **178** (2008), no. 11, 852–867.
- [149] S. Navin, “Diffraction in PYTHIA,” *arXiv* (2010) 1005.3894.
- [150] A. Hoecker, P. Speckmayer, J. Stelzer, J. Therhaag, E. von Toerne, and H. Voss, “TMVA: toolkit for multivariate data analysis.” <http://tmva.sourceforge.net>.
- [151] LHCb Collaboration, R. Aaij *et al.*, “Measurement of $\sigma(pp \rightarrow b\bar{b}x)$ at $\sqrt{s} = 7$ TeV in the forward region,” *Phys. Lett. B* **694** (2010), no. 3, 209–216.
- [152] R. Armenteros and J. Podolanski, “Analysis of V-events,” *Philos. Mag.* **45** (1953), no. 360, 13–30.
- [153] F. Dettori, “Measurement of strange hadron production ratios and perspectives for the search of $D^0 \rightarrow \mu^+\mu^-$ decay at LHCb,” PhD thesis, Università di Cagliari, 2011.
- [154] P. Z. Skands, “Tuning Monte Carlo generators: The Perugia tunes,” *arXiv* (2011) 1005.3457v4.

- [155] STAR Collaboration, J. Adams *et al.*, “Identified hadron spectra at large transverse momentum in $p + p$ and $d + Au$ collisions at $\sqrt{s_{NN}} = 200$ GeV,” *Phys. Lett. B* **637** (2006), no. 3, 161–169.
- [156] ALICE Collaboration, K. Aamodt *et al.*, “Midrapidity antiproton-to-proton ratio in pp collisions at $\sqrt{s} = 0.9$ and 7 TeV measured by the ALICE experiment,” *Phys. Rev. Lett.* **105** (2010) 072002.
- [157] P. Z. Skands *et al.*, “PYTHIA 6 update notes.”
http://www.hepforge.org/archive/pythia6/update_notes-6.4.26.txt.
- [158] C. G. Blanks, J. Nardulli, and F. Soomro, “The laser alignment and monitoring system for the LHCb RICH detectors,” Tech. Rep., LHCb-PUB-2011-014, CERN, Geneva, 2011.
- [159] F. Soomro, “Radiative decays of B mesons at LHCb,” PhD thesis, Imperial College London, May 2011.
- [160] “DIM – Distributed Information Management System.”
<http://dim.web.cern.ch/dim>.